Study of topology and correlation effects in two-dimensional lattices

By

Rahul Ghosh

Enrolment No: PHYS11201705002

National Institute of Science Education and Research, Bhubaneswar

A thesis submitted to the

Board of Studies in Physical Sciences

(as applicable)

In partial fulfillment of requirements

for the Degree of

DOCTOR OF PHILOSOPHY

of

HOMI BHABHA NATIONAL INSTITUTE

March 5, 2026

Homi Bhabha National Institute

Recommendations of the Viva Voce Committee

As members of the Viva Voce Committee, we certify that we have read the dissertation prepared by **Rahul Ghosh** entitled **Study of topology and correlation effects in two-dimensional lattices** and recommend that it may be accepted as fulfilling the thesis requirement for the award of Degree of Doctor of Philosophy.

Chairman - Dr. Ajaya Kumar Nayak		Date 05/06/2026
Guide / Convener - Dr. Kush Saha	K Saha	Date 5/6/2026
Examiner - Prof. Saurabh Basu	Saurabh Basu	Date 5/6/2026
Member 1 - Dr. Anamitra Mukherjee		Date 5/6/26
Member 2 - Dr. Ashis Kumar Nandy		Date 05/06/2026
Member 3 - Dr. Soumya Bera	Soumya Bera	Date 05/06/2026

Final approval and acceptance of this thesis is contingent upon the candidate's submission of the final copies of the thesis to HBNI.
I/We hereby certify that I/we have read this thesis prepared under my/our direction and recommend that it may be accepted as fulfilling the thesis requirement.

Date : 05/6/2026
Place : NISER

Signature
Co-guide (if any)

K Saha
Signature
Guide KUSH SAHA

STATEMENT BY AUTHOR

This dissertation has been submitted in partial fulfillment of requirements for an advanced degree at Homi Bhabha National Institute (HBNI) and is deposited in the Library to be made available to borrowers under rules of the HBNI.

Brief quotations from this dissertation are allowable without special permission, provided that accurate acknowledgement of source is made. Requests for permission for extended quotation from or reproduction of this manuscript in whole or in part may be granted by the Competent Authority of HBNI when in his or her judgment the proposed use of the material is in the interests of scholarship. In all other instances, however, permission must be obtained from the author.

(Rahul Ghosh)

DECLARATION

I, hereby declare that the investigation presented in the thesis has been carried out by me. The work is original and has not been submitted earlier as a whole or in part for a degree / diploma at this or any other Institution / University.

(Rahul Ghosh)

Certification on Academic Integrity

Undertaking by the Student:

1. I **Rahul Ghosh**, HBNI Enrolment No. PHYS11201705002 hereby undertake that the Thesis, titled **Study of topology and correlation effects in two-dimensional lattices** is prepared by me and is the original work undertaken by me.

2. I also hereby undertake that this document has been duly checked through a plagiarism detection tool and the document is found to be plagiarism free as per the guidelines of the Institute/UGC.

3. I am aware and undertake that if plagiarism is detected in my thesis at any stage in the future, suitable penalty will be imposed as applicable as per the guidelines of the Institute/UGC.

Rahul Ghosh

(Rahul Ghosh)

Endorsed by the Thesis Supervisor:

I certify that the thesis written by the Researcher is plagiarism free as mentioned above by the student.

Signature of the Thesis Supervisor with date NSaha 5/6/2026

Name : Dr. Kush Saha

Designation : Reader - F

Department/ Centre : School of Physical Sciences

Name of the CI/ OCC : National Institute of Science Education and Research

List of Publications arising from the thesis

Journal

1. ”Spin-imbalance induced buried topological edge currents in Mott and topological insulator heterostructures”, Rahul Ghosh, Subhajyoti Pal, Kush Saha and Anamitra Mukherjee, New Journal of Physics, **2025**, 27, 113502 .

2. ”Quantum phases in a two-dimensional generalized interacting Su-Schrieffer-Heeger model”, Rahul Ghosh, Phys. Rev. B 113, 115149 (**2026**).

Conferences

1. Spectroscopies of Novel Superconductors (SNS) 2022. IISc Bangalore, India, 12-16 December 2022.

2. Young Investigators Meet on Quantum Condensed Matter Theory (YIMQCMT)-2022. NISER Bhubaneswar, India, 29 October-1st November 2022.

(Rahul Ghosh)

Dedication

This thesis is dedicated to the loving memory of my father,
Late Ranjit Ghosh,
and to my mother, Tapati Ghosh, and my sister, Rima Ghosh,
for their endless love, unwavering support, and constant encouragement.

ACKNOWLEDGEMENTS

I would like to express my deepest gratitude to my guide, **Dr. Kush Saha**, for his immense support, constant encouragement, and invaluable guidance throughout my research journey. His insightful suggestions and unwavering mentorship have been instrumental in shaping this work. I am especially grateful to **Dr. Anamita Mukherjee** and **Dr. Subhajyoti Pal** (my batchmate) for their immense contributions and fruitful collaboration on my first paper. Their expertise and dedication greatly enriched the quality of the work. I am also thankful to the other members of the doctoral committee for their valuable assessment and constructive feedback.

I also thank my batchmates **Dr. Prottoy Das, Dr. Sourav Bhakta, Shrish,** and **Dr. Shuvayu Roy**, along with my college mate **Dr. Sourav Gope**, for their friendship and for making my Integrated PhD journey memorable and enjoyable. I am thankful to my lab mates **Atanu Jana, Ritwika Majumdar,** and **Dr. Sujit NS** for their constant presence and support during a significant part of this long journey. I would also like to acknowledge my junior and group mates **Ivan Dutta, Sayan Banik,** and **Dr. Akash Dey** for their help and camaraderie. Special thanks to my other NISER friends **Dr. Debamaly Dutta, Dr. Subhadip Pradhan,** and **Dr. Soumik Nandy** for their support and companionship.

I am grateful to **NISER** and **HBNI** for providing me with this wonderful opportunity, and to **DAE** for funding my Integrated PhD program. Finally, I would like to acknowledge **ChatGPT, Copilot** and **Gemini** for their assistance in writing and debugging code, facilitating my learning process.

Contents

Abstract xi

List of Figures xiii

Chapter 1 Introduction 1

1.1 Topological invariants and bulk–edge correspondence 4
1.2 Topology in different tight-binding models 7
1.2.1 Su–Schrieffer–Heeger model: One-dimensional topology 8
1.2.2 Haldane model: Chern insulator without magnetic field 10
1.2.3 Kane–Mele model: Time-reversal-invariant topology 13
1.3 Beyond the noninteracting picture 14
1.3.1 Can interactions generate topology? 15
1.3.2 Dirac points versus quadratic band touching 18
1.3.3 Other competing orders and the role of nematicity 20
1.4 Effects of interaction on band topology 21
1.4.1 Kane–Mele–Hubbard and Bernevig–Hughes–Zhang–Hubbard models 22
1.5 Interfaces and heterostructures: Correlated topological matter 24
1.5.1 Limitations 26
1.6 Motivation and research questions 27
1.7 Outline of the thesis 28

Chapter 2 Theoretical formalism and computational methods 30

2.0.1 Generalized interacting lattice Hamiltonian 30
2.1 Hartree–Fock mean field method 31
2.1.1 Spinless fermions with extended interactions 32
2.1.2 Spinful fermions with on-site Hubbard interaction 33
2.1.3 Self-consistency, initial conditions, and competing solutions 33

2.1.4 Limitations . . . 34
2.2 Slave-rotor mean-field theory . . . 34
2.3 Topological invariants . . . 37
2.4 Current operators . . . 37

Chapter 3 Quantum phases in two dimensional generalized interacting SSH model 39

3.1 Generalized two-dimensional SSH model . . . 40
3.2 Hartree–Fock formulation and momentum-space Hamiltonian . . . 43
3.3 Order parameters and symmetry classification . . . 45
3.3.1 Quantum anomalous Hall order . . . 45
3.3.2 Site-nematic insulating order . . . 46
3.3.3 Stripe charge-density-wave order . . . 46
3.3.4 Bond-nematic order . . . 46
3.3.5 Summary of symmetry breaking patterns . . . 47
3.4 Interaction-driven phase diagrams and physical discussion . . . 47
3.4.1 Phase diagram in the quadratic band touching regime: checkerboard limit . . . 48
3.4.2 Phase diagram in the quadratic band touching regime with hopping asymmetry . . . 51
3.4.3 Competition of order parameters in the quadratic band touching regime . . . 52
3.4.4 Phase diagram in the Dirac semimetal regime . . . 56
3.5 Summary and conclusion . . . 58

Chapter 4 Spin-imbalance induced buried topological edge currents in MI–TI heterostructures 60

4.1 Heterostructure geometry and physical setup . . . 61
4.2 Model Hamiltonian . . . 63
4.3 Theoretical methods . . . 65
4.3.1 Hartree–Fock approach . . . 66

4.3.2 Slave-rotor mean-field approach 68
4.4 Results 69
4.4.1 Buried topological edge states and spectral reconstruction 69
4.4.2 Edge reconstruction 71
4.4.3 Charge and spin currents 75
4.4.4 Slave-rotor results 76
4.5 Summary and conclusion 79

Chapter 5 Summary and conclusions 81

References 87

Chapter A Appendix 101
A.1 Chern number and QAH order parameter 101
A.2 Proof of particle-hole symmetry 102

Chapter B Appendix 109
B.1 Mean field in k-space 109
B.2 Long-range Coulomb interaction 110
B.3 Computational details of self-consistency in Hartree-Fock approach in heterostructure problem 110

Chapter C Appendix 112
C.1 Derivation of current 112

Chapter D Appendix 114
D.1 Slave-rotor mean field theory 114
D.2 Observable in Slave-rotor calculation 116

Abstract

The discovery of topological insulators (TIs) established that quantum phases can be characterized by global topological invariants rather than local order parameters. While topological band theory has been highly successful in describing noninteracting systems, the role of strong electron–electron interactions remains an important open problem. This thesis explores how electronic correlations can both generate new topological phases and reconstruct existing topological states beyond the conventional band-theory framework.

In the first part of this thesis, we investigate interaction-driven topological phases in a two-dimensional generalized Su–Schrieffer–Heeger (SSH) model using a self-consistent Hartree–Fock approach. We chart out the phase diagram of a semimetal with a quadratic band-touching point and identify an interaction-induced quantum anomalous Hall (QAH) phase characterized by a nonzero Chern number. Besides the QAH phase, interactions stabilize several competing charge- and bond-ordered states, including a bond-nematic Dirac semimetal (BNDS) phase not reported in earlier mean-field studies. We further show that an onsite potential suppresses the interaction-driven QAH phase while significantly enlarging the stability region of the BNDS phase, highlighting the rich interplay between symmetry breaking and topology in systems with an enhanced low-energy density of states.

The second part of the thesis focuses on the impact of strong correlations at interfaces two between distinct insulators. We investigate a heterostructure composed of a ferrimagnetic Mott insulator and a time-reversal-invariant topological insulator on a Lieb lattice. By combining Hartree–Fock and slave-rotor mean-field methods, we show that topological boundary modes can survive in a buried form at the interface despite the presence of strong correlations. Furthermore, proximity-induced magnetization generates a spin imbalance in the helical edge states. Owing to spin–momentum locking, this imbalance converts a dissipationless spin current into a topologically protected charge current, providing a novel interaction-driven mechanism for controlling interfacial transport.

Overall, this thesis demonstrates that electron–electron interactions can both create and reconstruct topological phases. The results provide new insights into correlated topological matter and broaden the understanding of topological phenomena in strongly interacting

systems.

List of Figures

1.1 Hall voltage U_H and longitudinal voltage U_{PP} plotted as functions of the gate voltage V_g, measured at a temperature of $1.5\,\mathrm{K}$ under an applied magnetic field of $18\,\mathrm{T}$ [1]. 2

1.2 Schematic illustration of the SSH model featuring alternating hopping amplitudes t_1 and t_2. The thick (thin) bonds represent stronger (weaker) hopping strengths, respectively. 8

1.3 Band dispersion of the SSH model. The spectrum for periodic boundary conditions is shown in (a), whereas (b) and (c) illustrate the spectra obtained with open boundary conditions for the two different hopping regimes of the model [2]. 9

1.4 (a) Illustration of the Haldane model defined on a honeycomb lattice structure. (b) Phase diagram plotted in the ϕ–M parameter space, showing the corresponding Chern number values across different regions. (c) Schematic depiction of the edge-state behavior in the Haldane model under open boundary conditions. When the Chern number is finite ($\nu = \pm 1$), the system hosts robust chiral edge modes protected by topology, with their propagation direction determined by the sign of ν. In contrast, these edge states are absent in the topologically trivial phase ($\nu = 0$) [2]. 10

1.5 Interacting lattice model in honeycomb geometry 15

1.6 Phase diagram at half filling of spinless interacting fermions on the honeycomb lattice [3]. 17

3.1 Schematic of the two-dimensional Su–Schrieffer–Heeger (SSH) model on a square lattice with four sites per unit cell (plaquette). Nearest-neighbor (NN) hoppings include intra-cell bonds (blue, amplitude t_1) and inter-cell bonds (red, amplitude t_2). Next-nearest-neighbor (NNN) hoppings introduce diagonal couplings: green and purple bonds denote amplitudes t_1' and t_2', respectively. 41

3.2 **(a)** Noninteracting band structure at $\delta = 0$, showing a quadratic band touching (QBT) at the Brillouin-zone M point (π, π). **(b)** Band structure at $\delta = -0.2t_1$ with $t_1 = 1.0$ and $t_2 = 2.0$, where the QBT splits into two Dirac cones. The high-symmetry points are $\Gamma = (\frac{\pi}{2}, \frac{\pi}{2})$, $X = (\pi, \frac{\pi}{2})$, $Y = (\frac{\pi}{2}, \pi)$, and $M = (\pi, \pi)$. 42

3.3 **Interaction-driven phase diagrams of the generalized 2D SSH model at $\delta = 0$ for different hopping configurations. (a)** Phase diagram for the symmetric hopping case $t_1 = t_2 = 1.0$, corresponding to the checkerboard limit. Four distinct phases emerge: a QAH phase with spontaneous time-reversal symmetry breaking (black), a SNI that breaks C_4 symmetry (purple), a stripe CDW (red), and a BNDS with gapless anisotropic Dirac nodes (yellow). **(b)** Phase diagram for asymmetric hopping with $t_1 = 1.0$ and $t_2 = 2.0$, representative of the generalized SSH regime. The QAH phase remains robust, while the BNDS region expands significantly due to enhanced bond anisotropy. The site-nematic and stripe-ordered insulating phases persist but shrink in extent. **(c)** Phase diagram for another asymmetric case, $t_1 = 2.0$ and $t_2 = 1.0$. While the overall structure is similar to (b), the QAH region is reduced, reflecting the sensitivity of topological ordering to the direction of hopping asymmetry. The BNDS and insulating phases continue to dominate, underscoring their robustness. **(d-g)** Representative band spectra and ordering patterns of spinless fermions at half-filling in the topologically trivial SSH lattice with a QBT point, shown for asymmetric hopping parameters $t_1 = 1.0$ and $t_2 = 2.0$. The QAH phase is distinguished by loop-current order, while the BNDS phase features anisotropic bond ordering. SNI and stripe CDW phases are also illustrated with their characteristic charge distributions. Circle sizes indicate the local charge density, and bond widths represent the magnitude of the bond-order parameter. . . 49

3.4 **(a)** Evolution of the QAH and BNDS order parameters as functions of the interaction strength U for fixed hopping amplitudes $t_1 = 1.0$, $t_2 = 2.0$, and onsite potential $\delta = 0$. At weak coupling, the system exhibits a pure BNDS phase characterized by spontaneous bond-nematic order. In the intermediate U regime, both QAH and BNDS order parameters coexist, indicating an interaction-induced topological-nematic mixed phase. As U increases further, the QAH order is suppressed, and a narrow BNDS region emerges before the transition to a SNI phase. **(b)** Corresponding plot for $t_1 = 2.0$, $t_2 = 1.0$, showing a reduced extent of the QAH phase and a slightly broader BNDS region separating the QAH and SNI phases. All the data in (a) and (b) are in arbitrary unit. **(c)** Site-nematic order parameter δ_{site} as a function of U for $t_1 = 1.0$, $t_2 = 2.0$. The SNI order parameter remains finite across all phases, including the BNDS and QAH regimes, but becomes strongly enhanced deep in the SNI phase, signaling a crossover from weak to strong site-nematic order. **(d)** Similar behavior of δ_{site} for $t_1 = 2.0$, $t_2 = 1.0$, consistent with the trends observed in panel (c), confirming the robustness of site-nematic fluctuations across the phase diagram. All plots are obtained for fixed next nearest-neighbor interaction strength $V = 2.0t_1$ in panels (a) and (c), and $V = 2.0t_2$ in panels (b) and (d). 53

3.5 Interaction dependence of the sublattice-dependent bond order. **(a)** $t_1 = 1.0, t_2 = 2.0$ and **(b)** $t_1 = 2.0, t_2 = 1.0$, both exhibiting a finite value that signals sublattice-selective bond order driving anisotropic BNDS formation. For comparison, the symmetric checkerboard limit $(t_1 = t_2 = 1.0)$ yields zero difference, confirming the absence of sublattice dependence. . . 54

3.6 **Interaction-driven phase diagrams in the Dirac semimetal regime with $t_1 = 1.0$ and $t_2 = 2.0$ for varying staggered potential δ. (a)** For $\delta = 0.2t_1$, a finite staggered potential already reduces the extent of the QAH phase (black) compared to the $\delta = 0$ case. **(b)** At $\delta = 0.4t_1$, the QAH region is further suppressed. **(c)** For $\delta = 0.6t_1$, the QAH phase is nearly absent, giving way to the BNDS phase. Across all cases, increasing δ destabilizes the interaction-induced QAH state in favor of BNDS, indicating that the QAH phase remains robust only for weak sublattice staggering. 56

4.1 **Heterostructure schematic :** We divide a periodically identified Lieb lattice into $U \neq 0$ and $\lambda \neq 0$ parts along the x-direction. The resulting interfaces (vertical dashed lines) are parallel to the y-direction. Unit cells and sites of $\lambda_R - U_L$ interface (I_1) and $U_R - \lambda_L$ interface (I_2) are labeled as follows. The [ac] edge denotes that the (ac) sites on the U_L edge hybridize with the (b) sites on the region labeled by λ_R. At the [b] edge, the (b) sites on the U side interface with (ac) sites of the TI. The three-unit cell consists of sites labeled by 'a, 'b', and 'c.' The two heterostructure cases with interfaces [b]-[ac] and [b]-[b] are demarcated at the bottom with arrows. The three site unit cell is marked with 'I' and the vertical layers of (ac) sites and (b) sites demarcated by $\mathcal{L}$ =1, 2 ,3 ... are also shown. 62

4.2 **Density of states & edge modes for [b]-[ac] heterostructure**. (i) show the unit-cell projected DOS. The interface unit cell DOS (black) and (red), respectively, are for the [b] and [ac] interfaces, one unit cell on either side of the interface. (ii) and (iii) show the spin-resolved momentum (k_y)-dependent buried-interface modes at the two interfaces. The dispersions are computed, including contributions from one unit cell on the $U \neq 0$ and three on the $\lambda \neq 0$ side, for the [ac] (black) and [b] (red) interfaces respectively. The results are presented for $\lambda = 0.3t$ and $U = 7t$ on a Lieb lattice with 20 three-site unit cells along the x-direction, while translation symmetry is assumed along the y-direction. 70

4.3 **Magnetic and charge reconstructions across the heterostructure interface.** (i) and (iii) show the layer-resolved charge density $N(\mathcal{L})$ (black line) and magnetization $M(\mathcal{L})$, respectively, along the x direction for the $[b]-[ac]$ heterostructure. (ii) and (iv) present the corresponding profiles for the $[b]-[b]$ heterostructure. In all panels, alternating layers along the x axis are composed of (**a**–**c**) and **b** sublattice sites, as defined in Fig. 4.1. The results are computed for $\lambda = 0.3t$ and $U = 7t$. 72

4.4 **Charge and spin currents for the $[b]-[ac]$ heterostructure.** (i) Charge current $J_c = J_\uparrow + J_\downarrow$ (squares) and magnetization M_z (circles) as functions of the spin–orbit coupling λ for the $[b]$ interface. (ii) shows the corresponding results for the $[ac]$ interface. (iii) and (iv) display the spin currents $J_s = J_\uparrow - J_\downarrow$ at the $[b]$ and $[ac]$ interfaces, respectively. All quantities are averaged over contributions from the three edge unit cells on the TI side of the heterostructure. Filled (open) symbols with solid (dashed) lines correspond to $U = 7t$ ($U = 6t$). 74

4.5 **Unit-cell-resolved density of states for the [b]-[ac] heterostructure within slave-rotor mean-field theory.** We present the unit-cell-resolved density of states (DOS) obtained from slave-rotor mean-field theory for the [b]-[ac] heterostructure. The red and black curves correspond to the DOS at the [b] and [ac] interfaces, respectively, computed from one unit cell on each side of the interface. The results are shown for $\lambda = 0.3t$ and $U = 7t$, on a Lieb lattice comprising 20 three-site unit cells along the x-direction, with translational symmetry assumed along the y-direction. 77

A.1 (a) Chern number as a function of the nearest-neighbor interaction strength U. The system exhibits a quantized value $|C| = 1$ within the QAH phase. (b) Quantum anomalous Hall (QAH) order parameter as a function of U, which is finite in the QAH phase and vanishes upon entering the site-nematic phase. Results are shown for $V = 3.0t_1$, $t_1 = 1.0$, and $t_2 = 2.0$. 101

Chapter 1

Introduction

In the twentieth century, condensed matter physics developed as a discipline to understand how simple microscopic laws governing electrons give rise to the rich variety of macroscopic properties observed in solids. For much of this period, band theory accomplished this objective with great success [4, 5]. Using Bloch's theorem, band theory treated electrons in a periodic crystal as the free particles moving in an energy band. This framework provided a clear classification of materials as metals, semiconductors, or insulators based on their band structure and offered accurate, predictive descriptions for a wide range of materials. Even today, band theory remains as fundamental basis of modern solid-state physics.

Despite the success of band theory, the single-particle picture is inadequate for describing many complex electronic phenomena. In some materials, interactions between electrons play a decisive role, and the electronic structure qualitatively differs from the band theory of independent electrons. Phenomena such as magnetism, metal-insulator transition, and unconventional superconductivity cannot be understood within the framework of noninteracting band theory. Instead, they emerge from a fundamental competition between kinetic energy, which favors electron delocalization, and Coulomb repulsion, which tends to localize electrons. This competition results in collective behavior that lies well beyond the scope of conventional band theoretic descriptions.

Traditionally, these collective phases were understood through Landau's theory of phase transitions [6]. This framework classifies matter according to spontaneously broken symmetries and local order parameters, successfully describing states such as ferromagnets and

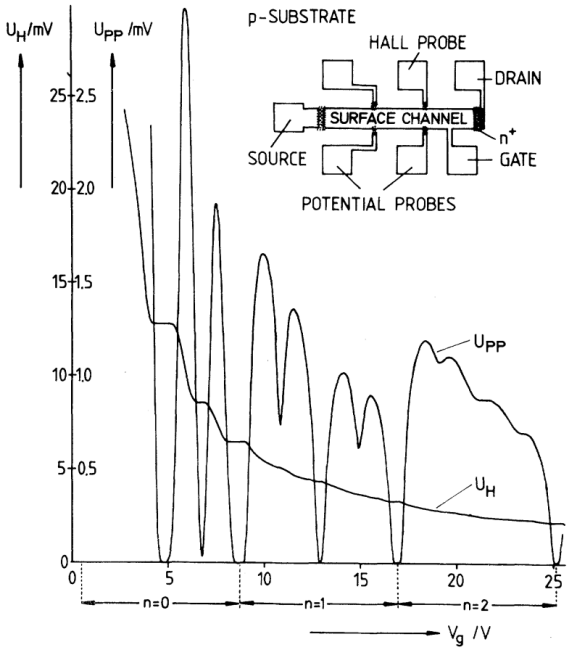

Figure 1.1: Hall voltage U_H and longitudinal voltage U_{PP} plotted as functions of the gate voltage V_g, measured at a temperature of $1.5\,\mathrm{K}$ under an applied magnetic field of $18\,\mathrm{T}$ [1].

superconductors. Within this paradigm, distinct phases are characterized by their symmetry properties, and phase transitions correspond to symmetry breaking events.

The discovery of the integer quantum Hall effect (IQHE), however exposed a fundamental limitation of this symmetry-based classification. In a two-dimensional electron gas at low temperature subjected to a strong magnetic field, the Hall conductivity is quantized as

$$\sigma_{xy} = \frac{e^2}{h}\,\nu, \tag{1.1}$$

with $\nu \in \mathbb{Z}$. This quantization is extraordinarily robust against disorder and microscopic details, yet it cannot be explained by any local order parameter. Rather, it reflects a global property of the electronic ground state.

Experimental evidence for the IQHE is shown in Fig. 1.1, where the Hall voltage exhibits precisely quantized plateaus accompanied by vanishing longitudinal resistance. The quantized Hall resistance is independent of sample geometry and disorder, highlighting its

topological origin. Quantum mechanically, a strong magnetic field quantizes the electronic spectrum into discrete Landau levels. In the semiclassical picture [7], electrons execute cyclotron motion in the bulk, where disorder localizes the states, while at the sample boundaries they undergo skipping orbits, forming chiral edge states responsible for transport.

Thouless, Kohmoto, Nightingale and den Nijs [8] provided a complete theoretical understanding, demonstrating that the integer ν corresponds to a topological invariant of electronic wavefunctions. This established that quantum phases may be distinguished not only by symmetry, but also by global topological properties that remain invariant as long as the bulk energy gap does not close. This realization introduced topology as an alternative fundamental principle for characterizing quantum phases in condensed matter physics. Topological phases are characterized by bulk invariants that are insensitive to local perturbations, yet they manifest through robust boundary phenomena. A defining feature of such phases is the bulk–edge correspondence, which guarantees that nontrivial bulk topology is accompanied by protected edge or interface states.

Subsequent developments showed that topological phases are not limited to systems exposed to strong magnetic fields. Lattice models demonstrated that nontrivial topology can emerge purely from the internal structure of Bloch wavefunctions, even in zero magnetic field [9]. This led to the prediction and experimental realization of time-reversal-invariant topological insulators, which possess insulating bulks and robust metallic boundary modes protected by symmetry. Importantly, these developments were understood within the framework of noninteracting band theory, where topology arises from the global structure of single-particle Bloch wavefunctions. In this picture, topological invariants are defined for occupied energy bands and do not require electron–electron interactions.

At the same time, the role of electron–electron interactions in topological systems emerged as a central open problem. Since real materials are rarely weakly interacting, fundamental questions naturally arise: Can interactions destabilize or destroy topological phases?

How do they modify or reconstruct boundary states? More intriguingly, can interactions themselves generate topological phases in systems that are trivial in the noninteracting limit? Answering these questions requires moving beyond uniform, weakly interacting models. Lattice geometry, band degeneracies, and the low-energy spectrum play a crucial role in determining how interactions act. In many cases, interactions favor conventional symmetry-breaking orders [10, 11, 12] that compete with topology, while in other situations—particularly in systems with enhanced low-energy phase space—they can generate topological mass terms and stabilize nontrivial phases [13, 14, 15, 16]. An additional layer of complexity arises in spatially inhomogeneous systems. For example, interfaces and heterostructures [17, 18, 19] break translational symmetry and introduce strong spatial variations in charge density, screening, and correlation strength. Such conditions are not exceptional, but are often found in real materials and engineered structures. At interfaces, new electronic states can emerge that have no counterpart in any of the bulk materials, and the interplay between topology and strong correlations becomes especially pronounced.

This thesis is motivated by the need to understand topology as an emergent phenomenon shaped by interactions, symmetry breaking, and spatial inhomogeneity. The central goal is to clarify how topological phases emerge, compete, and reconstruct in interacting lattice systems and correlated heterostructures.

1.1 Topological invariants and bulk–edge correspondence

Topological phases are distinguished by global properties of electronic wavefunctions that remain invariant under smooth deformations of the Hamiltonian, as long as the bulk energy gap does not close and the relevant symmetries are preserved. These properties are quantified by topological invariants, which provide a robust classification of quantum phases beyond the conventional Landau symmetry-breaking paradigm.

In crystalline solids, electronic states are described by Bloch wavefunctions of the form

$$\psi_{n\mathbf{k}}(\mathbf{r}) = e^{i\mathbf{k}\cdot\mathbf{r}}\, u_{n\mathbf{k}}(\mathbf{r}), \tag{1.2}$$

where n labels the band index and $\mathbf{k}$ lies in the Brillouin zone. While the energy spectrum is determined by the eigenvalues of the Bloch Hamiltonian, the topological properties of a band are encoded in the geometry of the Bloch eigenstates $|u_{n\mathbf{k}}\rangle$ as the crystal momentum $\mathbf{k}$ is varied across the Brillouin zone. When the crystal momentum is changed adiabatically along a closed loop $\mathcal{C}$ in momentum space [20], the wavefunction of an isolated Bloch band acquires a geometric phase known as the Berry phase [21],

$$\gamma_n(\mathcal{C}) = \oint_{\mathcal{C}} \mathbf{A}_n(\mathbf{k}) \cdot d\mathbf{k}, \tag{1.3}$$

where the Berry connection is defined as

$$\mathbf{A}_n(\mathbf{k}) = i\langle u_{n\mathbf{k}}|\nabla_{\mathbf{k}} u_{n\mathbf{k}}\rangle, \tag{1.4}$$

which acts as a gauge potential in momentum space. Although the Berry connection depends on the phase choice of the Bloch states, the Berry phase accumulated along a closed path is gauge invariant modulo 2π and is therefore physically meaningful.

The local geometric structure of the Bloch states is captured by the Berry curvature, defined as the curl of the Berry connection,

$$\Omega_n(\mathbf{k}) = \nabla_{\mathbf{k}} \times \mathbf{A}_n(\mathbf{k}). \tag{1.5}$$

The Berry curvature plays a role analogous to that of a magnetic field in momentum space and underlies a variety of anomalous transport effects. Most importantly, it serves as the fundamental ingredient for defining topological invariants in band insulators.

In time-reversal symmetry broken two-dimensional systems, the relevant topological invariant is the Chern number. For a filled and isolated band n, the Chern number (ν_n) is

obtained by integrating the Berry curvature over the entire Brillouin zone as

$$\nu_n = \frac{1}{2\pi} \int_{\mathrm{BZ}} d^2k \, \Omega_n(\mathbf{k}). \tag{1.6}$$

This quantity is quantized to integer values and cannot change continuously under variations of system parameters. A change in the Chern number necessarily requires the closing of the bulk energy gap, signaling a topological phase transition.

When several bands are occupied, the physically relevant invariant is the sum of the Chern numbers of all occupied bands. This invariant has a direct and experimentally measurable consequence [22]: it determines the quantized Hall conductivity through the Thouless–Kohmoto–Nightingale–den Nijs (TKNN) relation,

$$\sigma_{xy} = \frac{e^2}{h} \sum_{n \in \mathrm{occ}} \nu_n. \tag{1.7}$$

The remarkable robustness of the integer quantum Hall effect against disorder and microscopic perturbations follows directly from the quantization of the Chern number, which cannot change without a closing of the bulk energy gap.

As mentioned, a central principle related to topological phases is the bulk–edge correspondence [23, 24], which establishes a direct link between bulk topology and boundary physics. According to this principle, a nontrivial bulk topological invariant guarantees the existence of gapless boundary modes at the interface between two topologically distinct phases. In the case of a two-dimensional Chern insulator with total Chern number ν, bulk–edge correspondence implies the presence of $|\nu|$ chiral edge modes propagating along each boundary. These modes are unidirectional and cannot be removed without closing the bulk gap or eliminating the topological distinction between the bulk and the surrounding vacuum. Physically, the chiral edge states provide the channels through which the quantized Hall current is carried.

In systems that preserve time-reversal symmetry, the situation is more subtle. Because the Berry curvature is odd under time reversal, the total Chern number necessarily vanishes.

Nevertheless, such systems can still possess nontrivial topological structure. The famous example is the quantum spin Hall insulator [25, 26, 27], which supports counter-propagating helical edge states that are protected by time-reversal symmetry. In this case, the appropriate topological invariant is a $\mathbb{Z}_2$ invariant that distinguishes trivial and nontrivial time-reversal-invariant insulators.

For centrosymmetric systems, this invariant can be computed directly from bulk band structure using the parity eigenvalues of the occupied bands at the time-reversal invariant momenta (TRIMs) $\{\Gamma_i\}$,

$$(-1)^q = \prod_i \prod_{m\in\text{occ}} \xi_{2m}(\Gamma_i), \tag{1.8}$$

where $\xi_{2m}(\Gamma_i) = \pm 1$ denotes the parity eigenvalue of the mth Kramers pair. A nontrivial value $q = 1$ signals the presence of an odd number of Kramers pairs of helical edge states, while $q = 0$ corresponds to a topologically trivial insulator.

The quantization of these invariants reflects the global structure of the Bloch eigenstates and remains unchanged under smooth perturbations that preserve the bulk energy gap. They therefore provide a bulk characterization of topological phases that is directly connected to protected boundary states through the bulk–edge correspondence. In the following section, these ideas are illustrated concretely using simple lattice models that realize topological phases in a transparent and controlled manner.

1.2 Topology in different tight-binding models

In this section, we discuss three well-known lattice models: the Su–Schrieffer–Heeger model in one dimension and the Haldane and Kane–Mele models in two dimensions. These models are not merely illustrative examples: together, they explain the basics of topological band theory and provide the reference framework for understanding how interactions modify or generate topological phases.

1.2.1 Su–Schrieffer–Heeger model: One-dimensional topology

The Su–Schrieffer–Heeger (SSH) model [28, 29] provides the simplest realization of a topological phase in one dimension. It describes spinless fermions hopping on a dimerized chain with two sites per unit cell and alternating nearest-neighbor hopping amplitudes. The real-

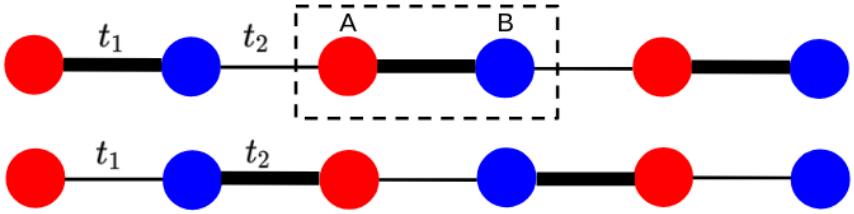

Figure 1.2: Schematic illustration of the SSH model featuring alternating hopping amplitudes t_1 and t_2. The thick (thin) bonds represent stronger (weaker) hopping strengths, respectively.

space Hamiltonian is given by

$$H_{\text{SSH}} = \sum_n \left(t_1 \, c^\dagger_{n,A} c_{n,B} + t_2 \, c^\dagger_{n,B} c_{n+1,A} + \text{H.c.} \right), \tag{1.9}$$

where t_1 and t_2 denote the intra-cell and inter-cell hopping amplitudes, respectively, and A, B label the two sublattices as indicated in Fig. 1.2.

Upon Fourier transformation, the Bloch Hamiltonian can be written in the compact form

$$H(k) = d_x(k)\, \sigma_x + d_y(k)\, \sigma_y, \tag{1.10}$$

with

$$d_x(k) = t_1 + t_2 \cos k, \tag{1.11}$$

$$d_y(k) = t_2 \sin k. \tag{1.12}$$

The energy spectrum consists of two bands,

$$E_\pm(k) = \pm \sqrt{d_x^2(k) + d_y^2(k)}, \tag{1.13}$$

which are separated by a bulk gap except at $t_1 = t_2$, where the gap closes at $k = \pi$.

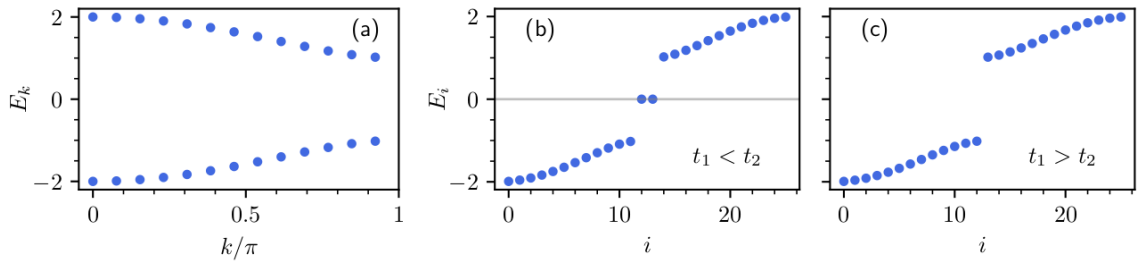

Figure 1.3: Band dispersion of the SSH model. The spectrum for periodic boundary conditions is shown in (a), whereas (b) and (c) illustrate the spectra obtained with open boundary conditions for the two different hopping regimes of the model [2].

The topology of the SSH model is characterized by a winding number,

$$\nu = \frac{1}{2\pi} \int_{-\pi}^{\pi} dk \, \frac{d_x \partial_k d_y - d_y \partial_k d_x}{d_x^2 + d_y^2}. \tag{1.14}$$

Evaluating this expression yields

$$\nu = \begin{cases} 1, & |t_2| > |t_1|, \\ 0, & |t_1| > |t_2|. \end{cases} \tag{1.15}$$

The energy spectrum for periodic and open boundary conditions is shown in Fig. 1.3. Under periodic boundary conditions [Fig. 1.3(a)], the system exhibits two gapped bulk bands, except at the critical point $t_1 = t_2$, where the gap closes. In contrast, under open boundary conditions, the topologically nontrivial phase ($\nu = 1$), shown in Fig. 1.3(b), supports zero-energy edge states within the bulk gap that are exponentially localized at the ends of the chain. These boundary states are protected by chiral symmetry and provide a direct manifestation of the bulk–edge correspondence.

Beyond its original one-dimensional setting, the SSH model plays an important conceptual role as a building block for higher-dimensional lattice constructions. When SSH-type dimerization patterns are extended to two dimensions, they naturally give rise to Dirac points or quadratic band touching points. These band degeneracies form the basis for the

interaction-driven instabilities and topological phases as will be discussed in chapter 3 of this thesis.

1.2.2 Haldane model: Chern insulator without magnetic field

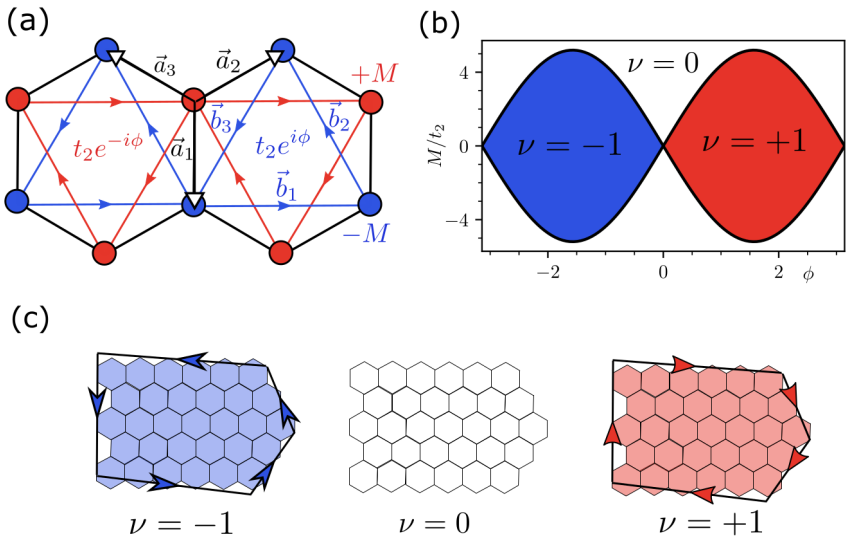

Figure 1.4: (a) Illustration of the Haldane model defined on a honeycomb lattice structure. (b) Phase diagram plotted in the ϕ–M parameter space, showing the corresponding Chern number values across different regions. (c) Schematic depiction of the edge-state behavior in the Haldane model under open boundary conditions. When the Chern number is finite ($\nu = \pm 1$), the system hosts robust chiral edge modes protected by topology, with their propagation direction determined by the sign of ν. In contrast, these edge states are absent in the topologically trivial phase ($\nu = 0$) [2].

The Haldane model [9, 30] provides a paradigmatic example of a two-dimensional Chern insulator and demonstrates that a quantized Hall response can arise even in the absence of an external magnetic field. The model is defined on a honeycomb lattice (Fig. 1.4(a)) and combines real nearest-neighbor hopping with complex next-nearest-neighbor hopping arranged so that the net magnetic flux through each unit cell vanishes. The tight-binding Hamiltonian of the model is given by

$$H = -t \sum_{\langle ij \rangle} c_i^\dagger c_j - t_2 \sum_{\langle\langle ij \rangle\rangle} e^{i\nu_{ij}\phi} c_i^\dagger c_j + M \sum_i \xi_i \, c_i^\dagger c_i, \tag{1.16}$$

where t denotes the nearest-neighbor hopping amplitude and t_2 is the next-nearest-neighbor hopping strength. The phase ϕ encodes the circulating currents associated with the complex hopping, while $\nu_{ij} = \pm 1$ depends on the direction of the hopping path. The factor $\xi_i = \pm 1$ labels the two sublattices of the honeycomb lattice, and M represents a staggered sublattice potential [31] that explicitly breaks inversion symmetry.

Upon Fourier transformation, the Hamiltonian can be written in momentum space in the compact form as

$$H(\mathbf{k}) = \mathbf{d}(\mathbf{k}) \cdot \boldsymbol{\sigma}, \tag{1.17}$$

where $\boldsymbol{\sigma}$ denotes the Pauli matrices acting in sublattice space. The components of the $\mathbf{d}$ vector are

$$d_x(\mathbf{k}) = -t \sum_{i=1}^{3} \cos(\mathbf{k} \cdot \boldsymbol{a}_i), \tag{1.18}$$

$$d_y(\mathbf{k}) = -t \sum_{i=1}^{3} \sin(\mathbf{k} \cdot \boldsymbol{a}_i), \tag{1.19}$$

$$d_z(\mathbf{k}) = M - 2t_2 \sin\phi \sum_{i=1}^{3} \sin(\mathbf{k} \cdot \mathbf{b}_i), \tag{1.20}$$

where $\mathbf{a}_i$ and $\mathbf{b}_i$ represent the nearest- and next-nearest-neighbor vectors, respectively. The three nearest-neighbor vectors are given as

$$\boldsymbol{a}_1 = a(0, 1), \tag{1.21}$$

$$\boldsymbol{a}_2 = a\left(\frac{\sqrt{3}}{2}, -\frac{1}{2}\right), \tag{1.22}$$

$$\boldsymbol{a}_3 = a\left(-\frac{\sqrt{3}}{2}, -\frac{1}{2}\right). \tag{1.23}$$

The three next-nearest-neighbor vectors can be expressed as

$$\boldsymbol{b}_1 = \boldsymbol{a}_2 - \boldsymbol{a}_3 = a(\sqrt{3}, 0), \tag{1.24}$$

$$\boldsymbol{b}_2 = \boldsymbol{a}_3 - \boldsymbol{a}_1 = a\left(-\frac{\sqrt{3}}{2}, -\frac{3}{2}\right), \tag{1.25}$$

$$\boldsymbol{b}_3 = \boldsymbol{a}_1 - \boldsymbol{a}_2 = a\left(-\frac{\sqrt{3}}{2}, \frac{3}{2}\right). \tag{1.26}$$

The resulting energy spectrum,

$$E_{\pm}(\mathbf{k}) = \pm|\mathbf{d}(\mathbf{k})|, \tag{1.27}$$

is fully gapped except at isolated points where the bulk gap closes.

To clarify the topological origin of this gap, it is useful to expand the Hamiltonian near the two inequivalent Dirac points $\mathbf{K}$ and $\mathbf{K}'$. The low-energy theory takes the Dirac form

$$H_{\eta}(\mathbf{q}) = v_F(\eta q_x \sigma_x + q_y \sigma_y) + m_{\eta}\sigma_z, \tag{1.28}$$

where $\eta = \pm 1$ label the valley degrees of freedom and

$$m_{\eta} = M - \eta\, 3\sqrt{3}\, t_2 \sin\phi. \tag{1.29}$$

The sign and relative magnitude of these Dirac mass terms play a central role in determining the topological character of the phase.

A topologically nontrivial phase arises when the Dirac masses at the two valleys acquire opposite signs. Since each massive Dirac cone contributes $\pm\frac{1}{2}$ to the Chern number depending on the sign of its mass, opposite mass signs cause the valley contributions to reinforce rather than cancel, resulting in a quantized Chern number $\nu = 1$.

$$\nu = \frac{1}{2}\left[\mathrm{sgn}(m_+) - \mathrm{sgn}(m_-)\right]. \tag{1.30}$$

The Berry curvature responsible for this invariant is strongly concentrated near the Dirac points, highlighting the low-energy origin of the topological response.

By tuning the staggered sublattice potential M or the complex next-nearest-neighbor hopping amplitude, the system can be driven through a topological phase transition. This transition occurs when the bulk energy gap closes at

$$M = \pm 3\sqrt{3}\, t_2 \sin\phi. \tag{1.31}$$

For parameter values satisfying

$$|M| < 3\sqrt{3}\, |t_2 \sin\phi|, \tag{1.32}$$

the system realizes a quantum anomalous Hall phase. In this regime, the Hall conductivity is quantized according to

$$\sigma_{xy} = \frac{e^2}{h}\, \nu, \tag{1.33}$$

and the nonzero Chern number guarantees the presence of chiral edge states that propagate unidirectionally along the boundary. These edge modes provide a direct manifestation of the bulk–edge correspondence.

1.2.3 Kane–Mele model: Time-reversal-invariant topology

The Kane–Mele model [32, 26] generalizes the Haldane model to spinful electrons and provides a minimal lattice realization of a time-reversal-invariant topological insulator. Instead of breaking time-reversal symmetry explicitly, the Kane–Mele model relies on intrinsic spin–orbit coupling to generate nontrivial topology while preserving time-reversal symmetry.

The Hamiltonian is given by

$$H_{\mathrm{KM}} = -t \sum_{\langle ij \rangle} c_i^\dagger c_j + i\lambda_{\mathrm{SO}} \sum_{\langle\langle ij \rangle\rangle} \nu_{ij}\, c_i^\dagger s^z c_j + \lambda_v \sum_i \xi_i\, c_i^\dagger c_i, \tag{1.34}$$

where λ_{SO} denotes the intrinsic spin–orbit coupling, s^z is the Pauli matrix in spin space, and λ_v is a staggered sublattice potential. The spin–orbit term effectively realizes two time-

reversed copies of the Haldane model, with opposite signs of the complex hopping for spin-up and spin-down electrons.

As a consequence, the total Chern number vanishes,

$$\nu = \nu_\uparrow + \nu_\downarrow = 0, \tag{1.35}$$

while the system remains topologically nontrivial. The topological character is instead captured by a $\mathbb{Z}_2$ invariant, which distinguishes the quantum spin Hall phase from a trivial insulator. In the nontrivial phase, the bulk gap is accompanied by robust helical edge states, in which counter-propagating modes carry opposite spin polarization. Time-reversal symmetry forbids elastic backscattering between these modes, ensuring their robustness against weak nonmagnetic disorder.

In the following sections, these lattice Hamiltonians serve as starting points for incorporating interactions and for exploring how topology is generated or reshaped in both uniform and spatially inhomogeneous systems.

1.3 Beyond the noninteracting picture

The lattice models discussed so far illustrate how noninteracting electrons can realize topological phases through band structure, symmetry, and lattice geometry. This framework has been highly successful and forms the foundation of topological band theory. In real materials, however, electrons are never truly noninteracting. Electron–electron interactions are always present and, in many systems, are comparable to or even stronger than the kinetic energy. Their presence fundamentally limits the applicability of a purely band-theoretic description.

Once interactions are taken into account, several important questions naturally arise. Can interactions destabilize an existing topological phase? How do they modify or reconstruct topological boundary states? More fundamentally, can interactions themselves

generate topological phases in systems that are topologically trivial at the noninteracting level? In the following, we first address the possibility of interaction-generated topology. This question is particularly fundamental, as it asks whether topology can arise purely from many-body effects rather than from single-particle band structure. We then turn to lattice models that exhibit topological order (Sections 1.4 and 1.5), and discuss how interactions reshape topological phases in both homogeneous and spatially inhomogeneous settings.

1.3.1 Can interactions generate topology?

A more subtle and conceptually important possibility is that electron–electron interactions may themselves generate topological phases, even when the underlying noninteracting band structure is topologically trivial. In such cases, topology does not originate from explicit band parameters or spin–orbit coupling, but instead emerges spontaneously as a consequence of interaction-driven symmetry breaking. This idea was proposed in a seminal work by Raghu *et al.* [3], who demonstrated that repulsive interactions on a simple lattice can stabilize a quantum anomalous Hall phase through spontaneous current formation.

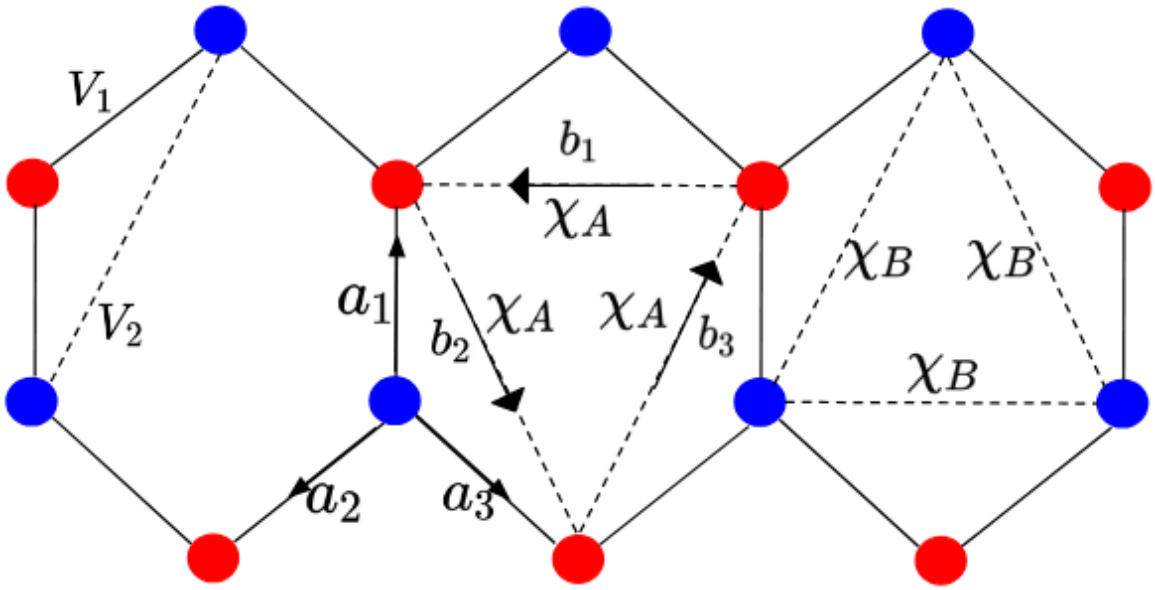

Figure 1.5: Interacting lattice model in honeycomb geometry

The essential setting is the honeycomb lattice as shown in Fig. 1.5 at half filling, whose noninteracting limit hosts Dirac cones at the corners of the Brillouin zone. For spinless fermions, the interacting Hamiltonian can be written as

$$H = -t \sum_{\langle ij \rangle} \left(c_i^\dagger c_j + \text{h.c.} \right) + V_1 \sum_{\langle ij \rangle} (n_i - 1)(n_j - 1) + V_2 \sum_{\langle\langle ij \rangle\rangle} (n_i - 1)(n_j - 1), \quad (1.36)$$

where t denotes nearest-neighbor hopping, while V_1 and V_2 represent nearest- and next-nearest-neighbor repulsive interactions, respectively. At weak coupling, the system remains a Dirac semimetal with a vanishing density of states at the Fermi level. As a result, infinitesimal interactions do not immediately destabilize the semimetal. However, the nature of the leading instability depends sensitively on the range of the interactions. Nearest-neighbor repulsion V_1 favors a conventional charge density wave that breaks sublattice symmetry and produces a trivial insulating state. In contrast, next-nearest-neighbor repulsion V_2 opens the possibility of a different instability rather than simple charge ordering. Decoupling the V_2 interaction in the bond channel introduces a complex bond expectation value on second-neighbor links,

$$\chi_{ij} = \langle c_i^\dagger c_j \rangle, \quad (1.37)$$

which can acquire a purely imaginary component. A nonzero imaginary χ_{ij} corresponds to circulating currents around the hexagonal plaquettes and spontaneously breaks time-reversal symmetry while preserving translational invariance. At the mean-field level, this generates an effective complex next-nearest-neighbor hopping term that is formally identical to the Haldane model.

The resulting mean-field Hamiltonian therefore takes the form

$$H_{\text{MF}} = -t \sum_{\langle ij \rangle} c_i^\dagger c_j - \sum_{\langle\langle ij \rangle\rangle} t_2^{\text{eff}} e^{i\nu_{ij}} c_i^\dagger c_j + \text{h.c.}, \quad (1.38)$$

where the effective hopping amplitude $t_2^{\text{eff}} \propto V_2 \,\text{Im}\, \chi_{ij}$ is generated spontaneously by interactions. Importantly, there is no explicit time-reversal-breaking term in the original Hamil-

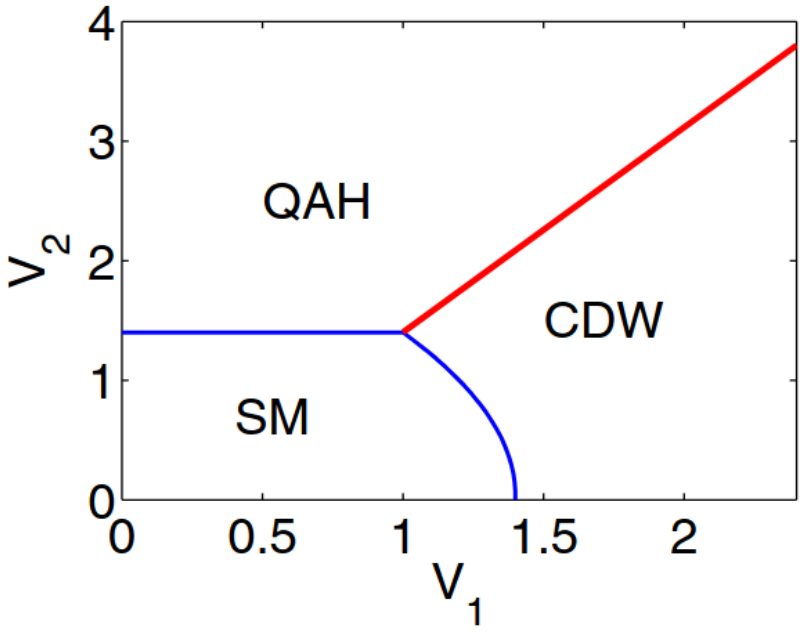

Figure 1.6: Phase diagram at half filling of spinless interacting fermions on the honeycomb lattice [3].

tonian, the topological mass arises entirely from many-body effects.

This interaction-generated hopping opens a gap at the Dirac points and produces a quantum anomalous Hall (QAH) insulating phase characterized by a nonzero Chern number and chiral edge states (Fig. 1.6). Because the insulating gap is driven by interactions rather than band structure, this phase is often referred to as a *topological Mott insulator* [3, 33, 34].

Despite its conceptual novelty, several unbiased numerical studies [10, 11, 12, 35, 36, 37, 38] have revealed important limitations of interaction-generated quantum anomalous Hall phases. Exact diagonalization, density-matrix renormalization group, and quantum Monte Carlo calculations on closely related honeycomb lattice models consistently show that, over most of the parameter space, repulsive interactions favor more conventional symmetry-breaking phases, such as charge density wave order or magnetism, rather than topological order. In fact, in these unbiased studies, an interaction-driven quantum anomalous Hall phase is absent. The central lesson is that strong correlations do not generically

generate topological phases. Rather, interaction-induced topological order must compete with and overcome conventional, topologically trivial symmetry-breaking states. This observation motivates the search for lattice settings in which such competing orders are weakened or energetically disfavored. Systems hosting quadratic band-touching points provide a particularly promising platform, as their enhanced density of states increases the susceptibility to interaction-driven instabilities and can tip the balance in favor of topological phases, as discussed next.

1.3.2 Dirac points versus quadratic band touching

A key factor that controls whether electron–electron interactions can generate topological phases is the low-energy density of states near the Fermi level. This becomes particularly clear when comparing systems hosting Dirac points with those exhibiting quadratic band touching (QBT) points. In two-dimensional Dirac systems, the low-energy dispersion is linear,

$$E(\mathbf{k}) \sim |\mathbf{k}|, \tag{1.39}$$

which implies a vanishing density of states at the Fermi energy,

$$\rho_{\text{Dirac}}(E) \propto |E|, \qquad \rho_{\text{Dirac}}(0) = 0. \tag{1.40}$$

As the Fermi level is approached, the available phase space for scattering processes rapidly diminishes. Consequently, short-range interactions become increasingly ineffective at low energies and are perturbatively irrelevant at weak coupling from a renormalization-group perspective.

This suppression of interaction effects stabilizes the Dirac semimetal at weak coupling. Although mean-field approaches may suggest interaction-driven instabilities, unbiased numerical studies show that Dirac systems remain stable until interactions become sufficiently strong. Even then, the resulting phases are typically conventional symmetry-breaking insu-

lators, such as magnetic or charge-ordered states, rather than interaction-generated quantum anomalous Hall phases. In this sense, Dirac dispersions are generally unfavorable for realizing topology that emerges purely from interactions.

Quadratic band touching points present a contrasting situation. Here, the low-energy dispersion is quadratic,

$$E(\mathbf{k}) \sim k^2, \tag{1.41}$$

leading to a finite density of states at the Fermi level,

$$\rho_{\mathrm{QBT}}(E) \simeq \rho_0 \neq 0, \qquad \rho_{\mathrm{QBT}}(0) = \rho_0. \tag{1.42}$$

The presence of a finite density of states strongly enhances interaction effects. Even weak short-range interactions in renormalization group sense [39, 40] become marginally relevant and destabilize the noninteracting fixed point.

In sum, a quadratic band touching point is intrinsically unstable in the presence of interactions [39, 41, 42, 43, 44, 45], and the system is driven toward some form of symmetry breaking. Which ordered phase ultimately emerges depends on the available interaction channels and the underlying lattice symmetries. In spinless systems, several unbiased theoretical studies of quadratic band touching points on checkerboard [13, 46], Lieb, bilayer graphene [14, 15, 16, 47, 48] and kagome lattices [49, 50, 51, 52, 53, 54] identify time-reversal-symmetry-breaking instabilities as leading candidates. In this scenario, interactions spontaneously generate a topological mass term that gaps the spectrum and realizes a quantum anomalous Hall phase with chiral edge states. Other competing orders, such as nematic or charge density wave phases, may also develop and remain close in energy, leading to strong competition in this regime. Therefore, the density-of-states-controlled distinction explains why lattice models hosting quadratic band touching points, such as generalized two-dimensional SSH-type models, form an essential part of this thesis which will be explored in a later chapter.

1.3.3 Other competing orders and the role of nematicity

Interaction-generated topology never emerges in isolation. Near band degeneracies, multiple symmetry-breaking channels compete for the same low-energy degrees of freedom. Common competing orders are charge density wave order, magnetic order (in case of spinful models), and nematic order.

Nematicity corresponds to the spontaneous breaking of lattice rotational symmetry while preserving translational invariance. In lattice systems, nematic order can arise through anisotropic renormalization of hopping amplitudes (bond nematicity) or through unequal on-site potentials within the unit cell (site nematicity). Bond nematicity typically reconstructs the dispersion without opening a full gap, often splitting a quadratic band touching into Dirac cones. Site nematicity, by contrast, usually opens a gap (via reducing rotational symmetry) and produces an insulating phase.

From an energetic standpoint, nematic order can be favored at weak to intermediate interaction strengths because it lowers the kinetic energy efficiently without immediately opening a gap or generating Berry curvature. As a result, many interacting phase diagrams exhibit nematic phases that prevent or compete with quantum anomalous Hall order. Small changes in interaction range, lattice anisotropy, or band structure can tip the balance between these competing outcomes.

These considerations point to an important lesson. While electron–electron interactions can, in principle, generate topological phases in systems that are trivial at the band level, this does not happen in a generic way. Interaction-driven topology must compete with more conventional symmetry-breaking tendencies, and whether it ultimately emerges depends strongly on the low-energy electronic structure, especially the density of states and the nature of band degeneracies. Systems with quadratic band touching are therefore particularly significant, since their finite density of states makes interactions effective already

at weak coupling and places nematic, charge-ordered, and topological instabilities on an equal footing. This close competition is precisely what motivates the study of generalized two-dimensional SSH-type lattice models, which naturally host quadratic band touching points and provide a controlled setting to explore how interactions choose between nematic order and interaction-induced topological phases.

1.4 Effects of interaction on band topology

In the previous section, we discussed how electron–electron interactions can *generate* topological phases starting from a topologically trivial noninteracting band structure. In this section, we shift focus to a complementary question: how interactions affect topological phases already present in the noninteracting limit in lattice systems. We begin with homogeneous, translationally invariant models, where the role of interactions can be studied in a clean and controlled setting, free from the additional complications introduced by spatial inhomogeneity. We then move on to heterostructures in the next section, where translational symmetry is explicitly broken. These uniform systems provide valuable reference points for understanding how correlations renormalize, compete with, or finally destabilize topological phases that originate at the band-structure level.

Two important models discussed in this context are the Kane–Mele–Hubbard model and the Bernevig–Hughes–Zhang (BHZ)–Hubbard model. Both extend well-established noninteracting topological band structures by incorporating local Hubbard interactions, but they differ in the microscopic origin of their topology and in the way their topological phases respond to electron–electron interactions.

1.4.1 Kane–Mele–Hubbard and Bernevig–Hughes–Zhang–Hubbard models

The Kane–Mele–Hubbard and Bernevig–Hughes–Zhang (BHZ)–Hubbard models provide two well-established and complementary settings for understanding how electron–electron interactions affect pre-existing topological phases in uniform lattice systems. In both cases, topology is already present at the noninteracting level and is protected by time-reversal symmetry, while interactions act as an additional ingredient that can renormalize or ultimately destabilize the topological state.

In the Kane–Mele–Hubbard model [55, 56, 57, 58, 59], the noninteracting limit features intrinsic spin–orbit coupling that opens a bulk gap on the honeycomb lattice and gives rise to a quantum spin Hall phase with helical edge states. Extensive numerical studies, most notably quantum Monte Carlo simulations, show that this phase is robust against weak and intermediate Hubbard interactions. In this regime, interactions mainly renormalize single-particle properties such as the bulk gap, quasiparticle weight, and edge-state velocity, while the topological character remains unchanged. At stronger coupling, antiferromagnetic order develops. Once magnetism sets in, time-reversal symmetry is broken, the helical edge states become gapped, and the system crosses into a topologically trivial insulating phase. The loss of topology therefore occurs not gradually, but as a direct consequence of magnetic ordering.

The BHZ–Hubbard model [60, 61, 62, 63] follows a similar overall pattern but through a different microscopic route. Here, topology originates from band inversion between orbitals of opposite parity rather than from lattice geometry. Dynamical mean-field theory studies show that the system remains a topological insulator at weak to intermediate interaction strengths, with the $\mathbb{Z}_2$ invariant unchanged. However, correlations act directly on the inverted band structure itself. In the low-energy Dirac-like description of the BHZ model,

topology is controlled by a mass parameter that determines the relative energy ordering of the electron- and hole-like orbitals. The sign of this mass distinguishes the topological and trivial insulating phases, as it encodes whether band inversion is present. Electronic interactions renormalize this mass parameter by modifying the orbital energies through the self-energy correction. As the interaction strength increases, the renormalized mass is gradually driven toward zero, thereby reducing the degree of band inversion. When it eventually changes sign, the band ordering is restored to the trivial configuration, and a topological phase transition occurs even in the absence of symmetry breaking. Well before this transition, the edge states already show strong correlation effects, including reduced coherence and modified dispersion, while time-reversal symmetry remains intact.

A important theme common to both models is the enhanced sensitivity of boundary states to interactions. Even when the bulk remains topological, edge states can undergo substantial reconstruction. In some regimes, the outermost layers become strongly renormalized or locally insulating, while the bulk stays gapped and topological. The helical edge modes then effectively shift inward rather than disappearing immediately. Only at stronger coupling, when magnetic order develops and consequently time-reversal symmetry is broken, the edge states become fully gapped, leading to destruction of the topological phase.

Together, these models serve as clean reference points for understanding how interactions reshape band-derived topological phases in uniform systems. They demonstrate both the robustness of topology at weak coupling and the indirect ways in which strong correlations can eventually destabilize it. At the same time, these results highlight that qualitatively new correlation-driven phenomena are more likely to emerge in settings that extend beyond uniform bulk systems, thereby motivating the study of spatially inhomogeneous structures and interfaces discussed in the following section.

1.5 Interfaces and heterostructures: Correlated topological matter

Studies of interacting lattice models show that electron–electron interactions can substantially modify topological phases and, at strong coupling, may even destroy them through symmetry breaking. While uniform bulk systems provide conceptual clarity, many of the most striking phenomena emerge at interfaces, where translational symmetry is broken and electronic properties vary across only a few lattice spacings. In heterostructures, charge density, screening strength, and effective interaction parameters change from layer to layer, producing electronic states that cannot be understood as a simple combination of the two bulk materials. Interfaces therefore provide a natural setting in which topology, correlations, and electronic reconstruction meet.

Oxide heterostructures offer clear demonstrations of such interfacial reconstruction. A prominent example is the $LaAlO_3/SrTiO_3$ interface [19], where a high-mobility two-dimensional electron gas forms even though both constituents are insulating in the bulk. This metallic state does not arise from simple band alignment; instead, it results from electronic reconstruction driven by polar discontinuity and long-range Coulomb interactions [17, 18]. Remarkably, the same interface can host superconductivity [64], magnetism [65], and strong magnetoresistance [66]. These observations make clear that interfaces are extended correlated regions in which charge, spin, and orbital degrees of freedom reorganize over several layers [67].

Correlated heterostructures [68, 69, 70, 71, 72, 73, 74] display similar physics. At Mott insulator–band insulator interfaces, mismatches in chemical potential and screening drive charge transfer across the boundary [70, 74]. Metallic states may then emerge within only a few layers, even when both bulk materials remain insulating. These interfacial metals are often strongly renormalized and may coexist with magnetic order. Related behavior appears

in Mott insulator–metal systems [71], where itinerant carriers from the metallic side screen localized moments in the correlated region, potentially giving rise to Kondo-like physics. In all these cases, interfaces host emergent phases absent in either bulk constituent.

When one of the materials is topological, additional possibilities arise. Topological insulators support boundary states protected by bulk invariants and symmetries, yet once placed in contact with another material, these states become sensitive to proximity effects. In TI–superconductor heterostructures [75, 76], superconducting correlations are induced in the helical edge or surface states, opening a gap and potentially generating Majorana bound states. Interfaces between topological insulators and ferromagnets [77, 78, 79] provide a complementary route: magnetic proximity breaks time-reversal symmetry and can gap the boundary spectrum, leading to quantum anomalous Hall states. Heterostructures between distinct topological insulators [80] further show that boundary modes can hybridize or reorganize when topological indices differ across an interface. In most of these settings, however, interactions are treated as weak or symmetry breaking is externally imposed.

A qualitatively different situation arises at topological insulator–Mott insulator interfaces, where topological boundary states encounter electrons localized by strong Coulomb repulsion. Inhomogeneous dynamical mean-field theory studies [81, 82] show that boundary states need not simply disappear. Instead, the effective topological phase boundary can shift into the correlated region, producing so-called buried edge states. In one scenario, helical modes penetrate the Mott insulator and evolve into strongly renormalized midgap states with heavy-fermion-like character [81]. In another, when the Mott transition is first order and spin–orbit coupling is present on both sides [82], several correlated layers become topologically nontrivial, effectively relocating the boundary. These results demonstrate that strong correlations can reconstruct and reposition topological boundary modes rather than merely suppressing them.

Taken together, these developments emphasize that interfaces are active, self-consistently

reconstructed regions where topology and strong correlations interact. Charge transfer, screening, and many-body renormalization can generate metallic or ordered states confined to only a few layers. When topology is involved, boundary states become dynamical quantities whose spatial location and spectral properties are shaped by interaction-driven reconstruction. Understanding this interplay is therefore essential for exploring genuinely correlated topological heterostructures.

1.5.1 Limitations

Despite significant progress, current theoretical approaches to topological insulator–Mott insulator heterostructures still suffer from limitations. Most existing studies rely on inhomogeneous dynamical mean-field theory restricted to paramagnetic solutions. As a result, spontaneous magnetic ordering and magnetic reconstruction at the interface are explicitly suppressed. This is a serious limitation, since topological boundary states are inherently sensitive to magnetism, and even weak time-reversal symmetry breaking can qualitatively reshape helical edge modes. Consequently, key questions related to spatially varying magnetization, spin imbalance, and symmetry-breaking reconstruction of boundary states remain largely unexplored.

These limitations directly motivate the approach adopted in this thesis. By combining real-space Hartree–Fock theory with slave-rotor methods, it becomes possible to treat charge redistribution, strong correlations, and magnetic ordering on equal footing, without imposing paramagnetic constraints. This framework allows access to regimes in which weak, proximity-induced magnetization reconstructs topological boundary states without fully destroying their topological origin. In particular, it enables the study of intermediate phases characterized by spin-imbalanced helical edge modes, opening the door to interaction-driven spin-to-charge current conversion at topological insulator–Mott insulator interfaces. The detailed investigation of these effects forms the basis of the following

chapters.

1.6 Motivation and research questions

The discussions in the preceding sections establish a coherent picture of how topology, interactions, and spatial inhomogeneity shape quantum phases of matter. While noninteracting band theory provides a powerful framework for classifying topological phases, it becomes insufficient once strong electron–electron interactions and broken translational symmetry are taken into account. Interactions can renormalize, compete with, or even generate topological phases, and interfaces provide natural settings in which these effects are amplified.

This thesis is motivated by the observation that two complementary aspects of correlated topological matter remain only partially understood. First, although interaction-generated topology has been theoretically proposed and analyzed in specific lattice models, its realization is highly constrained and competes strongly with more conventional symmetry-breaking orders. Identifying the conditions under which interactions favor topological order over nematic or charge-ordered phases requires controlled lattice settings and careful analysis of competing instabilities. Second, while topological boundary states are known to be robust against weak perturbations, their behavior in strongly correlated and spatially inhomogeneous environments remains far less explored, particularly when magnetic reconstruction is allowed to emerge self-consistently.

These considerations lead to the following central questions that are investigated in this thesis:

- Under what conditions can electron–electron interactions spontaneously generate topological phases in lattice systems that are topologically trivial at the band level?
- How does lattice geometry, and in particular the presence of Dirac or quadratic band

touching points, control the competition between topological order and symmetry-breaking instabilities such as nematicity and charge order?

- How do strong correlations modify the structure of topological boundary states in spatially inhomogeneous settings?
- Can proximity-induced magnetism reconstruct helical edge states without fully destroying their topological character?
- Is it possible for interaction-driven reconstruction at interfaces to enable new transport phenomena, such as spin-to-charge current conversion?

To address these questions, the thesis is organized around two complementary lines of investigation. First, it examines interaction effects in uniform lattice models, using generalized two-dimensional Su–Schrieffer–Heeger models as controlled settings to study how interactions lift band degeneracies and select between competing phases. Special emphasis is placed on quadratic band touching points, where the finite density of states makes interactions effective and allows interaction-generated topological phases to compete directly with nematic and charge-ordered states.

The second direction focuses on spatially inhomogeneous systems, specifically heterostructures formed by interfacing topological insulators with Mott insulators. Here, topological boundary states are exposed to strong local correlations and magnetic reconstruction. Using real-space self-consistent Hartree–Fock theory combined with slave-rotor methods, the work explores regimes beyond paramagnetic mean-field approaches and identifies intermediate phases with spin-imbalanced yet topologically derived edge modes.

1.7 Outline of the thesis

The remainder of this thesis is organized as follows.

Chapter 2 introduces the theoretical framework employed throughout this work, including the formulation of the interacting lattice models and the numerical implementation of the Hartree–Fock and slave-rotor methods.

Chapter 3 investigates interaction-driven topological phases in generalized two-dimensional Su–Schrieffer–Heeger (SSH) models. It presents the lattice geometries and interaction terms considered in this study and analyzes how electron–electron interactions can induce spontaneous symmetry breaking and generate topological phases beyond the noninteracting band picture.

Chapter 4 is devoted to the study of topological insulator–Mott insulator interfaces in the Lieb lattice setting. This chapter examines how strong correlations, charge redistribution, and magnetic reconstruction reshape topological boundary states, leading to phenomena such as buried edge modes and interaction-driven spin imbalance at interfaces.

Chapter 5 summarizes the main results of the thesis and places them in a broader perspective. It discusses the implications of these findings for correlated topological matter and outlines possible directions for future research.

Chapter 2

Theoretical formalism and computational methods

The primary aim of this thesis is to understand how electron–electron interactions modify and give rise to topological phases in two-dimensional quantum systems. While noninteracting topological materials can often be described using band theory and topological invariants, interactions introduces significant complexity that makes an exact treatment of large systems challenging. To address this problem, we employ self-consistent mean-field approaches that provide a practical way to study correlation effects and their influence on edge states, interfaces, and interaction-driven topological phenomena. We begin by introducing a generalized lattice Hamiltonian that serves as the foundation for the SSH-type lattices and heterostructures considered in this work. We then present the Hartree–Fock (HF) and slave-rotor (SR) mean-field methods used throughout the thesis to investigate symmetry-breaking instabilities, emergent phase diagrams, Mott localization, and strong-correlation effects. Finally, we introduce the Chern number used to characterize topological phases and outline the formalism for calculating Green's functions and current operators.

2.0.1 Generalized interacting lattice Hamiltonian

All models studied in this thesis can be formulated within a generic lattice Hamiltonian of the form

$$\mathcal{H} = \mathcal{H}_0 + \mathcal{H}_{\text{int}} + \mathcal{H}_{\text{LRC}}, \tag{2.1}$$

where $\mathcal{H}_0$ describes the noninteracting band structure, $\mathcal{H}_{\text{int}}$ contains the short-range or onsite electron–electron interactions, and $\mathcal{H}_{\text{LRC}}$ accounts for long-range Coulomb effects that is

essential in spatially inhomogeneous systems.

The single-particle part is written as

$$\mathcal{H}_0 = -\sum_{i,j,\sigma} \left(t_{ij} c^\dagger_{i\sigma} c_{j\sigma} + \text{h.c.} \right) + \sum_{i,\sigma} (\epsilon_i - \mu)\, n_{i\sigma}, \tag{2.2}$$

where t_{ij} specifies the nearest- and next-nearest-neighbor hopping amplitudes, including complex next-nearest-neighbor spin-orbit coupling term that opens topological gaps, ϵ_i represents sublattice dependent on-site potentials and μ is chemical potential.

In heterostructures and interface geometries, charge redistribution plays a important role. To prevent unphysical charge accumulation and to capture electrostatic reconstruction, long-range Coulomb interactions are included at the mean-field level [83, 84],

$$\mathcal{H}_{\text{LRC}} = \sum_i \phi_i n_i, \tag{2.3}$$

where the electrostatic potential ϕ_i is determined self-consistently from mean-field parameters as follows,

$$\phi_i = \sum_{j \neq i} a_M\, t\, \frac{\langle n_j \rangle - Z_{\text{ion}}}{|\mathbf{r}_i - \mathbf{r}_j|}. \tag{2.4}$$

Here a_M denotes the Madelung constant that accounts for the lattice geometry, Z_{ion} represents the positive ionic background charge, and t sets the overall energy scale. This term captures electrostatic reconstruction and realistic charge redistribution across correlated heterostructures.

2.1 Hartree–Fock mean field method

Electron–electron interactions play a important role in all lattice models studied in this thesis. To treat these interactions in a controlled yet flexible manner, we employ *Hartree–Fock (HF) theory* as the primary numerical approach. Within this framework, interacting many-body terms are decoupled into effective single-particle contributions that depend

self-consistently on expectation values such as local density, bond amplitudes, and magnetization. The resulting quadratic Hamiltonian is solved iteratively until self-consistency is achieved. Depending on the degrees of freedom and the physical problem under consideration, two distinct interaction decoupling schemes are employed, as described below.

2.1.1 Spinless fermions with extended interactions

For the generalized SSH models, we consider spinless fermions interacting via short-range repulsive density–density interactions. The interaction Hamiltonian is given by

$$\mathcal{H}_{\text{int}}^{\text{SSH}} = \frac{1}{2}\sum_{i\neq j} V_{ij}\, n_i n_j, \tag{2.5}$$

where V_{ij} denotes nearest-neighbor and next-nearest-neighbor repulsion.

To capture interaction-driven phases such as the quantum anomalous Hall (QAH) state and bond-nematic order, the interaction is decoupled in the both Hartree and Fock channels,

$$n_i n_j \approx \langle n_i\rangle n_j + n_i\langle n_j\rangle - \langle n_i\rangle\langle n_j\rangle - \left(\chi_{ji}c_i^\dagger c_j + \chi_{ij}c_j^\dagger c_i - |\chi_{ij}|^2\right),$$

where $\chi_{ij} = \langle c_i^\dagger c_j\rangle$ is the bond order parameter.

This decoupling allows interactions to dynamically renormalize hopping amplitudes and, when appropriate, generate complex bond expectation values. An imaginary component of χ_{ij} corresponds to spontaneous loop currents and signals QAH order, while anisotropy in its real component reflects bond-nematic symmetry breaking. The Hartree terms simultaneously capture charge redistribution and charge-density-wave tendencies.

The resulting Hartree–Fock Hamiltonian reads

$$\mathcal{H}_{\text{HF}} = \sum_{i,j}\left(-t_{ij} - V_{ij}\chi_{ij}^*\right)c_i^\dagger c_j + \sum_i\left(\epsilon_i + \sum_{j\neq i} V_{ij}\langle n_j\rangle\right)n_i. \tag{2.6}$$

2.1.2 Spinful fermions with on-site Hubbard interaction

For the heterostructure system, we consider spinful fermions subject to a local Hubbard interaction,

$$\mathcal{H}_{\text{int}}^{\text{Het}} = U \sum_i n_{i\uparrow} n_{i\downarrow}. \tag{2.7}$$

In the strongly interacting regime, magnetic correlations and Mott physics become central to the low-energy behavior.

Within Hartree–Fock theory, the onsite interaction is decoupled in the density (Hartree) channel as

$$n_{i\uparrow} n_{i\downarrow} \approx \langle n_{i\uparrow} \rangle n_{i\downarrow} + \langle n_{i\downarrow} \rangle n_{i\uparrow} - \langle n_{i\uparrow} \rangle \langle n_{i\downarrow} \rangle. \tag{2.8}$$

Accordingly, the interaction term becomes

$$U n_{i\uparrow} n_{i\downarrow} \approx U \Big(\langle n_{i\uparrow} \rangle n_{i\downarrow} + \langle n_{i\downarrow} \rangle n_{i\uparrow} \Big) - U \langle n_{i\uparrow} \rangle \langle n_{i\downarrow} \rangle. \tag{2.9}$$

The last term represents a constant energy shift and does not affect the eigenstates. The resulting mean-field Hamiltonian can therefore be written as

$$\mathcal{H}_{\text{HF}} = -\sum_{i,j,\sigma} \Big(t_{ij} c_{i\sigma}^\dagger c_{j\sigma} + \text{h.c.} \Big) + \sum_{i,\sigma} \left[\epsilon_i + U \langle n_{i\bar{\sigma}} \rangle \right] n_{i\sigma} + \text{const.} \tag{2.10}$$

Each spin species thus experiences an effective on-site potential generated by the opposite spin, $\epsilon_{i\sigma}^{\text{eff}} = U \langle n_{i\bar{\sigma}} \rangle$. The local charge density and spin polarization are determined self-consistently, enabling a unified description of interfacial charge reconstruction and interaction-driven magnetism.

2.1.3 Self-consistency, initial conditions, and competing solutions

The Hartree–Fock equations are solved using an iterative self-consistency procedure. Starting from an initial guess for the mean-field parameters, the effective Hamiltonian is diagonalized, expectation values are recalculated, and the procedure is repeated until convergence is achieved.

Because Hartree–Fock theory admits multiple locally stable solutions corresponding to different symmetry-breaking patterns, the choice of initial conditions plays an important role. To ensure that the physically relevant ground state is identified, several distinct initial configurations are explored. For each converged solution, the total Hartree–Fock energy is evaluated and the state with the lowest energy is selected. To improve numerical stability and avoid oscillatory behavior, the update of mean-field parameters is performed using linear mixing between successive iterations.

2.1.4 Limitations

Hartree–Fock theory provides a transparent and intuitive framework for identifying interact ion-driven instabilities, symmetry breaking, and spatial reconstruction in lattice models. Although it does not capture quantum fluctuations, it is particularly well suited for studying lattice-scale ordering, edge states, and heterostructures. In strong regimes where strong local charge fluctuations become essential, Hartree–Fock is complemented by slave-rotor mean-field theory, which is discussed in the following section.

2.2 Slave-rotor mean-field theory

While Hartree-Fock captures magnetic symmetry breaking, it fails to describe the paramagnetic Mott transition and neglects local charge fluctuations. To validate the survival of edge states in the strong-coupling regime (chapter 4), we employ the **Slave-Rotor (SR)** mean-field theory.

Rotor decomposition and constraint: We decompose the physical electron creation operator $d_{i\sigma}^{\dagger}$ into a neutral fermionic spinon $f_{i\sigma}^{\dagger}$ (carrying spin) and a charged bosonic rotor $e^{-i\theta_i}$ (carrying charge):

$$d_{i\sigma}^{\dagger} = f_{i\sigma}^{\dagger} e^{-i\theta_i}, \quad d_{i\sigma} = f_{i\sigma} e^{i\theta_i} \tag{2.11}$$

To maintain the physical Hilbert space, we impose the local constraint:

$$\sum_{\sigma} f_{i\sigma}^{\dagger} f_{i\sigma} + L_i = 1 \tag{2.12}$$

where $L_i = -i\frac{\partial}{\partial\theta_i}$ is the angular momentum of the rotor, representing the deviation from half-filling.

Coupled effective Hamiltonians: Substituting this decomposition leads to two coupled Hamiltonians solved self-consistently:

1. The spinon Hamiltonian ($\mathcal{H}_f$): The spinons describe a fermionic system where the hopping is renormalized by the coherence of the rotors:

$$\mathcal{H}_f = -\sum_{i,j,\sigma} \left(t_{ij} \langle e^{i(\theta_i - \theta_j)} \rangle f_{i\sigma}^{\dagger} f_{j\sigma} + h.c. \right) + \sum_{i,\sigma} (h_i - \mu_f) n_{i\sigma}^{f} \tag{2.13}$$

Here, $\langle e^{i(\theta_i - \theta_j)} \rangle$ acts as a renormalization factor that modifies the effective hopping amplitude of the spinons. In the Mott phase, the rotor condensate vanishes, suppressing coherent quasiparticle hopping and leading to a charge-localized insulating state. The quantity h_i is a site-dependent Lagrange multiplier enforcing the slave-rotor constraint and effectively acts as a local chemical potential for the spinons.

2. The rotor Hamiltonian ($\mathcal{H}_\theta$): The interactions are carried entirely by the rotor degrees of freedom:

$$\mathcal{H}_\theta = -\sum_{i,j} \left(J_{ij} e^{-i(\theta_i - \theta_j)} + h.c. \right) + \frac{U}{2} \sum_i L_i^2 + \sum_i h_i^{\theta} L_i \tag{2.14}$$

Here $J_{ij} = t_{ij} \sum_\sigma \langle f_{i\sigma}^{\dagger} f_{j\sigma} \rangle$ acts as an effective kinetic coupling generated by the spinon sector. The term h_i^{θ} is the corresponding Lagrange multiplier in the rotor sector, which couples to the rotor angular momentum L_i and enforces the local constraint between the spinon occupation and the rotor charge degree of freedom. Similar to the spinon sector, this parameter is obtained self-consistently in the mean-field solution.

Real-space cluster solution: Since the heterostructure breaks translational invariance, we employ a **Cluster Mean-Field Theory**. We define a cluster of unit cells and treat intra-cluster rotor interactions exactly by diagonalizing the cluster Hamiltonian, while treating inter-cluster couplings at the mean-field level.

Many-body Green's function reconstruction: At the mean-field level the physical electron Green's function approximately factorizes into spinon and rotor correlators

$$G_{i\sigma}(\tau) \approx -\langle \mathcal{T}_\tau f_{i\sigma}(\tau) f^\dagger_{i\sigma}(0)\rangle \langle \mathcal{T}_\tau e^{i\theta_i(\tau)} e^{-i\theta_i(0)}\rangle, \tag{2.15}$$

where gauge fluctuations are neglected. Using the spectral representations of the spinon and rotor propagators, we obtain the electron Green's function in frequency space. The resulting spectral function exhibits a coherent quasiparticle peak in the metallic phase and the emergence of upper and lower Hubbard bands in the Mott insulating regime.

Self-consistent numerical procedure

All calculations are performed in real space on finite lattices with close boundary conditions along the interface direction and periodic boundary conditions along the translationally invariant direction. Starting from an initial guess for all mean-field variables, the effective single-particle Hamiltonian is constructed and diagonalized.

Expectation values of charge density, bond order parameters, and rotor condensates are computed from the eigenstates and fed back into the Hamiltonian. This procedure is iterated until self-consistency is achieved, defined by convergence of all local order parameters below a prescribed tolerance. Physical observables are evaluated using the converged solution.

2.3 Topological invariants

For topological characterization of the QAH phase, we compute the Chern number C using the method developed by Fukui, Hatsugai, and Suzuki (FHS) [85] on a discrete Brillouin zone. We define the $U(1)$ link variable $U_\mu(\mathbf{k}_l)$ from the normalized overlap of ground state wavefunctions:

$$U_\mu(\mathbf{k}_l) = \frac{\langle\Psi(\mathbf{k}_l)|\Psi(\mathbf{k}_l+\hat{\mu})\rangle}{|\langle\Psi(\mathbf{k}_l)|\Psi(\mathbf{k}_l+\hat{\mu})\rangle|} \tag{2.16}$$

The lattice Berry flux $\tilde{F}_{xy}(\mathbf{k}_l)$ is given by the gauge-invariant product of link variables around a plaquette:

$$\tilde{F}_{xy}(\mathbf{k}_l) = \ln\left(U_x(\mathbf{k}_l)U_y(\mathbf{k}_l+\hat{x})U_x(\mathbf{k}_l+\hat{y})^{-1}U_y(\mathbf{k}_l)^{-1}\right) \tag{2.17}$$

The total Chern number is the sum of the flux over the Brillouin zone:

$$C = \frac{1}{2\pi i}\sum_l \tilde{F}_{xy}(\mathbf{k}_l) \tag{2.18}$$

This method ensures strictly integer results even for coarse discretization.

2.4 Current operators

To characterize the edge-state transport properties of the heterostructures studied in this thesis, we calculate the local bond currents. The current operator is obtained from the continuity equation, $\frac{dn_i}{dt} = i[\mathcal{H}, n_i]$, which relates the time evolution of the local charge density to the flow of particles between neighboring sites. The current flowing from site j to site i is given by

$$J_{ij} = -i\sum_\sigma \left(t_{ij}d^\dagger_{i\sigma}d_{j\sigma} - t_{ji}d^\dagger_{j\sigma}d_{i\sigma}\right). \tag{2.19}$$

To distinguish between charge and spin transport, the expectation value of the current is decomposed into its charge and spin components,

$$J^c = J_\uparrow + J_\downarrow, \qquad J^s = J_\uparrow - J_\downarrow. \tag{2.20}$$

This decomposition is particularly useful for identifying the conversion of spin currents into charge currents in correlated topological heterostructures.

The theoretical framework developed in this chapter provides the foundation for the studies presented in the remainder of the thesis. In the following chapters, it is applied to generalized two-dimensional SSH models to investigate interaction-driven nematic and quantum anomalous Hall phases, and to topological insulator–Mott insulator heterostructures to explore magnetic reconstruction, charge redistribution, and the emergence of spin-imbalanced edge modes.

Chapter 3

Quantum phases in two dimensional generalized interacting SSH model

In chapter 1, we established that while band topology provides a powerful framework for classifying quantum phases, it remains fundamentally formulated within a single-particle picture. Electron–electron interactions introduce many-body effects that can either destabilize, reconstruct, or even spontaneously generate topological phases. However, interaction-driven topology does not arise generically, as the same interactions may also favor conventional symmetry-breaking orders such as charge-density-wave or nematic phases. Identifying the conditions under which topology emerges therefore requires lattice models whose low-energy electronic structure amplifies interaction effects.

Semimetallic systems with symmetry-protected band degeneracies provide particularly fertile ground for such studies. Among them, quadratic band touching (QBT) points play a special role. Unlike Dirac points, which possess a vanishing density of states at the Fermi level, QBT points exhibit a finite density of states, rendering them unstable to arbitrarily weak interactions. This enhanced susceptibility opens a window for interaction-driven instabilities to emerge already at weak to intermediate coupling.

In this chapter, we investigate interaction-driven quantum phases in a two-dimensional generalized Su–Schrieffer–Heeger (SSH) model defined on a square lattice. This model provides a minimal and highly tunable platform that can host either a QBT or symmetry-protected Dirac nodes in the noninteracting limit, depending on microscopic parameters. By systematically incorporating extended density–density interactions within Hartree–Fock framework, we demonstrate how electronic correlations spontaneously generate topological

order in an otherwise semimetallic system.

Our central results are threefold. First, we show that interactions stabilize a quantum anomalous Hall (QAH) phase characterized by spontaneous time-reversal symmetry breaking and a nonzero Chern number. Second, we identify a robust bond-nematic Dirac semimetal (BNDS) phase that intervenes between topological and trivial insulating states, revealing a nontrivial interplay between nematicity and topology. Third, we demonstrate how lattice asymmetry and staggered potentials control the competition between these phases, allowing a continuous evolution from QBT-driven to Dirac-driven topological behavior.

3.1 Generalized two-dimensional SSH model

We consider a two-dimensional interacting spinless fermion model defined on a square lattice with a four-site unit cell. The lattice geometry [Fig. 3.1] can be viewed as a natural two-dimensional generalization of the Su–Schrieffer–Heeger (SSH) [86, 87, 88] model, where dimerized hopping patterns are introduced along both spatial directions. Each unit cell consists of four inequivalent sublattice sites, labeled a, b, c, and d, arranged in a plaquette geometry.

The Hamiltonian of the model is given by

$$\hat{H} = -\sum_{i,j}\Big(t_{ij}\, c_i^\dagger c_j + \text{h.c.}\Big) + \delta \sum_{i\in\{a,d\}} n_i - \delta \sum_{i\in\{b,c\}} n_i + U\sum_{\langle i,j\rangle} n_i n_j + V \sum_{\langle\langle i,j\rangle\rangle} n_i n_j. \quad (3.1)$$

Here, $c_i^\dagger$ (c_i) creates (annihilates) a spinless fermion at lattice site i, and $n_i = c_i^\dagger c_i$ is the local density operator. The hopping amplitudes t_{ij} include inequivalent nearest-neighbor (NN) hoppings t_1 and t_2, corresponding respectively to intra-cell and inter-cell bonds. In addition, next-nearest-neighbor (NNN) hoppings are included with amplitudes t_1' and t_2', which connect sites along the diagonals of each plaquette.

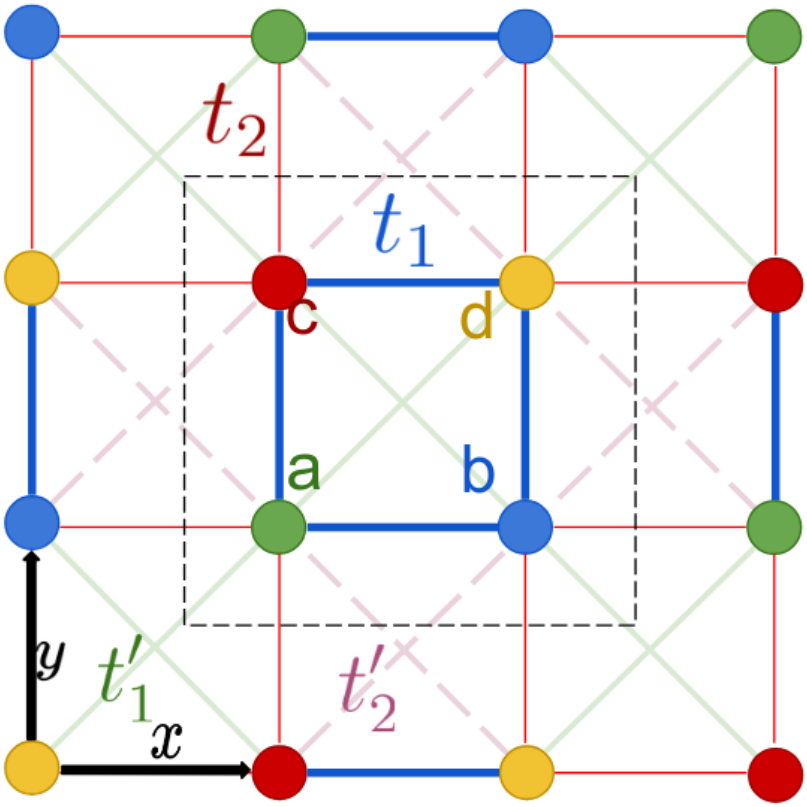

Figure 3.1: Schematic of the two-dimensional Su–Schrieffer–Heeger (SSH) model on a square lattice with four sites per unit cell (plaquette). Nearest-neighbor (NN) hoppings include intra-cell bonds (blue, amplitude t_1) and inter-cell bonds (red, amplitude t_2). Next-nearest-neighbor (NNN) hoppings introduce diagonal couplings: green and purple bonds denote amplitudes t'_1 and t'_2, respectively.

The second and third terms in Eq. (3.1) represent a staggered on-site potential δ, which assigns an energy $+\delta$ to sublattice sites a and d and $-\delta$ to sites b and c. This term explicitly breaks sublattice and rotational symmetries and plays a crucial role in tuning the low-energy band structure. The last two terms describe repulsive density–density interactions: U acts between NN sites $\langle i, j\rangle$, while V couples NNN pairs $\langle\langle i, j\rangle\rangle$.

Depending on the hopping parameters, the model interpolates between different lattice geometries. For $t_1 = t_2$, the system reduces to a checkerboard lattice with uniform NN hopping. When the NNN hoppings satisfy $t'_1 = -t'_2 = 0.5$ (these values are fixed throughout the remainder of this chapter unless otherwise stated), the model preserves particle-hole

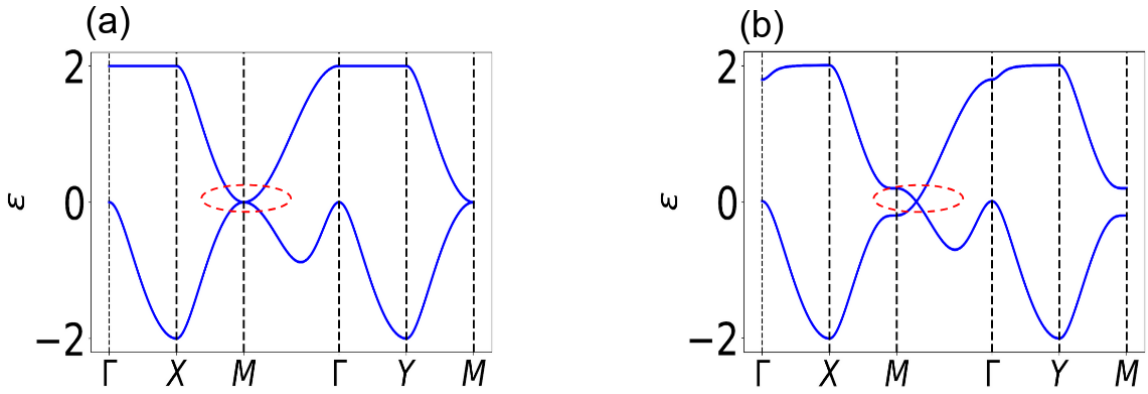

Figure 3.2: **(a)** Noninteracting band structure at $\delta = 0$, showing a quadratic band touching (QBT) at the Brillouin-zone M point (π, π). **(b)** Band structure at $\delta = -0.2t_1$ with $t_1 = 1.0$ and $t_2 = 2.0$, where the QBT splits into two Dirac cones. The high-symmetry points are $\Gamma = (\frac{\pi}{2}, \frac{\pi}{2})$, $X = (\pi, \frac{\pi}{2})$, $Y = (\frac{\pi}{2}, \pi)$, and $M = (\pi, \pi)$.

symmetry [see Appendix. A.2], and the noninteracting band structure exhibits a QBT at the high symmetry $M(\pi, \pi)$ point. A finite staggered potential δ breaks the fourfold (C_4) rotational symmetry and splits the QBT into two Dirac cones [89]. Depending on the sign of δ, the cones appear along one of two orthogonal directions in the Brillouin zone: either the $k_y - k_x = 0$ line or the $k_y + k_x = \frac{3\pi}{2}$ line. In contrast, setting $t_1 \neq t_2$ breaks particle–hole symmetry but preserves the QBT at M when $\delta = 0$ [Fig. 3.2(a)]. For finite δ, this QBT also splits into a pair of Dirac cones [Fig. 3.2(b)], similar the checkerboard case [89]. The QBT is protected by the C_4 rotational symmetry of the lattice, which forbids linear Dirac terms in the effective low-energy Hamiltonian [39, 40]. Breaking C_4 symmetry lifts this protection, splitting the QBT into Dirac cones and strongly modifying the susceptibility to interaction-driven instabilities [46, 89]. Throughout this chapter, we focus on the half-filled case, where the interplay between band degeneracies, lattice symmetries, and electronic interactions is most pronounced.

3.2 Hartree–Fock formulation and momentum-space Hamiltonian

To investigate interaction-driven instabilities in the generalized two-dimensional SSH model, we employ an Hartree–Fock (HF) mean-field approximation with a four-site unit-cell ansatz. This approach allows for the spontaneous breaking of time-reversal, translational, and point-group symmetries, and is therefore well suited for describing charge-ordered, nematic, and interaction-induced topological phases on equal footing.

The density–density interaction terms in Eq. (3.1) are decoupled by retaining both Hartree (density) and Fock (exchange) channels. Within this approximation, the mean-field decomposition for a generic interacting bond between sites i and j is given by

$$\hat{n}_i\hat{n}_j \simeq \langle\hat{n}_i\rangle\hat{n}_j + \langle\hat{n}_j\rangle\hat{n}_i - \langle\hat{n}_i\rangle\langle\hat{n}_j\rangle - \epsilon_{ji}\hat{c}_i^\dagger\hat{c}_j - \epsilon_{ij}\hat{c}_j^\dagger\hat{c}_i + |\epsilon_{ij}|^2,$$

where $\epsilon_{ij} = \langle\hat{c}_i^\dagger\hat{c}_j\rangle$ denotes the bond expectation value arising from the exchange channel.

The bond expectation values are decomposed into real and imaginary parts as $\epsilon_{ij} = \epsilon_{ij}^R + i\epsilon_{ij}^I$. The imaginary components correspond to circulating bond currents and allow for spontaneous breaking of time-reversal symmetry. To capture such loop-current order associated with imaginary nearest-neighbor hopping processes, we impose the constraints

$$\begin{aligned}
\langle\hat{c}_b^\dagger\hat{c}_a\rangle &= \langle\hat{c}_b^\dagger\hat{c}_{a+2\hat{x}}\rangle, \qquad \langle\hat{c}_c^\dagger\hat{c}_a\rangle = \langle\hat{c}_c^\dagger\hat{c}_{a+2\hat{y}}\rangle, \\
\langle\hat{c}_d^\dagger\hat{c}_c\rangle &= \langle\hat{c}_d^\dagger\hat{c}_{c+2\hat{x}}\rangle, \qquad \langle\hat{c}_d^\dagger\hat{c}_b\rangle = \langle\hat{c}_d^\dagger\hat{c}_{b+2\hat{y}}\rangle,
\end{aligned} \tag{3.2}$$

together with their Hermitian conjugates. All next-nearest-neighbor (NNN) mean-field parameters are constrained to be real.

With these assumptions, the Hartree–Fock Hamiltonian can be written in momentum space as

$$\hat{H} = E_0 + \sum_{\mathbf{k}} \Psi_{\mathbf{k}}^\dagger \, \mathcal{H}_{\mathrm{HF}}^{\mathbf{k}} \, \Psi_{\mathbf{k}}, \tag{3.3}$$

where

$$\Psi_{\mathbf{k}} = \begin{pmatrix} \hat{c}_{\mathbf{k},a} \\ \hat{c}_{\mathbf{k},b} \\ \hat{c}_{\mathbf{k},c} \\ \hat{c}_{\mathbf{k},d} \end{pmatrix}. \tag{3.4}$$

The Hartree–Fock Hamiltonian matrix takes the general form

$$\mathcal{H}^{\mathbf{k}}_{\mathrm{HF}} = \begin{pmatrix} \mathcal{H}^{\mathbf{k}}_{00} & \mathcal{H}^{\mathbf{k}}_{01} & \mathcal{H}^{\mathbf{k}}_{02} & \mathcal{H}^{\mathbf{k}}_{03} \\ \mathcal{H}^{\mathbf{k}}_{01*} & \mathcal{H}^{\mathbf{k}}_{11} & \mathcal{H}^{\mathbf{k}}_{12} & \mathcal{H}^{\mathbf{k}}_{13} \\ \mathcal{H}^{\mathbf{k}}_{02*} & \mathcal{H}^{\mathbf{k}}_{12*} & H^{\mathbf{k}}_{22} & \mathcal{H}^{\mathbf{k}}_{23} \\ \mathcal{H}^{\mathbf{k}}_{03*} & \mathcal{H}^{\mathbf{k}}_{13*} & \mathcal{H}^{\mathbf{k}}_{23*} & \mathcal{H}^{\mathbf{k}}_{33} \end{pmatrix}, \tag{3.5}$$

where the diagonal elements arise from Hartree contributions, while the off-diagonal elements contain both bare hopping terms and Fock-induced renormalizations.

The diagonal matrix elements are given by

$$\mathcal{H}^{\mathbf{k}}_{00} = 2U(\bar{n}_b + \bar{n}_c) + 4V\bar{n}_d + \delta, \tag{3.6}$$

$$\mathcal{H}^{\mathbf{k}}_{11} = 2U(\bar{n}_a + \bar{n}_d) + 4V\bar{n}_c - \delta, \tag{3.7}$$

$$\mathcal{H}^{\mathbf{k}}_{22} = 2U(\bar{n}_a + \bar{n}_d) + 4V\bar{n}_b - \delta, \tag{3.8}$$

$$\mathcal{H}^{\mathbf{k}}_{33} = 2U(\bar{n}_b + \bar{n}_c) + 4V\bar{n}_a + \delta. \tag{3.9}$$

The off-diagonal elements read

$$\mathcal{H}^{\mathbf{k}}_{01} = -t_1 e^{-ik_x} - t_2 e^{ik_x} - 2U\epsilon^R_{ab}\cos k_x - 2iV\epsilon^I_{ab}\cos k_x, \tag{3.10}$$

$$\mathcal{H}^{\mathbf{k}}_{02} = -t_1 e^{-ik_y} - t_2 e^{ik_y} - 2U\epsilon^R_{ac}\cos k_y - 2iV\epsilon^I_{ac}\cos k_y, \tag{3.11}$$

$$\mathcal{H}^{\mathbf{k}}_{13} = -t_1 e^{-ik_y} - t_2 e^{ik_y} - 2U\epsilon^R_{bd}\cos k_y - 2iV\epsilon^I_{bd}\cos k_y, \tag{3.12}$$

$$\mathcal{H}^{\mathbf{k}}_{23} = -t_1 e^{-ik_x} - t_2 e^{ik_x} - 2U\epsilon^R_{cd}\cos k_x - 2iV\epsilon^I_{cd}\cos k_x, \tag{3.13}$$

$$\mathcal{H}^{\mathbf{k}}_{03} = 2\big(t'_1 - V\epsilon^1_{ad}\big)\cos(k_x + k_y) + 2\big(t'_2 - V\epsilon^2_{ad}\big)\cos(k_x - k_y), \tag{3.14}$$

$$\mathcal{H}^{\mathbf{k}}_{12} = 2\big(t'_2 - V\epsilon^1_{bc}\big)\cos(k_x + k_y) + 2\big(t'_1 - V\epsilon^2_{bc}\big)\cos(k_x - k_y). \tag{3.15}$$

All remaining matrix elements follow from Hermiticity.

Finally, the constant energy shift is given by

$$E_0 = 2U\big(|\epsilon_{ab}|^2 + |\epsilon_{cd}|^2 + |\epsilon_{bd}|^2 + |\epsilon_{ac}|^2 - (\bar{n}_a + \bar{n}_d)(\bar{n}_b + \bar{n}_c)\big) + 2V\big(|\epsilon^1_{ad}|^2 + |\epsilon^2_{ad}|^2 + |\epsilon^1_{bc}|^2 + |\epsilon^2_{bc}|^2 - 2(\bar{n}_a\bar{n}_d + \bar{n}_b\bar{n}_c)\big)\,. \tag{3.16}$$

The self-consistent Hartree–Fock equations are solved by diagonalizing $\mathcal{H}^{\mathbf{k}}_{\mathrm{HF}}$ at each momentum $\mathbf{k}$, updating the mean-field parameters $\bar{n}_i$ and ϵ_{ij}, and iterating until the total energy converges within a tolerance of 10^{-10}.

3.3 Order parameters and symmetry classification

The Hartree–Fock formulation introduced in the previous section allows for a variety of competing ordered phases, distinguished by the symmetry properties of the self-consistent mean-field parameters. In this section, we define the order parameters used to characterize the interaction-driven phases of the generalized two-dimensional SSH model and classify them according to the symmetries they break.

Throughout this section, the order parameters are constructed from the site-resolved densities $\bar{n}_i = \langle \hat{n}_i \rangle$ and the bond expectation values $\epsilon_{ij} = \langle \hat{c}^\dagger_i \hat{c}_j \rangle$ appearing in the Hartree–Fock Hamiltonian.

3.3.1 Quantum anomalous Hall order

The quantum anomalous Hall (QAH) phase is characterized by spontaneous breaking of time-reversal symmetry and the emergence of circulating loop currents. Within the Hartree–Fock framework, this phase is signaled by purely imaginary nearest-neighbor bond expectation values.

A convenient order parameter for the QAH phase is defined as

$$\epsilon_{\mathrm{QAH}} = \frac{1}{4}\left|\mathrm{Im}\left(\epsilon_{ab} + \epsilon_{bd} + \epsilon_{dc} + \epsilon_{ca}\right)\right|, \tag{3.17}$$

which measures the net circulating current around a plaquette. A nonzero value of ϵ_{QAH} indicates spontaneous time-reversal symmetry breaking and corresponds to a gapped topological phase with a nonzero Chern number.

3.3.2 Site-nematic insulating order

The site-nematic insulating (SNI) phase is characterized by an imbalance in the local charge densities between different sublattices, leading to the breaking of the fourfold rotational (C_4) symmetry.

The corresponding order parameter is defined as

$$\delta_{\mathrm{SNI}} = \left|(\bar{n}_a + \bar{n}_d) - (\bar{n}_b + \bar{n}_c)\right|. \tag{3.18}$$

A finite value of δ_{SNI} indicates the formation of a gapped nematic insulating phase with inequivalent charge occupation on the two sublattice pairs.

3.3.3 Stripe charge-density-wave order

The stripe charge-density-wave (CDW) phase breaks translational symmetry and is characterized by alternating charge densities across different lattice sites. This phase is captured by the order parameter

$$\delta_{\mathrm{CDW}} = |\bar{n}_a - \bar{n}_d| + |\bar{n}_b - \bar{n}_c|. \tag{3.19}$$

A nonzero value of δ_{CDW} signals the formation of a stripe-like charge modulation and is accompanied by a gap opening in the single-particle spectrum.

3.3.4 Bond-nematic order

The bond-nematic Dirac semimetal (BNDS) is a gapless phase that spontaneously breaks the fourfold (C_4) rotational symmetry due to anisotropic next-nearest-neighbor (NNN) bond ordering. This nematicity manifests as an imbalance in the electronic bond strengths along orthogonal diagonal directions.

Specifically, for the a and d sublattices, the bond anisotropy is quantified by

$$\Delta_{\text{bond}}^{(1)} = \left| \langle \hat{c}_{a+\hat{x}+\hat{y}}^{\dagger} \hat{c}_a \rangle - \langle \hat{c}_{a+\hat{x}-\hat{y}}^{\dagger} \hat{c}_a \rangle \right|, \tag{3.20}$$

which measures the difference between NNN correlations along the two diagonal directions.

Similarly, the corresponding anisotropy for the b and c sublattices is given by

$$\Delta_{\text{bond}}^{(2)} = \left| \langle \hat{c}_{b+\hat{x}+\hat{y}}^{\dagger} \hat{c}_b \rangle - \langle \hat{c}_{b+\hat{x}-\hat{y}}^{\dagger} \hat{c}_b \rangle \right|. \tag{3.21}$$

The overall bond-nematic order parameter is then defined as the sublattice-resolved difference between these anisotropies,

$$\Delta_{\text{bond}} = \left| \Delta_{\text{bond}}^{(1)} - \Delta_{\text{bond}}^{(2)} \right|, \tag{3.22}$$

which captures the spontaneous breaking of C_4 rotational symmetry while maintaining translational invariance.

3.3.5 Summary of symmetry breaking patterns

The interaction-driven phases discussed above can be classified according to their symmetry properties as follows. The QAH phase breaks time-reversal symmetry while preserving translational symmetry. The SNI and stripe CDW phases break rotational symmetry and open a charge gap. In contrast, the BNDS phase breaks rotational symmetry without opening a gap. The competition and coexistence of these orders lead to the rich phase diagrams presented in the following section.

3.4 Interaction-driven phase diagrams and physical discussion

We have established the model, mean-field formulation, and order parameters in the preceding sections. We now discuss the interaction-driven phase diagrams of the generalized two-

dimensional SSH model, focusing on how the underlying band structure controls the competition between topological and symmetry-breaking orders. We begin with the quadratic band touching (QBT) regime, which provides a unifying framework for understanding the dominant interaction-driven instabilities. Within this regime, we first analyze the symmetric checkerboard limit and then examine the effects of hopping asymmetry, which preserves the QBT while explicitly favoring nematic bond ordering. Finally, we discuss the Dirac semimetal regime induced by a staggered on-site potential, where the lifting of the QBT qualitatively alters the phase diagram.

3.4.1 Phase diagram in the quadratic band touching regime: checkerboard limit

We begin the discussion of interaction-driven phases in the quadratic band touching (QBT) regime by considering the checkerboard limit of the generalized two-dimensional SSH model, corresponding to equal intra- and inter-cell hopping amplitudes $t_1 = t_2 = 1.0$ and vanishing staggered potential $\delta = 0$. In this limit, the lattice preserves fourfold rotational (C_4) symmetry, and the noninteracting band structure at half filling hosts a symmetry-protected quadratic band touching point. This QBT provides the natural starting point for understanding the interaction-driven instabilities discussed in this chapter.

The presence of a quadratic band touching (QBT) plays a central role in shaping the interaction driven phase diagram of the model. Unlike Dirac points, where the density of states vanishes linearly at the Fermi level, a QBT supports a finite density of states, making the semimetallic state unstable even to weak repulsive interactions. Within the Hartree–Fock framework, this enhanced susceptibility gives rise to multiple competing ordered phases at moderate interaction strengths. As shown in Fig. 3.3(a) for the symmetric checkerboard limit, the zero temperature phase diagram hosts a quantum anomalous Hall (QAH) insulator with Chern number $C = \pm 1$ [90], a bond nematic Dirac semimetal (BNDS), a

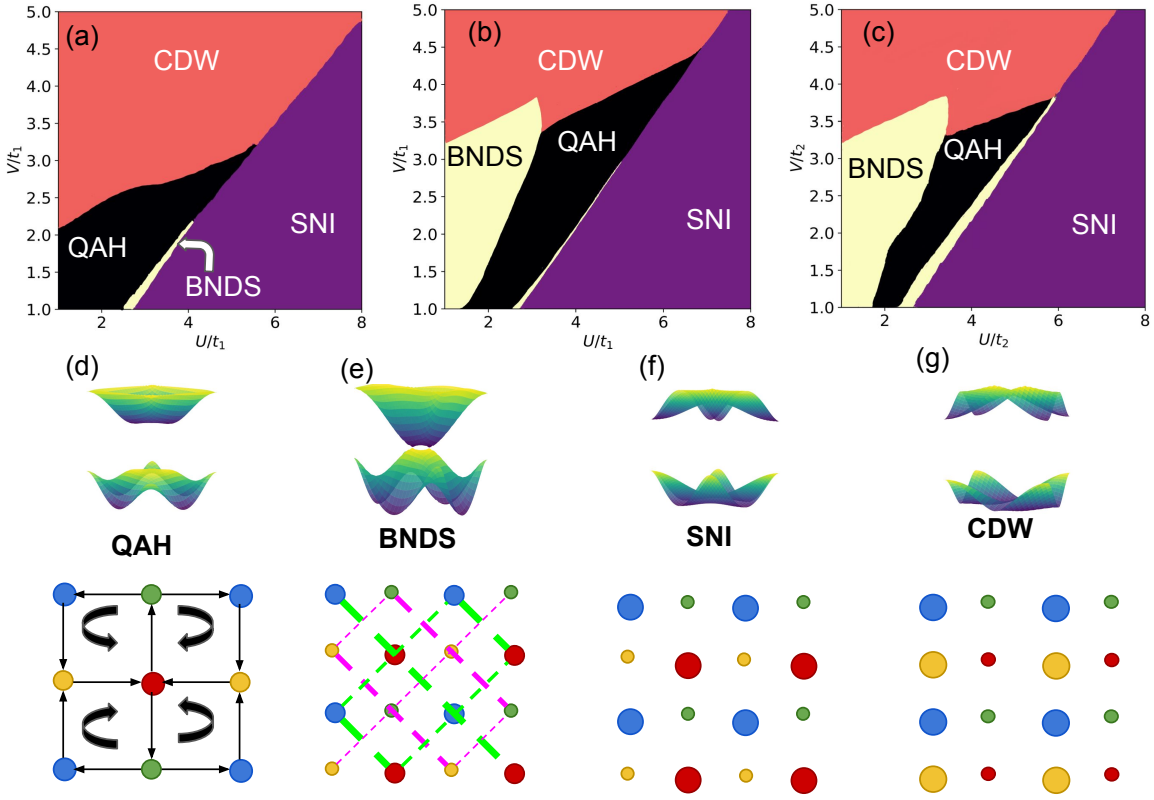

Figure 3.3: **Interaction-driven phase diagrams of the generalized 2D SSH model at $\delta = 0$ for different hopping configurations. (a)** Phase diagram for the symmetric hopping case $t_1 = t_2 = 1.0$, corresponding to the checkerboard limit. Four distinct phases emerge: a QAH phase with spontaneous time-reversal symmetry breaking (black), a SNI that breaks C_4 symmetry (purple), a stripe CDW (red), and a BNDS with gapless anisotropic Dirac nodes (yellow). **(b)** Phase diagram for asymmetric hopping with $t_1 = 1.0$ and $t_2 = 2.0$, representative of the generalized SSH regime. The QAH phase remains robust, while the BNDS region expands significantly due to enhanced bond anisotropy. The site-nematic and stripe-ordered insulating phases persist but shrink in extent. **(c)** Phase diagram for another asymmetric case, $t_1 = 2.0$ and $t_2 = 1.0$. While the overall structure is similar to (b), the QAH region is reduced, reflecting the sensitivity of topological ordering to the direction of hopping asymmetry. The BNDS and insulating phases continue to dominate, underscoring their robustness. **(d-g)** Representative band spectra and ordering patterns of spinless fermions at half-filling in the topologically trivial SSH lattice with a QBT point, shown for asymmetric hopping parameters $t_1 = 1.0$ and $t_2 = 2.0$. The QAH phase is distinguished by loop-current order, while the BNDS phase features anisotropic bond ordering. SNI and stripe CDW phases are also illustrated with their characteristic charge distributions. Circle sizes indicate the local charge density, and bond widths represent the magnitude of the bond-order parameter.

site nematic insulator (SNI), and a stripe charge density wave (CDW) phase. These phases originate from distinct symmetry breaking mechanisms, including time-reversal, rotational, and translational symmetry breaking, and are characterized by the order parameters defined in Sec. 3.3.

At weak to intermediate U, the dominant instability is toward the QAH phase. The finite DOS at the QBT lowers the energy cost of opening a topological gap through complex nearest-neighbor bond order, stabilizing spontaneous time-reversal breaking. Upon increasing the interaction strength, the QAH phase gives way to competing ordered states. In particular, we observe the emergence of a bond-nematic Dirac semimetal (BNDS), which intervenes between the QAH phase and the site-nematic insulating phase. The BNDS phase is characterized by anisotropic bond expectation $\Delta^{(1)}_{\text{bond}}$ values that break the C_4 rotational symmetry while preserving translational and time-reversal symmetries. Remarkably, despite the presence of strong interactions, the single-particle spectrum remains gapless in this phase, retaining Dirac nodes with anisotropic velocities.

The appearance of an intermediate BNDS phase separating the QAH and SNI phases has not been reported in earlier mean-field studies [90, 91] of closely related lattice models. This finding is consistent with recent thermodynamic studies [92, 93], which identified BNDS as a finite-temperature stable phase with characteristic bond-order signatures. In many previous Hartree–Fock analyses, bond order sector was not analysed and attention was focused primarily on insulating phases, such as charge-ordered or topological states. As a consequence, the possibility of an intermediate, gapless nematic phase between the QAH and SNI phases was overlooked. At still stronger interactions, charge-ordered insulating phases dominate: the SNI via sublattice occupation imbalance and the stripe CDW via periodic density modulation. These emerge as Hartree-driven density terms become energetically favorable.

Overall, the phase diagram in the checkerboard limit highlights the strong competi-

tion between topological order, nematic bond order, and charge ordering in systems with quadratic band touching. This regime therefore provides a useful reference point for understanding how additional symmetry breaking, such as hopping asymmetry, modifies the phase diagram, as discussed in the following subsection.

3.4.2 Phase diagram in the quadratic band touching regime with hopping asymmetry

We now consider the quadratic band touching (QBT) regime in the presence of hopping asymmetry, focusing on the two representative cases $t_1 = 1.0$, $t_2 = 2.0$ and $t_1 = 2.0$, $t_2 = 1.0$, with the staggered potential fixed to $\delta = 0$. In both cases, the quadratic band touching at half filling remains intact and protected by lattice symmetries, allowing us to examine how modifying the relative strength of intra- and inter-cell hopping influences interaction-driven ordering tendencies within the QBT regime.

We first discuss the case $t_1 = 1.0$ and $t_2 = 2.0$ [Fig. 3.3 (b)]. Introducing hopping asymmetry has a pronounced impact on the balance between competing phases. Compared to the symmetric checkerboard limit, nematic ordering in the bond sector is strongly enhanced, leading to a significant expansion of the bond-nematic Dirac semimetal (BNDS) phase. This phase becomes stable already at relatively weak interaction strengths. Physically, the imbalance between intra- and inter-cell hopping amplitudes favors anisotropic bond correlations, making it energetically favorable for the system to develop nematic bond order while remaining gapless.

In the asymmetric hopping regime, the quantum anomalous Hall (QAH) phase characterized by a Chern number $C = \pm 1$ [see Appendix A.1] remains present at weak to intermediate interaction strengths, although its region in the phase diagram is reduced compared to the symmetric checkerboard limit. At larger interaction strengths, insulating phases driven by charge ordering reappear. The SNI phase is stabilized by sublattice density imbalance,

while the stripe CDW phase emerges when translational symmetry breaking further lowers the interaction energy. The corresponding band structures and representative bond- and charge-order patterns are shown in Fig. 3.3(d)–3.3(g).

We now turn to the complementary asymmetric case $t_1 = 2.0$ and $t_2 = 1.0$ [Fig. 3.3 (c)]. The resulting phase diagram exhibits the same qualitative features as the $t_1 = 1.0$, $t_2 = 2.0$ case. The enhancement of the BNDS phase, the suppression of the QAH phase, and the appearance of charge-ordered insulating phases at stronger interactions all persist. The two phase diagrams are related by an interchange of bond directions, and no additional phases are introduced. Overall, the BNDS phase remains prevalent across all three hopping regimes, indicating its generic presence in the phase diagram of generalized SSH models with extended interactions. Our results not only extend previous Hartree-Fock analyses [90, 91] but also establish a clear link between bond anisotropy and the stabilization of gapless nematic phases. The clear identification of the BNDS region in our self-consistent solution highlights the critical role of competing bond-order channels in shaping the phase diagram of semimetallic systems with interaction-driven instabilities

3.4.3 Competition of order parameters in the quadratic band touching regime

A more detailed understanding of the interaction-driven phases in the quadratic band touching (QBT) regime can be obtained by examining the evolution of the relevant order parameters as a function of interaction strength, as shown in Fig. 3.4. Rather than focusing solely on phase boundaries, this analysis highlights how different ordering tendencies compete and, in some cases, coexist as interactions increase.

We begin with the weak-coupling regime, where the system stabilizes a bond-nematic Dirac semimetal (BNDS). As shown in Fig. 3.4(a), for asymmetric hopping $t_1 = 1.0$ and $t_2 = 2.0$, the bond-nematic order parameter becomes finite already at small values of the

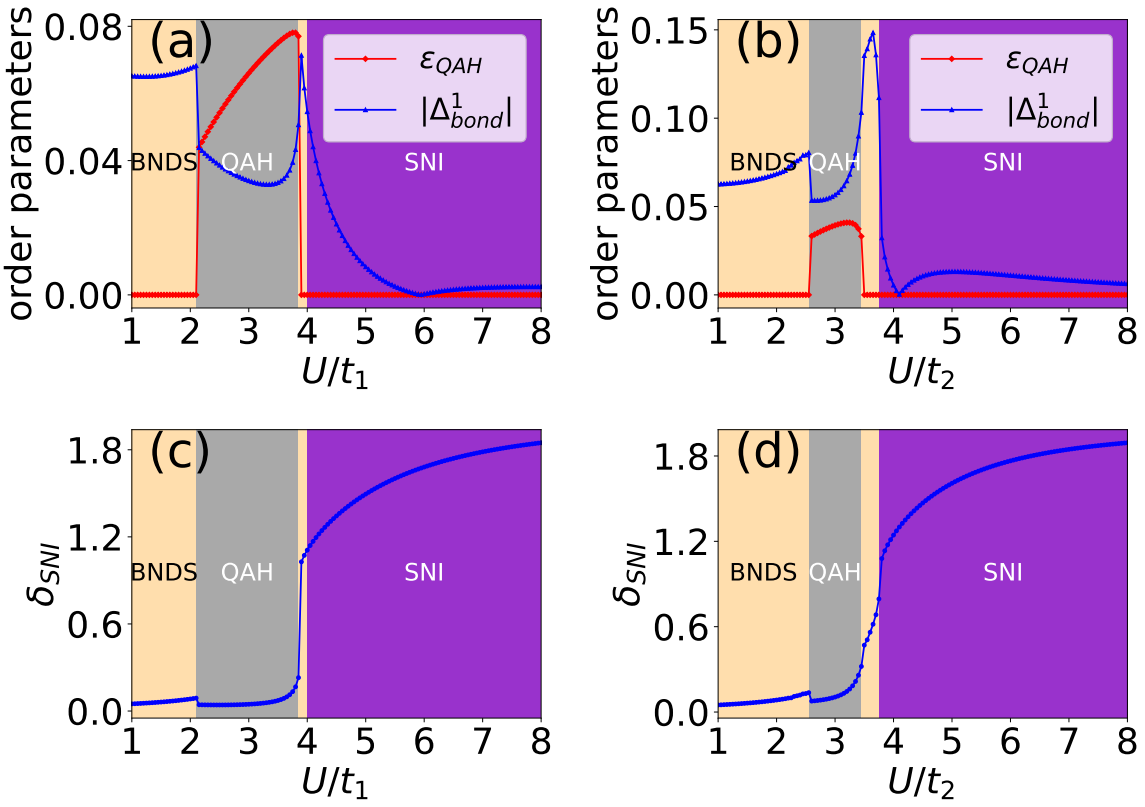

Figure 3.4: **(a)** Evolution of the QAH and BNDS order parameters as functions of the interaction strength U for fixed hopping amplitudes $t_1 = 1.0$, $t_2 = 2.0$, and onsite potential $\delta = 0$. At weak coupling, the system exhibits a pure BNDS phase characterized by spontaneous bond-nematic order. In the intermediate U regime, both QAH and BNDS order parameters coexist, indicating an interaction-induced topological-nematic mixed phase. As U increases further, the QAH order is suppressed, and a narrow BNDS region emerges before the transition to a SNI phase. **(b)** Corresponding plot for $t_1 = 2.0$, $t_2 = 1.0$, showing a reduced extent of the QAH phase and a slightly broader BNDS region separating the QAH and SNI phases. All the data in (a) and (b) are in arbitrary unit. **(c)** Site-nematic order parameter δ_{site} as a function of U for $t_1 = 1.0$, $t_2 = 2.0$. The SNI order parameter remains finite across all phases, including the BNDS and QAH regimes, but becomes strongly enhanced deep in the SNI phase, signaling a crossover from weak to strong site-nematic order. **(d)** Similar behavior of δ_{site} for $t_1 = 2.0$, $t_2 = 1.0$, consistent with the trends observed in panel (c), confirming the robustness of site-nematic fluctuations across the phase diagram. All plots are obtained for fixed next nearest-neighbor interaction strength $V = 2.0t_1$ in panels (a) and (c), and $V = 2.0t_2$ in panels (b) and (d).

interaction strength, while the QAH order parameter remains strictly zero. This indicates spontaneous breaking of rotational symmetry without breaking time-reversal symmetry. Microscopically, interactions induce anisotropic bond correlations that split the quadratic band touching into a pair of Dirac nodes, resulting in a gapless but nematically distorted semimetal.

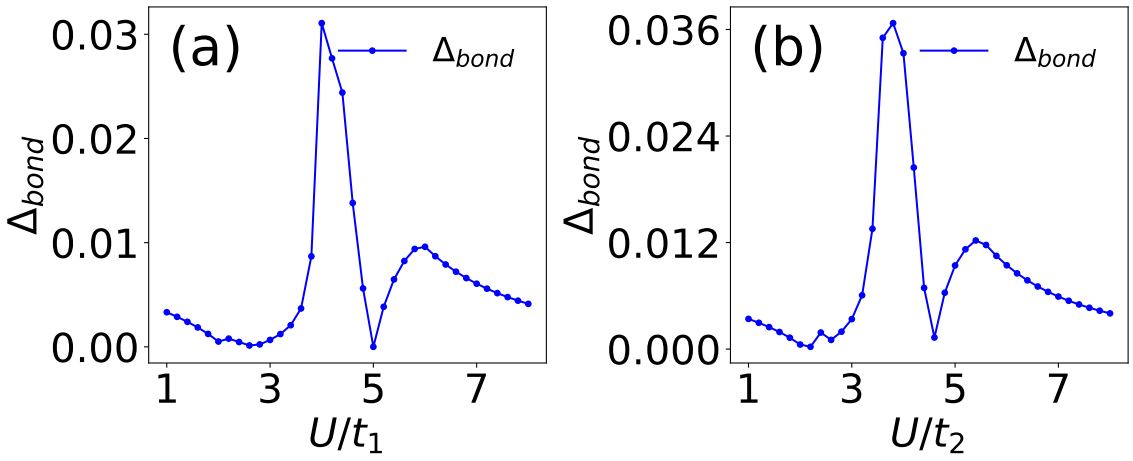

Figure 3.5: Interaction dependence of the sublattice-dependent bond order. **(a)** $t_1 = 1.0, t_2 = 2.0$ and **(b)** $t_1 = 2.0, t_2 = 1.0$, both exhibiting a finite value that signals sublattice-selective bond order driving anisotropic BNDS formation. For comparison, the symmetric checkerboard limit $(t_1 = t_2 = 1.0)$ yields zero difference, confirming the absence of sublattice dependence.

Importantly, the bond-nematic order realized in the presence of hopping asymmetry is sublattice dependent. As shown in Fig. 3.5, the interaction-induced bond order between the a and d sublattice sites differs slightly from that between the c and b sites. This sublattice-selective anisotropy Δ_{bond} is a direct consequence of hopping asymmetry in the generalized SSH model and is absent in the symmetric checkerboard limit ($t_1 = t_2$), where the corresponding difference vanishes. The BNDS phase identified here therefore represents a qualitatively distinct form of nematic semimetallicity, characterized by both directional and sublattice-resolved bond modulation.

Upon increasing the interaction strength, the system enters an intermediate regime where

bond-nematic and topological orders coexist. In this regime, both the BNDS and QAH order parameters acquire finite values simultaneously, as evidenced by the overlap of the corresponding curves in Fig. 3.4(a). This coexistence reflects a phase in which time-reversal symmetry is broken through loop-current formation, while rotational symmetry remains broken due to nematic bond anisotropy. Importantly, the growth of the QAH order parameter is accompanied by a partial suppression of the bond-nematic order, signaling direct competition between these two ordering tendencies. The QAH order opens a topological gap at the QBT, while the nematic bond order preserves anisotropy in the electronic structure. This regime demonstrates that interaction-driven topological order does not emerge in isolation, but develops on top of an already nematically distorted background.

At larger U, the QAH order parameter is suppressed and the system crosses over into a site-nematic insulating (SNI) phase. This transition is signaled by a sharp increase in the site-nematic order parameter, as shown in Fig. 3.4(c). While the site-nematic order parameter remains finite even in the BNDS and QAH regimes, it is subdominant there and becomes strongly enhanced only at strong coupling. This behavior reflects a gradual crossover from weak nematic fluctuations to a fully developed site-nematic insulating state driven primarily by Hartree (density) terms. In this regime, bond-driven orders are suppressed, the system becomes fully gapped, and charge localization dominates the low-energy physics.

A comparison with the inverted hopping configuration $t_1 = 2.0$ and $t_2 = 1.0$, shown in Fig. 3.4(b) and Fig. 3.4(d), reveals the same qualitative sequence of regimes. However, the extent of the QAH phase is reduced, while the intermediate BNDS region separating the QAH and SNI phases becomes broader. This asymmetry reflects the sensitivity of loop-current-driven topological order to the hopping hierarchy, whereas nematic bond order remains comparatively robust. Notably, the site-nematic order parameter exhibits similar qualitative behavior in both hopping configurations, remaining finite across all interaction strengths and sharply increasing only in the strong-coupling regime.

Taken together, Fig. 3.4 reveals a clear hierarchy of interaction-driven instabilities in the QBT regime. Nematic bond order dominates at weak coupling, a mixed topological–nematic phase emerges at intermediate coupling, and site-nematic insulating order prevails at strong coupling. The analysis of order parameters thus demonstrates that interaction-driven topological order in this model is closely intertwined with nematicity and competes directly with both bond- and density-driven symmetry breaking.

3.4.4 Phase diagram in the Dirac semimetal regime

We now turn to the Dirac semimetal regime, which is realized by introducing a finite staggered on-site potential δ. This term explicitly breaks sublattice symmetry and lifts the quadratic band touching, splitting it into a pair of Dirac cones. As a consequence, the low-energy density of states at the Fermi level is reduced compared to the QBT regime. This qualitative change in the band structure plays a crucial role in reshaping the balance between competing interaction-driven orders.

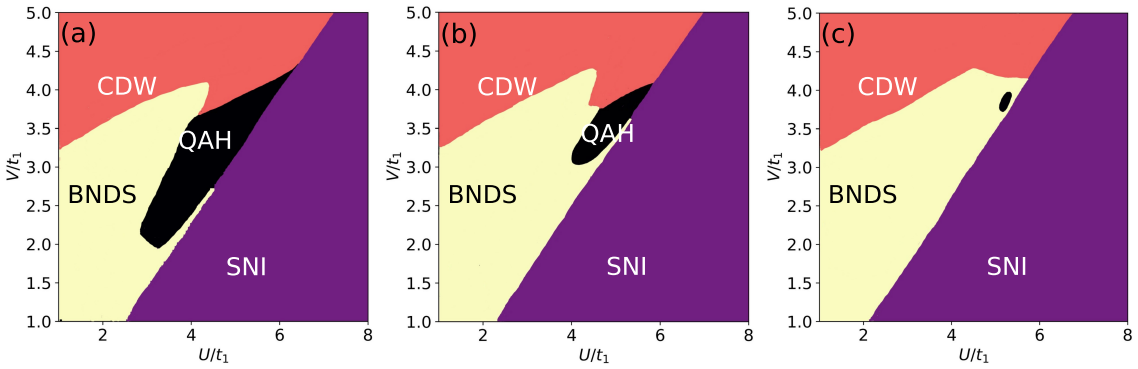

Figure 3.6: **Interaction-driven phase diagrams in the Dirac semimetal regime with** $t_1 = 1.0$ **and** $t_2 = 2.0$ **for varying staggered potential** δ**. (a)** For $\delta = 0.2t_1$, a finite staggered potential already reduces the extent of the QAH phase (black) compared to the $\delta = 0$ case. **(b)** At $\delta = 0.4t_1$, the QAH region is further suppressed. **(c)** For $\delta = 0.6t_1$, the QAH phase is nearly absent, giving way to the BNDS phase. Across all cases, increasing δ destabilizes the interaction-induced QAH state in favor of BNDS, indicating that the QAH phase remains robust only for weak sublattice staggering.

Figure 3.6 summarizes the evolution of the interaction-driven phase diagram with increasing δ for fixed hopping parameters $t_1 = 1.0$ and $t_2 = 2.0$. For a small staggered potential, $\delta = 0.2t_1$ [Fig. 3.6(a)], the quantum anomalous Hall (QAH) phase remains clearly visible and occupies a sizable region of the interaction parameter space. The QAH phase is characterized by a nonzero Chern number $C = \pm 1$, indicating that interaction-driven topological order can survive the explicit breaking of sublattice symmetry, provided that the staggered potential is sufficiently weak. Nevertheless, even at this small value of δ, the extent of the QAH phase is already reduced compared to the QBT case $\delta = 0$ [Fig. 3.3(b)], reflecting the reduced effectiveness of interactions in the presence of Dirac dispersions.

As the staggered potential is increased to $\delta = 0.4t_1$ [Fig. 3.6(b)], the competition between explicit symmetry breaking and interaction-driven ordering becomes more pronounced. The QAH phase is significantly suppressed, while the bond-nematic Dirac semimetal (BNDS) phase expands and occupies a larger portion of the phase diagram. This behavior indicates that once the quadratic band touching is lifted, nematic bond ordering provides a more efficient route for relieving interaction-induced instabilities than the formation of loop-current order associated with the QAH phase.

For a larger staggered potential, $\delta = 0.6t_1$ [Fig. 3.6(c)], the QAH phase is almost entirely eliminated. In this regime, the BNDS phase dominates the phase diagram over a wide range of interaction strengths. The near disappearance of the QAH phase highlights the fragility of interaction-induced topological order against explicit lattice symmetry-breaking perturbations. While interactions are able to overcome weak sublattice staggering and stabilize a topological phase at small δ, sufficiently large staggered potentials suppress the low-energy degeneracies required for spontaneous time-reversal symmetry breaking and instead enhance nematic ordering tendencies.

Overall, the phase diagrams in the Dirac semimetal regime demonstrate that interaction-driven QAH order is robust only in the vicinity of the QBT point. As the system is tuned

deeper into the Dirac regime by increasing δ, the balance shifts decisively toward symmetry-broken bond-ordered phases. This behavior underscores the central role of band geometry and low-energy density of states in enabling interaction-driven topological phases and provides a natural contrast to the ordering phenomena observed in the quadratic band touching regime discussed earlier.

3.5 Summary and conclusion

In this work, we have investigated the interplay between topology and nematicity in a generalized interacting two-dimensional SSH model, controlled by hopping asymmetry, sublattice potential, and interaction strength. Using a Hartree–Fock approach, we identified four competing many-body phases: a quantum anomalous Hall (QAH) insulator, a site-nematic insulator (SNI), a stripe charge-density-wave (CDW) insulator, and a bond-nematic Dirac semimetal (BNDS).

In the symmetric checkerboard limit, where the noninteracting band structure hosts a quadratic band touching, the phase diagram contains all four interaction-driven phases. In this regime, the BNDS phase emerges as a robust but narrow intermediate state separating the QAH and SNI phases, which was not analysed in earlier HF studies [90, 91]. Introducing hopping asymmetry significantly enlarges the parameter regime occupied by the BNDS phase, while simultaneously reducing the stability of the QAH phase. The analysis of order parameters reveals a clear hierarchy of interaction-driven instabilities: nematic bond order dominates at weak coupling, coexists with QAH order at intermediate coupling, and gives way to site-nematic insulating order at strong coupling. Throughout these regimes, site-nematic order remains finite, indicating that interaction-driven topological phases develop on an underlying nematic background.

We further find that in the presence of hopping asymmetry, the BNDS phase develops

a sublattice-dependent bond order that is absent in the symmetric checkerboard case. This additional structure highlights the sensitivity of nematic bond order to kinetic anisotropy. A finite staggered sublattice potential δ qualitatively alters the phase diagram by lifting the quadratic band touching and producing Dirac cones with a reduced low-energy density of states. As a result, the interaction-driven QAH phase becomes increasingly fragile and remains stable only within a narrow parameter window. In contrast, nematic phases—particularly the BNDS—dominate the phase diagram over a broad range of interaction strengths in the Dirac semimetal regime.

Taken together, these results demonstrate that the interaction-driven QAH phase in this model is not an isolated instability, but rather part of a broader landscape in which topological and nematic orders are intrinsically intertwined. This perspective is directly relevant for experimental platforms such as cold-atom optical lattices, moiré superlattices, and quantum simulation architectures, where hopping asymmetry and sublattice potentials can be tuned with high precision. Promising future directions include the dynamical control of nematic and topological orders using periodic driving or strain, as well as extensions beyond mean-field theory using methods such as exact diagonalization, density-matrix renormalization group, or functional renormalization group. These approaches will be essential for testing the robustness of the QAH and BNDS phases and for uncovering possible new forms of interaction-driven topological–nematic quantum matter.

Chapter 4

Spin-imbalance induced buried topological edge currents in MI–TI heterostructures

In the previous chapter, we demonstrated how electronic interactions can spontaneously generate topological phases and nematic order in homogeneous lattice models hosting Dirac and quadratic band touching points. These results established that strong correlations alone can induce nontrivial topology and competing symmetry-breaking phases, even in the absence of explicit topological terms in the noninteracting Hamiltonian. However, real materials and engineered quantum systems are often spatially inhomogeneous, where interfaces and boundaries play a central role in determining low-energy electronic properties.

Heterostructures formed by coupling topological insulators to strongly correlated materials provide a particularly rich platform to explore the interplay between topology, magnetism, and electronic correlations. At such interfaces, topological boundary states are no longer exposed to vacuum but are instead embedded in a correlated environment. This raises fundamental questions: Do topological edge modes survive in the presence of strong electronic correlations and magnetic order? If they do, how are their spin, charge, and transport properties modified by proximity to a correlated phase?

A paradigmatic example of this problem is the interface between a time-reversal invariant topological insulator and a Mott insulator. While the bulk topological insulator supports helical edge modes protected by time-reversal symmetry, the adjacent Mott insulating region can develop magnetic order and spin imbalance. The coexistence of these two competing tendencies makes the fate of topological edge states at correlated interfaces

highly nontrivial. Previous studies based on dynamical mean-field theory have shown that edge states can reconstruct or shift away from the physical interface. However, the role of magnetism, spin imbalance, and the resulting transport responses remain less explored, particularly within approaches that allow for spontaneous symmetry breaking.

In this chapter, we investigate a correlated Mott insulator–topological insulator heterostructure defined on a two-dimensional Lieb lattice. Using Hartree–Fock approach, complemented by slave-rotor mean-field theory and the inclusion of long-range Coulomb interactions, we study how topological edge states are reconstructed at buried interfaces and how magnetic proximity effects modify their properties. We show that topological edge modes persist at the MI–TI interface, but develop a spin imbalance induced by the ferrimagnetic order of the Mott insulator. As a result, the system supports equilibrium spin and charge currents localized near the buried interface, despite the bulk topological insulator remaining time-reversal symmetric.

The chapter is organized as follows. We first introduce the heterostructure geometry and model Hamiltonian. We then describe the theoretical methods used to capture spatially inhomogeneous charge and magnetic order. Subsequently, we present our results on the reconstruction of topological edge states, the emergence of spin imbalance, and the generation of charge and spin currents. Finally, we discuss the robustness of these findings in the strong-coupling regime and summarize the broader implications for correlated topological heterostructures.

4.1 Heterostructure geometry and physical setup

We consider a two-dimensional heterostructure composed of a Mott insulating (MI) region and a time-reversal-invariant topological insulator (TI), both defined on a Lieb lattice [94] [Fig. 4.1]. The Lieb lattice is particularly well suited for this study, as it naturally hosts

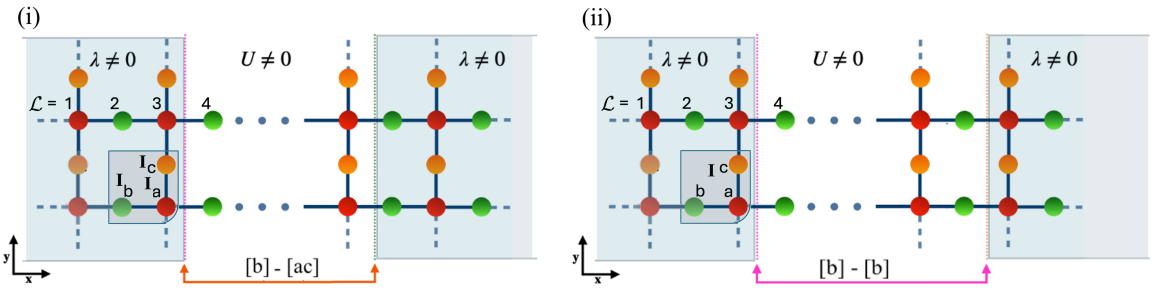

Figure 4.1: **Heterostructure schematic :** We divide a periodically identified Lieb lattice into $U \neq 0$ and $\lambda \neq 0$ parts along the x-direction. The resulting interfaces (vertical dashed lines) are parallel to the y-direction. Unit cells and sites of $\lambda_R - U_L$ interface (I_1) and $U_R - \lambda_L$ interface (I_2) are labeled as follows. The [ac] edge denotes that the (ac) sites on the U_L edge hybridize with the (b) sites on the region labeled by λ_R. At the [b] edge, the (b) sites on the U side interface with (ac) sites of the TI. The three-unit cell consists of sites labeled by 'a, 'b', and 'c.' The two heterostructure cases with interfaces [b]-[ac] and [b]-[b] are demarcated at the bottom with arrows. The three site unit cell is marked with 'I' and the vertical layers of (ac) sites and (b) sites demarcated by $\mathcal{L}$ =1, 2 ,3 ... are also shown.

flat bands, Dirac-like dispersive bands, and supports nontrivial topological phases in the presence of spin orbit coupling. These features make it an ideal platform to investigate the interplay between topology, strong correlations, and lattice geometry.

The heterostructure is constructed by partitioning the system along the x direction into two spatial regions. One region hosts strong onsite Hubbard interactions and realizes a Mott insulating phase, while the other region is noninteracting but includes intrinsic spin orbit coupling that stabilizes a quantum spin Hall insulating phase. Periodic boundary conditions are imposed along both the x and y directions. While translational invariance is preserved along the y direction parallel to the interface, it is explicitly broken along the x direction due to the spatial change in the electronic environment. This geometry gives rise to two MI–TI interfaces within a single finite system.

Unlike conventional topological insulators with boundaries exposed to vacuum, the interfaces studied here are buried inside a correlated environment. As a result, the topological edge modes are not terminated at an open boundary but are instead embedded within a mag-

netic and interacting background. This buried-interface geometry qualitatively modifies the fate of the edge states and allows for proximity-induced effects that are absent in isolated topological systems.

Depending on the lattice termination at the interface, we consider two distinct geometries. In the first case, referred to as the $[b]-[ac]$ geometry, the terminating b-sublattice sites on the $U \neq 0$ side are connected to the a sublattice sites on the $\lambda \neq 0$ side, while the terminating a-sublattice site on the $U \neq 0$ side are connected to the b-sublattice sites on the $\lambda \neq 0$ side. In the second case, denoted as the $[b]-[b]$ geometry, the terminating b-sublattice sites at both interfaces of the $U \neq 0$ region are connected exclusively to the a sublattice sites on the $\lambda \neq 0$ side. These two interface terminations allow us to investigate the sensitivity of the interfacial electronic properties to microscopic lattice details and to assess the robustness of the resulting physical phenomena.

The presence of two interfaces in the finite system leads to counterpropagating edge modes localized near opposite MI–TI boundaries. As will be shown in the following sections, these buried edge modes survive strong electronic correlations and develop a spin imbalance due to magnetic proximity effects. This imbalance plays a central role in generating equilibrium spin and charge currents localized near the interfaces.

4.2 Model Hamiltonian

We consider an interacting tight-binding model describing a MI–TI heterostructure on a two-dimensional Lieb lattice. Each unit cell contains three inequivalent sublattice sites, labeled a, b, and c. We study spinful fermions with spin index $\sigma =\uparrow, \downarrow$. The total Hamiltonian consists of nearest-neighbor hopping, intrinsic spin–orbit coupling, an onsite Hubbard interaction in the correlated region, and a long-range Coulomb interaction treated at the

mean-field level,

$$\mathcal{H} = \mathcal{H}_t + \mathcal{H}_{\mathrm{SOC}} + \mathcal{H}_{int} + \mathcal{H}_{\mathrm{C}}. \tag{4.1}$$

The kinetic energy arises from nearest-neighbor hopping on the Lieb lattice,

$$\mathcal{H}_t = -t \sum_{\langle i,j\rangle \in \Lambda} \sum_{\sigma} \left(d^{\dagger}_{i\sigma} d_{j\sigma} + \mathrm{H.c.} \right), \tag{4.2}$$

where $d^{\dagger}_{i\sigma}$ ($d_{i\sigma}$) creates (annihilates) an electron with spin σ at site i, and $\langle i,j\rangle$ denotes nearest-neighbor pairs. The corresponding density operators are $\hat{n}_{i\sigma} = d^{\dagger}_{i\sigma} d_{i\sigma}$ and $\hat{n}_i = \sum_{\sigma} \hat{n}_{i\sigma}$. Throughout this chapter, the hopping amplitude t sets the unit of energy. The full lattice is denoted by $\Lambda \equiv \Lambda_U \oplus \Lambda_\lambda$, where Λ_U and Λ_λ represent the sets of sites belonging to the interacting ($U \neq 0$) and spin–orbit coupled ($\lambda \neq 0$) regions, respectively.

The topological insulating region is generated by an intrinsic spin–orbit coupling of the Kane–Mele type, acting only on next-nearest-neighbor bonds within Λ_λ,

$$\mathcal{H}_{\mathrm{SOC}} = i\lambda \sum_{\langle\langle i,j\rangle\rangle \in \Lambda_\lambda} \sum_{\sigma,\sigma'} \nu_{ij}\, d^{\dagger}_{i\sigma} \left(\sigma^z\right)_{\sigma\sigma'} d_{j\sigma'}, \tag{4.3}$$

where λ is the spin–orbit coupling strength and $\langle\langle i,j\rangle\rangle$ denotes next-nearest-neighbor pairs. The factor $\nu_{ij} = \left(\mathbf{d}^1_{ij} \times \mathbf{d}^2_{ij}\right)_z = \pm 1$ depends on the clockwise/anti-clockwise traversal of electrons around the 'a' sites. This fact is encoded using d^1_{ij} and d^2_{ij} are the two unit vectors along the two nearest-neighbor bonds connecting 'a' sites to the 'b' and 'c' sites respectively [94]. The Pauli matrix σ^z acts in spin space. In the noninteracting limit, $\hat{H}_{\mathrm{SOC}}$ stabilizes a quantum spin Hall insulating phase in the TI region.

Strong electronic correlations are introduced through an onsite Hubbard interaction present only in the Mott-insulating region Λ_U,

$$\mathcal{H}_{int} = U \sum_{i \in \Lambda_U} \hat{n}_{i\uparrow} \hat{n}_{i\downarrow}, \tag{4.4}$$

where U is the interaction strength. This spatially inhomogeneous interaction profile models a sharp interface between a correlated Mott insulator and a noninteracting topological insulator.

To account for charge redistribution across the heterostructure, we include a long-range Coulomb interaction treated at the Hartree level [83, 84],

$$\mathcal{H}_{\mathrm{C}} = \sum_i \phi_i \, \hat{n}_i, \tag{4.5}$$

where ϕ_i is the Coulomb potential at site i. It is determined self-consistently as

$$\phi_i = \sum_{j \neq i} \frac{a_M t}{|\mathbf{r}_i - \mathbf{r}_j|} \left(\langle \hat{n}_j \rangle - z_j \right), \tag{4.6}$$

with $\mathbf{r}_i$ denoting the position of site i. The dimensionless parameter $a_M = e^2/(\epsilon a t)$ controls the strength of the Coulomb interaction, where ϵ is the dielectric constant and a the lattice spacing. We assume a uniform positive background charge $z_j = 1$ on all sites and consider a half-filled lattice, $\langle \hat{n}_i \rangle = 1$.

The inclusion of the long-range Coulomb interaction is essential for correlated heterostructures, as it suppresses unphysical phase separation and ensures a physically consistent charge redistribution at the MI–TI interface.

For the analysis of spatially inhomogeneous properties, we adopt two additional labeling conventions. First, lattice sites are denoted by $\{I_\alpha\}$, where I is the unit-cell index and $\alpha = a, b, c$ labels the sublattice within the Ith unit cell. Second, we introduce a layer index $\mathcal{L}$, which labels inequivalent layers along the x direction normal to the interface. These conventions, illustrated schematically in Fig. 4.1, are used throughout the following sections to present layer-resolved densities, magnetization, and current distributions.

4.3 Theoretical methods

To study the MI–TI heterostructure described by the Hamiltonian in Sec. 4.2, we employ a combination of Hartree–Fock theory and slave-rotor mean-field calculations. This combined approach allows us to capture spatially inhomogeneous charge and magnetic recon-

structions at the interface, while also assessing the robustness of the results in the strong-coupling regime.

4.3.1 Hartree–Fock approach

The primary method employed in this chapter is Hartree–Fock (HF) theory. The HF framework allows for spontaneous breaking of spin-rotational, time-reversal, and lattice symmetries, and is therefore well suited to describe magnetism, spin imbalance, and charge reconstruction in spatially inhomogeneous systems.

The onsite Hubbard interaction term $\mathcal{H}_{int}$ is decoupled solely in the density (Hartree) channel, as given in Eq. 2.8. For each interacting site $i \in \Lambda_U$, we retain the local spin-resolved densities $\langle \hat{n}_{i\sigma} \rangle$, allowing for spin polarization through unequal occupations $\langle \hat{n}_{i\uparrow} \rangle \neq \langle \hat{n}_{i\downarrow} \rangle$. No Fock (exchange) or spin-flip contributions, such as $\langle \hat{c}^\dagger_{i\sigma} \hat{c}_{i\bar{\sigma}} \rangle$, are included. Except for translational invariance along the y direction parallel to the interface, no symmetry constraints are imposed on the mean fields. Technical details of the mean-field solution of Hamiltonian Eq. 4.1 are provided in Appendix B.1.

Exploiting the remaining translational symmetry along y, we perform a partial Fourier transform in this direction and work in a mixed real–momentum representation. The Hamiltonian is diagonalized independently for each crystal momentum k_y, while retaining full real-space resolution along x. This enables the calculation of layer-resolved spectral functions, charge densities, magnetization profiles, and equilibrium currents.

The Coulomb potential ϕ_i introduced in Sec. 4.2 is determined self-consistently together with the Hartree mean fields. At each iteration, the local charge density $\langle \hat{n}_i \rangle$ is updated, the electrostatic potential ϕ_i is recalculated, and the resulting single-particle Hamiltonian is diagonalized until self-consistency is achieved. Convergence is monitored through the total energy and the spatial profiles of charge and magnetization. The computation of the Coulomb potential and details of the iterative self-consistency procedure are provided in

Appendices B.2 and B.3, respectively.

For each k_y, the Hartree mean-field Hamiltonian yields eigenvalues $\{\epsilon_{\kappa\sigma}(k_y)\}$ and eigenvectors $\{\langle I_\alpha, k_y, \sigma|\psi_\kappa\rangle\}$, where I denotes the unit-cell index along the x direction and $\alpha = a, b, c$ labels the sublattice within the unit cell. Although translational invariance is imposed along y, the eigenvectors retain full spatial dependence along x and therefore depend on the unit-cell index I. For convenience, we also construct layer-projected eigenvectors labeled by the layer index $\mathcal{L}$, as illustrated in Fig. 4.1.

Using the self-consistent HF solution, we compute the unit-cell-resolved density of states (DOS),

$$N_I(\omega) = \sum_{\kappa,k_y,\sigma} \sum_{\alpha\in I} |\langle I_\alpha, k_y, \sigma|\psi_\kappa\rangle|^2 \, \delta(\omega - \epsilon_{\kappa\sigma}(k_y)) \,, \tag{4.7}$$

where I labels the unit cell along the x direction.

To characterize magnetic order, we compute the unit-cell-averaged magnetization,

$$M_z = \frac{1}{6} \sum_{\alpha=a,b,c} \left(\langle n_{I_\alpha\uparrow}\rangle - \langle n_{I_\alpha\downarrow}\rangle\right), \tag{4.8}$$

which quantifies the spin imbalance averaged over the three sublattice sites of the Ith unit cell.

In Appendix C.1, we derive the expression for the charge current at a given unit cell I of the heterostructure. A brief summary is presented here. Starting from the continuity equation,

$$\dot{n}_I = i[H, n_I] = -\nabla \cdot \mathbf{J}_I, \tag{4.9}$$

with $n_I = \sum_{\sigma,\alpha} n_{I_\alpha\sigma}$ and $\overline{h} = 1$, we obtain

$$\dot{n}_I = -\sum_{\sigma=\uparrow,\downarrow} \left(j_\sigma^{(I\to I+\delta_x)} + j_\sigma^{(I\to I-\delta_x)} + j_\sigma^{(I\to I+\delta_y)} + j_\sigma^{(I\to I-\delta_y)} \right). \tag{4.10}$$

We define the spin-resolved current flowing along the positive x direction as

$$j_\sigma^x = \sum_I j_\sigma^{(I\to I+\delta_x)}, \tag{4.11}$$

and similarly along the positive y direction as

$$j_\sigma^y = \sum_I j_\sigma^{(I \to I+\delta_y)}. \tag{4.12}$$

The total charge current flowing along the y direction is

$$J_c = j_\uparrow^y + j_\downarrow^y, \tag{4.13}$$

while the spin current along y is defined as

$$J_s = j_\uparrow^y - j_\downarrow^y. \tag{4.14}$$

4.3.2 Slave-rotor mean-field approach

While Hartree–Fock theory captures magnetic ordering and spatial reconstruction at intermediate interaction strengths, it neglects quantum charge fluctuations and can overestimate magnetic order in the strong-coupling regime. To incorporate these strong-correlation effects, we complement the HF analysis with the standard slave-rotor (SR) mean-field approach.

In the slave-rotor formalism, the electron operator is written as

$$\hat{d}_{i\sigma} = e^{-i\theta_i} \hat{f}_{i\sigma}, \tag{4.15}$$

where the fermionic spinon $\hat{f}_{i\sigma}$ carries the spin degree of freedom and the bosonic rotor $e^{-i\theta_i}$ describes charge fluctuations. Within this framework, the Mott transition arises from the localization of the rotor degrees of freedom, while the spinon sector retains the underlying band structure.

Unlike HF theory, the SR approach does not capture magnetic order. Its strength lies instead in describing charge dynamics, the opening of the Mott gap, and the Mott–metal transition beyond static mean-field treatment. In this work, the SR equations are solved

self-consistently in the heterostructure geometry, including the spatially varying charge background induced by the Coulomb potential.

The main observable extracted from the SR calculation is the unit-cell-resolved density of states $N_I(\omega)$, obtained from the SR single-particle Green's function. Details of the heterostructure implementation of SR are provided in Appendix D.1, and the derivation and computation of $N_I(\omega)$ are given in Appendix D.2.

Together, the Hartree–Fock and slave-rotor approaches offer a complementary description of the system: Hartree–Fock captures magnetic reconstruction, while the slave-rotor method provides a strong-coupling perspective on charge fluctuations and the Mott transition.

4.4 Results

We present results for two kinds of heterostructure $[b]-[ac]$ and $[b]-[b]$ as shown in Fig. 4.1 (i) and (ii) respectively. We first discuss the Hartree-Fock (HF) mean field results for the $[b]-[ac]$ heterostructure.

4.4.1 Buried topological edge states and spectral reconstruction

Figure. 4.2(i) shows the unit-cell-resolved Hartree–Fock density of states (DOS) for the $[b]-[ac]$ heterostructure. The DOS is plotted layer by layer, starting from the bottom, which corresponds to the terminating unit cell of the $\lambda \neq 0$ region at the $[ac]$ interface, and extending up to the top, corresponding to the opposite terminating unit cell of the $U \neq 0$ region at the $[ac]$ interface. The central layer contains the two interface unit cells and straddles the $[b]$ interface. For clarity, the DOS associated with the $[b]$ and $[ac]$ interface unit cells is shown in red and black, respectively, while the DOS of all remaining unit cells is shown in blue. The chemical potential is indicated by $\omega - \mu = 0$.

As expected, the DOS of the bulk $U \neq 0$ region exhibits a large Mott gap of order

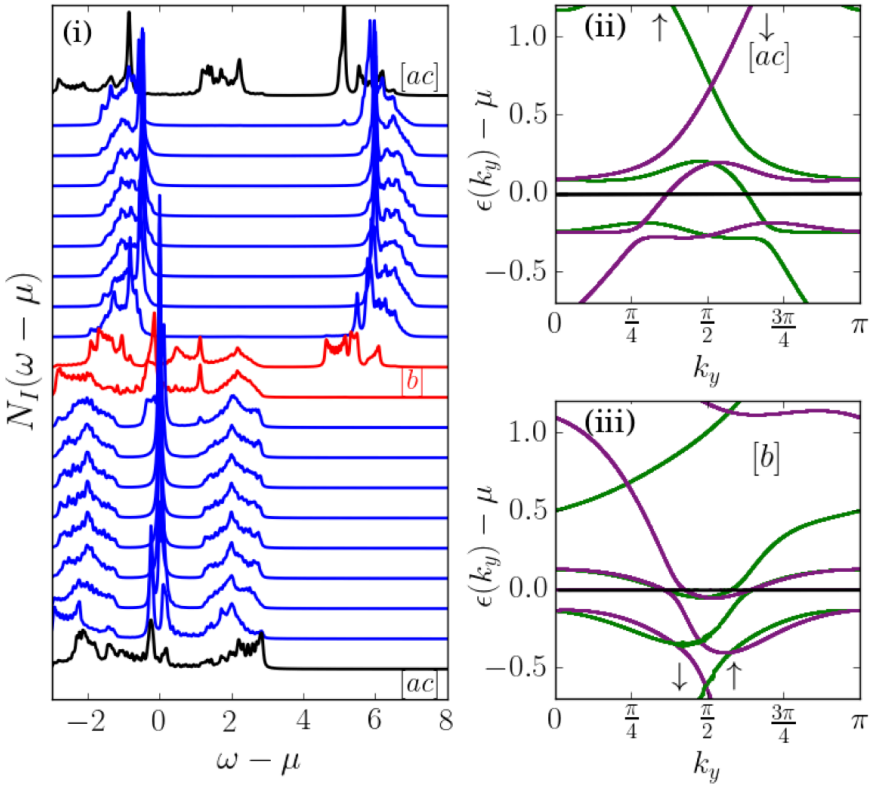

Figure 4.2: **Density of states & edge modes for [b]-[ac] heterostructure**. (i) show the unit-cell projected DOS. The interface unit cell DOS (black) and (red), respectively, are for the [b] and [ac] interfaces, one unit cell on either side of the interface. (ii) and (iii) show the spin-resolved momentum (k_y)-dependent buried-interface modes at the two interfaces. The dispersions are computed, including contributions from one unit cell on the $U \neq 0$ and three on the $\lambda \neq 0$ side, for the [ac] (black) and [b] (red) interfaces respectively. The results are presented for $\lambda = 0.3t$ and $U = 7t$ on a Lieb lattice with 20 three-site unit cells along the x-direction, while translation symmetry is assumed along the y-direction.

$\sim U/t$, with well-separated lower and upper Hubbard subbands, consistent with previous studies of the half-filled Lieb lattice [95, 96]. In contrast, the bulk $\lambda \neq 0$ region displays the characteristic noninteracting Lieb lattice band structure [97] , consisting of two dispersive bands and a flat band. The flat band lies symmetrically at an energy separation of approximately $4\lambda/t$ from the dispersive bands, as expected.

The interface unit cells, highlighted in red and black, exhibit qualitatively different spectral features compared to the bulk. In particular, both the $[b]$ and $[ac]$ interface unit cells

show finite spectral weight within the energy window corresponding to the bulk gaps. The presence of this in-gap spectral weight signals the emergence of states localized at the heterojunction interfaces. To clarify the nature of these states, we examine the spin-resolved energy–momentum (k_y-dependent) spectra shown in Fig. 4.2(ii) and Fig. 4.2(iii) for the $[ac]$ and $[b]$ interfaces, respectively. These spectra reveal dispersive edge modes with clear spin polarization and spin–momentum locking. A direct comparison with Fig. 4.2(i) confirms that these dispersive modes are constructed from the in-gap spectral weight observed in the interface DOS, establishing their topological origin and demonstrating that they are buried within the heterostructure.

For a conventional time-reversal symmetric topological insulator with an open boundary, counterpropagating spin-up and spin-down edge modes contribute equally and oppositely to the charge current, resulting in a net zero charge flow and a purely helical spin current. In the present heterostructure, however, the buried edge modes exhibit a qualitatively different behavior. The ferrimagnetic order in the Mott insulating region induces a spin imbalance in the adjacent $\lambda \neq 0$ interface unit cells. As a consequence, the spectral weights of the two spin channels become unequal, breaking the balance that enforces purely spin-polarized transport. This spin imbalance leads to the emergence of **a finite equilibrium charge current** carried by the buried topological edge modes, in contrast to the conventional helical edge-state picture. To further elucidate the microscopic origin of this behavior, we next analyze the spatial reconstruction of charge density and magnetic order across the MI–TI heterojunction.

4.4.2 Edge reconstruction

We now examine the spatial reconstruction of charge density and magnetic order across the heterostructure interfaces, as illustrated in Fig. 4.3. Panels (i) and (iii) show the layer-resolved charge density $N(\mathcal{L})$ and magnetization $M(\mathcal{L})$, respectively, for the $[b]-[ac]$ het-

erostructure at a fixed interaction strength $U = 7t$ and spin–orbit coupling $\lambda = 0.3t$. Along the x direction, the system consists of alternating layers of (**a**−**c**) and **b** sublattice sites, as depicted schematically in Fig. 4.1. For each layer, the charge density and magnetization are averaged over all (**a**−**c**) sites or over all **b** sites. The arrows in Fig. 4.3(i) mark the terminating layer index of (**a**−**c**) and **b** sites of $\lambda \neq 0$ side that are adjacent to the $U \neq 0$ region.

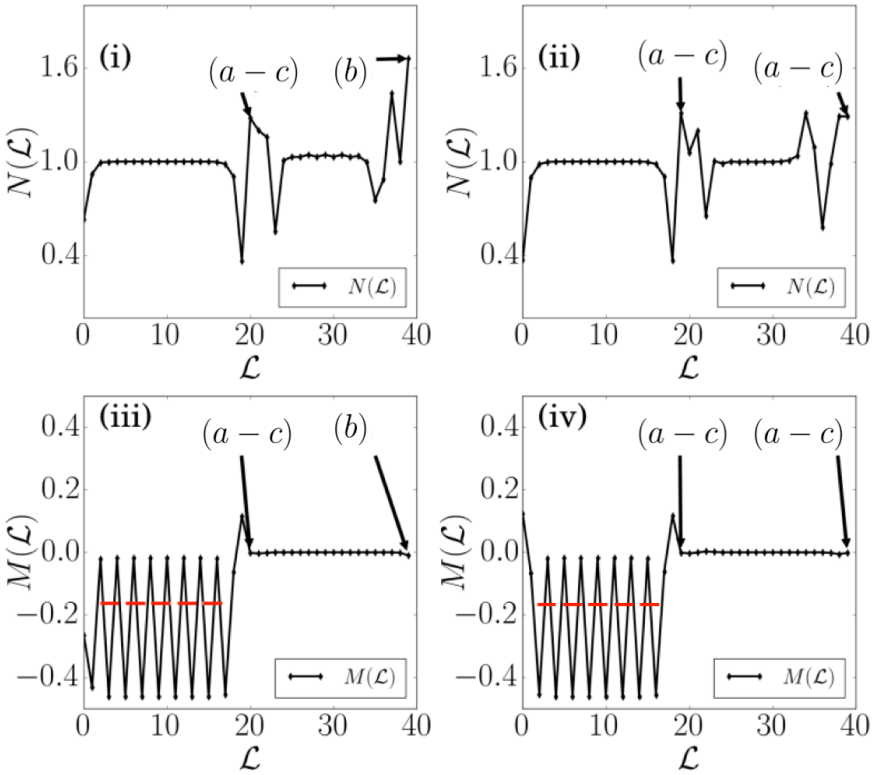

Figure 4.3: **Magnetic and charge reconstructions across the heterostructure interface.** (i) and (iii) show the layer-resolved charge density $N(\mathcal{L})$ (black line) and magnetization $M(\mathcal{L})$, respectively, along the x direction for the $[b]-[ac]$ heterostructure. (ii) and (iv) present the corresponding profiles for the $[b]-[b]$ heterostructure. In all panels, alternating layers along the x axis are composed of (**a**−**c**) and **b** sublattice sites, as defined in Fig. 4.1. The results are computed for $\lambda = 0.3t$ and $U = 7t$.

From Fig. 4.3(i), we observe that the average site occupation deep inside both the $U \neq 0$ and $\lambda \neq 0$ regions remains close to unity. This half-filled condition stabilizes a Mott insulating phase in the correlated region, consistent with the presence of a large Mott gap

in the bulk density of states shown earlier in Fig. 4.2(i). On the $\lambda \neq 0$ side, the system behaves as a half-filled Lieb lattice supporting both flat and dispersive bands [94].

In contrast, a substantial reconstruction of the charge density occurs in the vicinity of the heterojunction. Near the interface, the local filling deviates from $\langle n_i \rangle = 1$, indicating a redistribution of charge across the boundary. In particular, the $(\mathbf{a}-\mathbf{c})$ and **b** layers on the $\lambda \neq 0$ side adjacent to the interface exhibit charge densities exceeding unity, while the neighboring layers on the $U \neq 0$ side show a corresponding depletion. This self-consistent charge redistribution effectively dopes the interface region, leading to partially filled in-gap states and enabling the formation of buried metallic edge modes at the junction between the Mott insulator and the time-reversal-symmetric topological insulator.

We next consider the layer-resolved magnetization profiles shown in Fig. 4.3(iii). In the bulk $U \neq 0$ region, $M(\mathcal{L})$ exhibits an alternating pattern with a finite nonzero average value, in agreement with Lieb's theorem [97] and consistent with the formation of a ferrimagnetic Mott insulating state. For layers containing $(\mathbf{a}-\mathbf{c})$ sites, the magnetization represents the average contribution from the two sites, whereas for layers containing **b** sites it corresponds solely to the **b** sublattice. By contrast, the magnetization in the bulk $\lambda \neq 0$ region vanishes, as expected for a time-reversal-invariant topological insulator.

Notably, the layers on the $\lambda \neq 0$ side adjacent to the interface acquire a small but finite magnetization, as highlighted by the arrows in Fig. 4.3(iii). From the layer-resolved magnetization, we compute the unit-cell magnetization M_z, as defined in Sec. 4.3.1, for the unit cells at the $[b]$ and $[ac]$ interfaces on the $\lambda \neq 0$ side. We obtain finite negative values of approximately -0.0026 and -0.0043, respectively, demonstrating that magnetic order penetrates into the topological region over a few lattice spacings due to proximity effects.

Figures 4.3(ii) and 4.3(iv) show the corresponding charge density and magnetization profiles for the $[b]-[b]$ heterostructure. While the overall behavior remains qualitatively similar to that of the $[b]-[ac]$ case, quantitative differences arise in the interfacial recon-

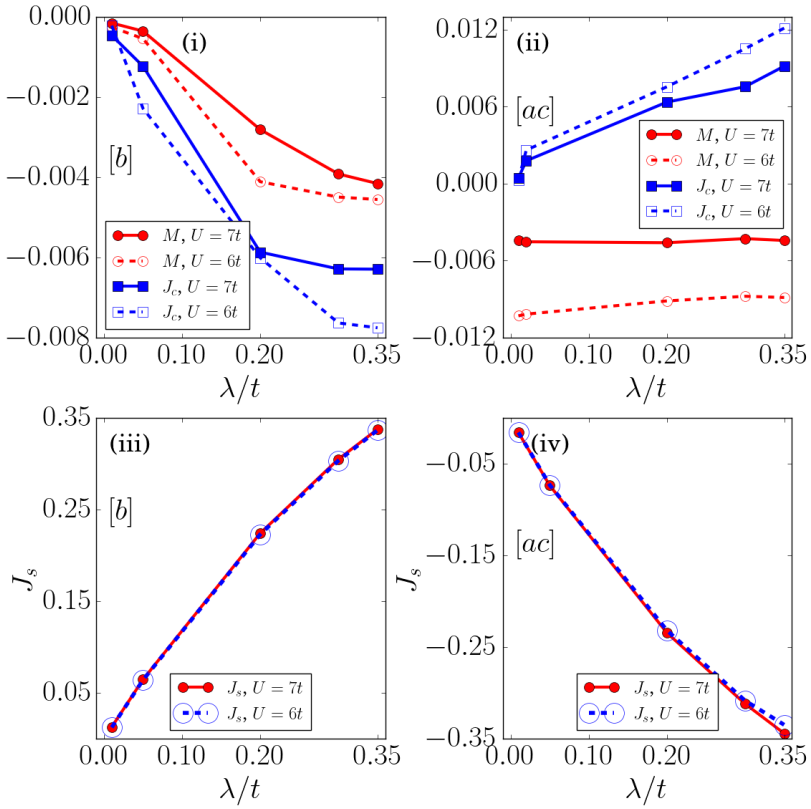

Figure 4.4: **Charge and spin currents for the $[b]$–$[ac]$ heterostructure.** (i) Charge current $J_c = J_\uparrow + J_\downarrow$ (squares) and magnetization M_z (circles) as functions of the spin–orbit coupling λ for the $[b]$ interface. (ii) shows the corresponding results for the $[ac]$ interface. (iii) and (iv) display the spin currents $J_s = J_\uparrow - J_\downarrow$ at the $[b]$ and $[ac]$ interfaces, respectively. All quantities are averaged over contributions from the three edge unit cells on the TI side of the heterostructure. Filled (open) symbols with solid (dashed) lines correspond to $U = 7t$ ($U = 6t$).

struction when the $[ac]$ termination is replaced by a $[b]$ termination. We have verified that these features are robust over a range of interaction strengths U.

The proximity-induced magnetization in the $\lambda \neq 0$ region plays a crucial role in determining the transport properties of the buried edge states. In the following section, we analyze how this induced magnetization leads to spin imbalance and the generation of equilibrium charge and spin currents at the heterostructure interfaces.

4.4.3 Charge and spin currents

Figure 4.4 presents the behavior of edge currents and induced magnetization in the [b]-[ac] heterostructure as functions of spin-orbit coupling λ, in the buried interfaces located on the topological ($\lambda \neq 0$) side.

Based on our numerical calculations, we find that for $U > 5t$, the charge current (J_c), spin current (J_s), and magnetization (M_z) penetrate approximately three unit cells into the TI region from the interface, along the x-direction with most contributions from the unit cell proximate to the interface. Therefore, all quantities shown in Fig. 4.4 are averaged over these three edge unit cells. The same averaging procedure is applied at both the [b] and [ac] edges.

Panels (i) and (ii) of Fig. 4.4 display the charge current $J_c = J_\uparrow + J_\downarrow$ (squares) and magnetization M_z (circles) for the [b] and [ac] edges, respectively. Across all values of λ, the magnetization induced at the TI edge is negative. This negative magnetization leads to an enhanced down-spin occupation among the edge states at both interfaces.

Importantly, due to spin-momentum locking, the direction of current carried by down-spin electrons differs between the two interfaces. As seen in Fig. 4.2(iii), at the [b] edge, down-spin carriers propagate along the negative y-direction, while at the [ac] edge [Fig. 4.2 (ii)], they move in the positive y-direction. These edge mode dispersions are also computed by including the contributions from three TI-side unit cells, ensuring consistency with the current profiles.

In the absence of magnetization—such as in a pristine TR symmetric topological insulator interfacing with vacuum—each edge would host counter-propagating spin-polarized currents of equal magnitude, resulting in a net zero charge current ($J_c = 0$) but a finite spin current ($J_s \neq 0$). However, the presence of proximity-induced negative magnetization at the interface breaks this symmetry, resulting in a finite J_c. Specifically, charge current

flows along the negative y-direction at the [b] edge and along the positive y-direction at the [ac] edge.

Moreover, both edges continue to support finite spin currents, as shown in Fig. 4.4(iii) and (iv), where $J_s = J_\uparrow - J_\downarrow$ is plotted as a function of λ. As expected, the magnitude of the spin current increases with increasing λ for both interfaces. However, unlike a TR symmetry-preserving system, a portion of this spin current is now converted into a charge current due to the induced edge magnetization. We note that the spin and charge currents at opposite edges cancel each other up to numerical accuracy, hence there is no net current in the system.

It is important to emphasize that the spin quantization axis is globally preserved across the entire heterostructure, and the induced edge magnetization remains weak. As a result, the helical nature of the spin-momentum-locked edge states and hence their topological protection persists despite the local breaking of time-reversal symmetry. This establishes a controlled mechanism for converting spin current into charge current, which can be interpreted as a *topology-driven conversion of a spin Hall effect into a charge Hall effect analog*. We also see that the overall conclusions remain unchanged for both the U values. These conclusions hold for even larger U values. We do not attempt to discuss the detailed microscopic origin of the evolution with U here within the HF theory, instead, we check the qualitative correctness of the results by using the strong-coupling SR mean-field approximation below.

4.4.4 Slave-rotor results

The slave-rotor (SR) mean-field theory provides an important complement to the Hartree–Fock (HF) approach by explicitly incorporating local charge fluctuations, which are neglected in HF treatments. At the same time, SR theory is intrinsically paramagnetic and therefore cannot capture magnetic ordering, in close analogy with paramagnetic dynamical

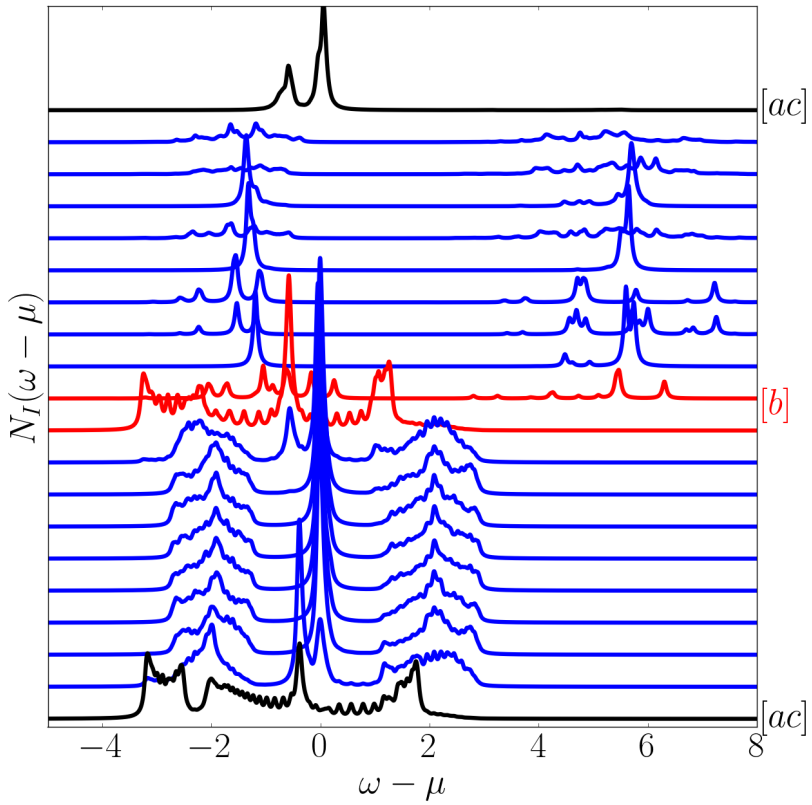

Figure 4.5: **Unit-cell-resolved density of states for the [b]-[ac] heterostructure within slave-rotor mean-field theory.** We present the unit-cell-resolved density of states (DOS) obtained from slave-rotor mean-field theory for the [b]-[ac] heterostructure. The red and black curves correspond to the DOS at the [b] and [ac] interfaces, respectively, computed from one unit cell on each side of the interface. The results are shown for $\lambda = 0.3t$ and $U = 7t$, on a Lieb lattice comprising 20 three-site unit cells along the x-direction, with translational symmetry assumed along the y-direction.

mean-field theory. In the present context, we employ the SR method to test the robustness of a central HF result, namely the survival of edge modes at large interaction strengths U when a strongly correlated region is interfaced with a topological insulator. The SR calculations, summarized in Appendix D.1, are performed on a background potential determined self-consistently from the long-range Coulomb interaction.

Figure 4.5 shows the unit-cell-resolved density of states (DOS) obtained within the slave-rotor mean-field framework for the $[b]$–$[ac]$ heterostructure. These results are directly

analogous to the HF DOS presented earlier in Fig. 4.2(i). In the bulk $U \neq 0$ region, the DOS exhibits a well-developed many-body Mott gap. The pronounced features of the lower and upper Hubbard subbands arise from the cluster-based treatment of the rotor Hamiltonian, as discussed in Appendix D.1. In contrast, the bulk $\lambda \neq 0$ region reproduces the expected band structure of a time-reversal-symmetric topological insulator on the Lieb lattice.

Most importantly, the interface unit cells at both the $[b]$ and $[ac]$ terminations show finite spectral weight within the bulk energy gaps. These in-gap features closely mirror the partially filled edge states observed in the HF analysis and provide independent confirmation of the existence of metallic edge modes at the heterojunction. In addition, we observe sharp peaks at the Fermi energy in the interface unit cells on the Mott insulating side. These features correspond to mid-gap resonances, a characteristic signature of doped Mott insulators, and can be understood as arising from Kondo-like screening of gapless spin degrees of freedom by carriers associated with the helical edge states penetrating into the correlated region [98]. Similar mid-gap states have been reported in dynamical mean-field theory studies of Mott insulator–topological insulator heterostructures [81].

Notably, these many-body resonances are absent in the HF description and can only be captured by approaches such as slave-rotor theory that retain local charge fluctuations. While the results shown correspond to $U = 7t$ to facilitate direct comparison with HF, we have verified that the qualitative features persist over a broad range of interaction strengths.

Taken together, the slave-rotor analysis confirms the robustness of buried helical edge modes deep into the strong-coupling regime and reveals additional correlation-driven features, such as mid-gap resonances, that lie beyond the scope of Hartree–Fock theory.

4.5 Summary and conclusion

Previous theoretical studies of Mott insulator–topological insulator (MI–TI) heterostructures have primarily examined scenarios in which electron–electron interactions and spin–orbit coupling coexist within the topological insulator region itself [99, 100]. Inhomogeneous dynamical mean-field theory has been widely employed to analyze such systems [81, 101]; however, these investigations have typically been limited to paramagnetic solutions and have often neglected long-range Coulomb interactions. This omission is significant, as the Coulomb potential plays a crucial role in suppressing electronic phase separation and stabilizing self-consistent charge redistribution at interfaces. Consequently, earlier approaches were unable to fully capture the physics of buried interfaces between a genuinely time-reversal-symmetric band topological insulator and a Mott insulator. Moreover, restricting the analysis to paramagnetic states prevented a systematic study of magnetic proximity effects on topological edge modes in such heterostructures.

In this thesis, we address these gaps by investigating a heterostructure composed of a time-reversal-symmetric topological insulator and a ferrimagnetic Mott insulator on a two-dimensional Lieb lattice. In this configuration, the correlated region develops ferrimagnetic order, while the topological region retains a bulk phase protected by spin–momentum locking. By solving the Hartree–Fock equations self-consistently and incorporating long-range Coulomb interactions, we demonstrate that metallic edge modes persist at the MI–TI interface even in the presence of magnetic proximity effects. The entire heterostructure shares a common spin quantization axis, and the induced magnetization in the topological edge states remains sufficiently weak such that the helical character of the boundary modes — and therefore their topological protection — is preserved.

A key outcome of this work is the emergence of a spin imbalance induced by this weak magnetization in the TI edge unit cells. This imbalance lifts the symmetry between counter-

propagating spin channels and generates a finite, topologically protected **charge current** localized at the interface. We demonstrate that both the magnitude and direction of this current can be controlled by tuning the spin–orbit coupling strength and by modifying the microscopic termination of the heterostructure. These results establish a clear mechanism by which magnetic proximity enables the conversion of a purely helical spin current into a controllable charge current without compromising the underlying topological character of the edge states.

To evaluate the robustness of the Hartree–Fock results in the strong-coupling regime, we carried out complementary calculations using slave-rotor mean-field theory. Although the slave-rotor framework is restricted to paramagnetic solutions and does not capture magnetic ordering, it incorporates local charge fluctuations absent in Hartree–Fock theory. The slave-rotor analysis confirms the persistence of buried edge modes deep within the Mott regime and reveals additional correlation-induced features, including mid-gap Kondo-like resonances, which extend beyond a static mean-field description. Taken together, the Hartree–Fock and slave-rotor approaches demonstrate that buried topological edge states remain robust against strong correlations and magnetic proximity effects.

Our results provide a concrete route to realizing interaction-tunable, magnetically proximitized topological edge modes with controllable charge transport. These predictions may be tested in recently realized material systems exhibiting the Lieb lattice geometry [102, 103]. In particular, layered transition-metal oxides with perovskite structures [104, 105] offer promising platforms for engineering such heterostructures. Systems combining strongly correlated 3d transition-metal layers with 5d layers possessing strong spin–orbit coupling are especially suitable for realizing topologically protected, partially spin-polarized charge currents. The ability to tune interaction strength and spin–orbit coupling through materials design further opens avenues for low-dissipation electronic and spintronic devices based on correlation-driven topological phenomena.

Chapter 5

Summary and conclusions

This thesis investigates how electron–electron interactions influence topological phases of matter in two-dimensional lattice systems, with a particular focus on band degeneracies, nematic ordering, and spatial inhomogeneity. Topological band theory has been highly successful in explaining phenomena such as the quantum Hall and quantum spin Hall effects in non-interacting systems. However, in many real materials, interactions between electrons are strong and can significantly modify the electronic properties. Understanding how these interactions affect topological behavior is therefore an important challenge in condensed matter physics. The main objective of this thesis is to explore how correlations can create, modify, or destroy topological phases and how these effects are influenced by symmetry breaking and spatially non-uniform environments. Through the study of two lattice models, this work sheds light on the rich interplay between electronic correlations and topology in quantum materials.

The thesis is divided into two closely related parts. The first part studies how strong electronic correlations can generate topological phases in uniform lattice systems that are topologically trivial in the absence of interactions. In these systems, topology emerges spontaneously from many-body effects. The second one investigates correlated topological heterostructures, where a topological phase already exists in one component of the system but is modified by strong correlations and proximity effects near an interface.

In the first part of this thesis, we studied a generalized two-dimensional Su–Schrieffer–Heeger (SSH) model that hosts a quadratic band-touching (QBT) point at half filling. Such a band structure provides an ideal setting for exploring correlation-driven phenomena be-

cause, unlike Dirac points, a QBT possesses a finite density of states at the Fermi level. Consequently, even relatively weak electron–electron interactions can destabilize the semimetallic state and drive the system into new ordered phases. Using a Hartree–Fock mean-field approach with a four-site unit cell, we systematically mapped the phase diagram by varying the hopping asymmetry, sublattice potential, and interaction strength, revealing a variety of competing interaction-driven phases.

One of the main results of this study is the rich phase diagram containing several competing ordered phases. These are quantum anomalous Hall (QAH) insulator, a site-nematic insulator (SNI), a stripe charge-density-wave phase, and a bond-nematic Dirac semimetal (BNDS). Each phase is associated with a different type of symmetry breaking and can be identified through its own characteristic order parameter.

In the symmetric checkerboard limit, where the quadratic band-touching point is protected by the lattice symmetry, we find that the BNDS phase appears as an intermediate phase between the QAH and SNI states. In this phase, the system spontaneously develops anisotropic bond order, breaking the rotational symmetry of the lattice while remaining gapless with Dirac-like excitations. Interestingly, this phase was not reported in several earlier mean-field studies. Our analysis shows that this is not because Hartree–Fock theory is unable to capture the BNDS phase. Rather, the BNDS phase was overlooked in previous works because bond nematicity was not investigated in the relevant parameter regime. Our analysis shows that once this possibility is taken into account, the BNDS phase emerges as a stable and distinct phase of the model.

Introducing hopping asymmetry in the generalized SSH model leads to significant changes in the phase diagram. Although the quadratic band-touching point remains intact, the anisotropy of the lattice strengthens the tendency toward nematic ordering and greatly enlarges the BNDS region. At the same time, the interaction-driven quantum anomalous Hall (QAH) phase becomes less stable and occupies a smaller part of the phase diagram. These

results highlight an important message of this thesis: topological order generated by interactions does not develop independently, but instead competes with other possible ordered states, such as nematic and charge-ordered phases. In many cases, these competing phases can be energetically more favorable. The rich phase diagram that emerges is therefore the result of a subtle competition between topology and symmetry breaking, governed by the underlying band structure and the strength of electronic interactions.

A detailed analysis of the order parameters reveals a clear sequence of phases as interactions are increased. At weak coupling, bond-nematic order dominates, leading to the BNDS phase. At intermediate coupling, the system supports a coexistence regime in which QAH order develops on top of a nematic background, resulting in a mixed topological–nematic phase. At strong coupling, site-nematic order becomes dominant and drives the system into a trivial insulating state. Importantly, site-nematic order remains finite across all regimes, indicating that topological phases in this model develop on a background with finite nematic order.

We also investigated the effect of a finite sublattice potential on the system. Introducing a sublattice potential lowers the rotational symmetry of the lattice from C_4 to C_2 and splits the quadratic band-touching point into a pair of Dirac cones. This reduces the density of states at the Fermi level, making the system less susceptible to interaction effects. As a result, the interaction-driven quantum anomalous Hall (QAH) phase becomes progressively less stable. We find that when the sublattice potential is small, electron interactions are still strong enough to induce topological order. However, as the sublattice potential increases, the bond-nematic Dirac semimetal (BNDS) phase becomes increasingly favored and occupies a larger region of the phase diagram. These results show that interaction-driven topological phases are highly sensitive to changes in the band structure and highlight the special role of quadratic band touching in enhancing correlation effects and stabilizing topological order.

Overall, the results presented in Chapter 3 show that the interaction-driven QAH phase is only one part of a much richer phase diagram. Nematic and charge-ordered phases are not merely competing states but are deeply connected to the emergence of topological order. In many cases, topological phases develop alongside symmetry-breaking orders and can even coexist with them. This strong connection between topology and nematicity is one of the central insights of this work and provides a deeper understanding of how electronic interactions shape the phases of correlated quantum systems.

The second part of the thesis focuses on spatially inhomogeneous systems, where translational symmetry is broken. In particular, we studied a heterostructure made of a ferrimagnetic Mott insulator and a time-reversal-invariant topological insulator on a Lieb lattice. This system provides an ideal setting to explore how strong electronic correlations affect topological states at an interface.

To investigate this problem, we used a combination of Hartree–Fock and slave-rotor mean-field methods within a mixed real- and momentum-space representation. Our results show that topological edge states can survive even when a topological insulator is placed next to a strongly correlated Mott insulator. Rather than being destroyed by the strong interactions, the edge states are reconstructed and shift away from the physical interface into the topological region. This finding demonstrates the robustness of topological boundary states and shows how they can adapt to the presence of strong correlations and spatial inhomogeneity.

One of the most important results of this study is the discovery of a spin imbalance in the reconstructed edge states near the buried interface. This imbalance arises from the magnetic influence of the neighboring Mott insulating region. Although the bulk topological insulator itself remains time-reversal symmetric, the magnetization close to the interface affects the edge states and leads to an unequal contribution from the two spin channels. Because these edge states exhibit spin–momentum locking, the resulting spin imbalance allows a

dissipationless spin current to be converted into a finite charge current near the interface. This finding reveals a novel interaction-driven mechanism for generating charge currents and shows that strong correlations and magnetic proximity effects can significantly modify the transport properties of topological edge states, even in the absence of an external magnetic field.

We showed that these phenomena are robust against changes in interface termination and persist across different heterostructure geometries. Complementary slave-rotor calculations confirm the robustness of the buried edge modes, beyond the range where Hartree–Fock theory is quantitatively reliable. This demonstrates that the key physical conclusions are robust across different mean-field approaches.

Overall, this thesis improves our understanding of how electronic interactions influence topological phases of matter. First, it clarifies how interactions can spontaneously generate topological phases in systems with enhanced low-energy density of states, while also competing with other ordered phases such as nematic and charge-ordered states. Second, it demonstrates that strong correlations can modify and control topological edge states at interfaces, leading to new mechanisms for dissipationless transport. Together, these results highlight the important role of electronic interactions in creating, transforming, and controlling topological phenomena in quantum materials.

The results presented in this thesis also open up several interesting directions for future research. On the interaction-driven topology side, it would be valuable to go beyond the mean-field approach and use more advanced methods such as exact diagonalization, density-matrix renormalization group (DMRG), or functional renormalization group (fRG). These techniques could provide a deeper understanding of the role of quantum fluctuations and help determine the stability of the BNDS and QAH phases more accurately. For the heterostructure problem, including effects such as dynamical screening, disorder, or periodic driving may reveal new ways to manipulate buried edge states and control interface

currents. More generally, the concepts explored in this thesis are relevant to a wide range of modern quantum platforms, including cold-atom optical lattices, moiré materials, and quantum simulators. These systems offer exceptional control over lattice geometry, interactions, and symmetry, making them ideal settings for testing and extending the ideas developed in this work.

In conclusion, this thesis shows that topology in quantum materials is not determined by band structure alone. Instead, it can emerge, evolve, and be significantly modified through electronic interactions and spatial inhomogeneity. By studying both interaction-driven topological phases in uniform lattice systems and the behavior of topological states in correlated heterostructures, this work provides a broader understanding of how topology and electronic correlations work together. The results presented here not only deepen our understanding of strongly correlated quantum matter but also offer new possibilities for designing and controlling topological phases in future quantum materials and devices.

References

[1] K. v. Klitzing, G. Dorda, and M. Pepper. New method for high-accuracy determination of the fine-structure constant based on quantized hall resistance. *Phys. Rev. Lett.*, 45:494–497, Aug 1980.

[2] Sergi Julià Farré. Controlling interactions in quantum materials: from a microscopic description to quantum simulation. 2022.

[3] S. Raghu, Xiao-Liang Qi, C. Honerkamp, and Shou-Cheng Zhang. Topological mott insulators. *Phys. Rev. Lett.*, 100:156401, Apr 2008.

[4] Charles Kittel. *Introduction to Solid State Physics*. Wiley, New York, 8 edition, 2005.

[5] Neil W. Ashcroft and N. David Mermin. *Solid State Physics*. Holt, Rinehart and Winston, New York, 1976.

[6] L. D. Landau. On the theory of phase transitions. *Zh. Eksp. Teor. Fiz.*, 7:19–32, 1937.

[7] B. I. Halperin. Quantized hall conductance, current-carrying edge states, and the existence of extended states in a two-dimensional disordered potential. *Phys. Rev. B*, 25:2185–2190, Feb 1982.

[8] D. J. Thouless, M. Kohmoto, M. P. Nightingale, and M. den Nijs. Quantized hall conductance in a two-dimensional periodic potential. *Phys. Rev. Lett.*, 49:405–408, Aug 1982.

[9] F. D. M. Haldane. Model for a quantum hall effect without landau levels: Condensed-matter realization of the ”parity anomaly”. *Phys. Rev. Lett.*, 61:2015–2018, Oct 1988.

[10] Noel A. García-Martínez, Adolfo G. Grushin, Titus Neupert, Belén Valenzuela, and Eduardo V. Castro. Interaction-driven phases in the half-filled spinless honeycomb lattice from exact diagonalization. *Phys. Rev. B*, 88:245123, Dec 2013.

[11] Yongfei Jia, Huaiming Guo, Ziyu Chen, Shun-Qing Shen, and Shiping Feng. Effect of interactions on two-dimensional dirac fermions. *Phys. Rev. B*, 88:075101, Aug 2013.

[12] Maria Daghofer and Martin Hohenadler. Phases of correlated spinless fermions on the honeycomb lattice. *Phys. Rev. B*, 89:035103, Jan 2014.

[13] Han-Qing Wu, Yuan-Yao He, Chen Fang, Zi Yang Meng, and Zhong-Yi Lu. Diagnosis of interaction-driven topological phase via exact diagonalization. *Phys. Rev. Lett.*, 117:066403, Aug 2016.

[14] Ke Yan, Hui Peng, Yujie Zhou, Haijian Li, and Zhongfan Liu. Formation of bilayer bernal graphene: Layer-by-layer epitaxy via chemical vapor deposition. *Nano Letters*, 11(3):1106–1110, 2011.

[15] Thomas C. Lang, Zi Yang Meng, Michael M. Scherer, Stefan Uebelacker, Fakher F. Assaad, Alejandro Muramatsu, Carsten Honerkamp, and Stefan Wessel. Antiferromagnetism in the hubbard model on the bernal-stacked honeycomb bilayer. *Phys. Rev. Lett.*, 109:126402, Sep 2012.

[16] Sumiran Pujari, Thomas C. Lang, Ganpathy Murthy, and Ribhu K. Kaul. Interaction-induced dirac fermions from quadratic band touching in bilayer graphene. *Phys. Rev. Lett.*, 117:086404, Aug 2016.

[17] Naoyuki Nakagawa, Harold Y. Hwang, and David A. Muller. Why some interfaces cannot be sharp. *Nature Materials*, 5:204–209, 2006.

[18] R. Pentcheva and W. E. Pickett. Charge localization or itineracy at $LaAlo_3$/$SrTio_3$ interfaces: Hole polarons, oxygen vacancies, and mobile electrons. *Phys. Rev. B*, 74:035112, Jul 2006.

[19] A. Ohtomo and H. Y. Hwang. A high-mobility electron gas at the laalo3/srtio3 heterointerface. *Nature*, 427(6973):423–426, 2004.

[20] J. Zak. Berry's phase for energy bands in solids. *Phys. Rev. Lett.*, 62:2747–2750, Jun 1989.

[21] Michael V. Berry. Quantal phase factors accompanying adiabatic changes. *Proceedings of the Royal Society of London. A. Mathematical and Physical Sciences*, 392:45 – 57, 1984.

[22] Barry Simon. Holonomy, the quantum adiabatic theorem, and berry's phase. *Phys. Rev. Lett.*, 51:2167–2170, Dec 1983.

[23] M. Z. Hasan and C. L. Kane. Colloquium: Topological insulators. *Rev. Mod. Phys.*, 82:3045–3067, Nov 2010.

[24] Marcel Franz and Laurens Molenkamp, editors. *Topological Insulators*, volume 6 of *Contemporary Concepts of Condensed Matter Science*. Elsevier, Amsterdam, Netherlands, 2013.

[25] B. Andrei Bernevig and Shou-Cheng Zhang. Quantum spin hall effect. *Phys. Rev. Lett.*, 96:106802, Mar 2006.

[26] C. L. Kane and E. J. Mele. Quantum spin hall effect in graphene. *Phys. Rev. Lett.*, 95:226801, Nov 2005.

[27] H.-M. Guo and M. Franz. Topological insulator on the kagome lattice. *Phys. Rev. B*, 80:113102, Sep 2009.

[28] W. P. Su, J. R. Schrieffer, and A. J. Heeger. Solitons in polyacetylene. *Phys. Rev. Lett.*, 42:1698–1701, Jun 1979.

[29] R. E. Peierls. *Quantum Theory of Solids*. International Series of Monographs on Physics. Oxford University Press, Oxford, United Kingdom, 1996.

[30] B. Andrei Bernevig and Taylor L. Hughes. *Topological Insulators and Topological Superconductors*. Princeton University Press, Princeton, NJ, USA, 2013.

[31] Gordon W. Semenoff. Condensed-matter simulation of a three-dimensional anomaly. *Phys. Rev. Lett.*, 53:2449–2452, Dec 1984.

[32] C. L. Kane and E. J. Mele. Z_2 topological order and the quantum spin hall effect. *Phys. Rev. Lett.*, 95:146802, Sep 2005.

[33] C. Weeks and M. Franz. Interaction-driven instabilities of a dirac semimetal. *Phys. Rev. B*, 81:085105, Feb 2010.

[34] Tanja Đurić, Nicholas Chancellor, and Igor F. Herbut. Interaction-induced anomalous quantum hall state on the honeycomb lattice. *Phys. Rev. B*, 89:165123, Apr 2014.

[35] Huaiming Guo and Yongfei Jia. Interaction-driven phases in a dirac semimetal: exact diagonalization results. *Journal of Physics: Condensed Matter*, 26(47):475601, 2014.

[36] Johannes Motruk, Adolfo G. Grushin, Fernando de Juan, and Frank Pollmann. Interaction-driven phases in the half-filled honeycomb lattice: An infinite density matrix renormalization group study. *Phys. Rev. B*, 92:085147, Aug 2015.

[37] Sylvain Capponi and Andreas M. Läuchli. Phase diagram of interacting spinless fermions on the honeycomb lattice: A comprehensive exact diagonalization study. *Phys. Rev. B*, 92:085146, Aug 2015.

[38] Daniel D. Scherer, Michael M. Scherer, and Carsten Honerkamp. Correlated spinless fermions on the honeycomb lattice revisited. *Phys. Rev. B*, 92:155137, Oct 2015.

[39] Kai Sun, Hong Yao, Eduardo Fradkin, and Steven A. Kivelson. Topological insulators and nematic phases from spontaneous symmetry breaking in 2d fermi systems with a quadratic band crossing. *Phys. Rev. Lett.*, 103:046811, Jul 2009.

[40] Stefan Uebelacker and Carsten Honerkamp. Instabilities of quadratic band crossing points. *Phys. Rev. B*, 84:205122, Nov 2011.

[41] Igor F. Herbut and Lukas Janssen. Topological mott insulator in three-dimensional systems with quadratic band touching. *Phys. Rev. Lett.*, 113:106401, Sep 2014.

[42] Rahul Nandkishore and Leonid Levitov. Quantum anomalous hall state in bilayer graphene. *Phys. Rev. B*, 82:115124, Sep 2010.

[43] Y. D. Chong, Xiao-Gang Wen, and Marin Soljačić. Effective theory of quadratic degeneracies. *Phys. Rev. B*, 77:235125, Jun 2008.

[44] Kai Sun and Eduardo Fradkin. Time-reversal symmetry breaking and spontaneous anomalous hall effect in fermi fluids. *Phys. Rev. B*, 78:245122, Dec 2008.

[45] Wei-Feng Tsai, Chen Fang, Hong Yao, and Jiangping Hu. Interaction-driven topological and nematic phases on the lieb lattice. *New Journal of Physics*, 17(5):055016, may 2015.

[46] Shouvik Sur, Shou-Shu Gong, Kun Yang, and Oskar Vafek. Quantum anomalous hall insulator stabilized by competing interactions. *Phys. Rev. B*, 98:125144, Sep 2018.

[47] Shouryya Ray, Matthias Vojta, and Lukas Janssen. Quantum critical behavior of two-dimensional fermi systems with quadratic band touching. *Phys. Rev. B*, 98:245128, Dec 2018.

[48] Shouryya Ray and Lukas Janssen. Gross-neveu-heisenberg criticality from competing nematic and antiferromagnetic orders in bilayer graphene. *Phys. Rev. B*, 104:045101, Jul 2021.

[49] Satoshi Nishimoto, Masaaki Nakamura, Aroon O'Brien, and Peter Fulde. Metal-insulator transition of fermions on a kagome lattice at 1/3 filling. *Phys. Rev. Lett.*, 104:196401, May 2010.

[50] Jun Wen, Andreas Rüegg, C.-C. Joseph Wang, and Gregory A. Fiete. Interaction-driven topological insulators on the kagome and the decorated honeycomb lattices. *Phys. Rev. B*, 82:075125, Aug 2010.

[51] W. Zhu, Shou-Shu Gong, Tian-Sheng Zeng, Liang Fu, and D. N. Sheng. Interaction-driven spontaneous quantum hall effect on a kagome lattice. *Phys. Rev. Lett.*, 117:096402, Aug 2016.

[52] Hoi-Yin Hui, Mengsu Chen, Sumanta Tewari, and V. W. Scarola. Chiral topological phases in optical lattices without synthetic fields. *Phys. Rev. A*, 98:023609, Aug 2018.

[53] Yafei Ren, T.-S. Zeng, W. Zhu, and D. N. Sheng. Quantum anomalous hall phase stabilized via realistic interactions on a kagome lattice. *Phys. Rev. B*, 98:205146, Nov 2018.

[54] Soumya Sankar, Ruizi Liu, Cheng-Ping Zhang, Qi-Fang Li, Caiyun Chen, Xue-Jian Gao, Jiangchang Zheng, Yi-Hsin Lin, Kun Qian, Ruo-Peng Yu, Xu Zhang, Zi Yang Meng, Kam Tuen Law, Qiming Shao, and Berthold Jäck. Experimental evidence for a berry curvature quadrupole in an antiferromagnet. *Phys. Rev. X*, 14:021046, Jun 2024.

[55] Johannes Reuther, Ronny Thomale, and Stephan Rachel. Magnetic ordering phenomena of interacting quantum spin hall models. *Phys. Rev. B*, 86:155127, Oct 2012.

[56] M. Hohenadler, T. C. Lang, and F. F. Assaad. Correlation effects in quantum spin-hall insulators: A quantum monte carlo study. *Phys. Rev. Lett.*, 106:100403, Mar 2011.

[57] Christopher N. Varney, Kai Sun, Marcos Rigol, and Victor Galitski. Interaction effects and quantum phase transitions in topological insulators. *Phys. Rev. B*, 82:115125, Sep 2010.

[58] Dong Zheng, Guang-Ming Zhang, and Congjun Wu. Particle-hole symmetry and interaction effects in the kane-mele-hubbard model. *Phys. Rev. B*, 84:205121, Nov 2011.

[59] M. Hohenadler, Z. Y. Meng, T. C. Lang, S. Wessel, A. Muramatsu, and F. F. Assaad. Quantum phase transitions in the kane-mele-hubbard model. *Phys. Rev. B*, 85:115132, Mar 2012.

[60] Jan Carl Budich, Björn Trauzettel, and Giorgio Sangiovanni. Fluctuation-driven topological hund insulators. *Phys. Rev. B*, 87:235104, Jun 2013.

[61] A. Amaricci, A. Valli, G. Sangiovanni, B. Trauzettel, and M. Capone. Coexistence of metallic edge states and antiferromagnetic ordering in correlated topological insulators. *Phys. Rev. B*, 98:045133, Jul 2018.

[62] Amal Medhi, Vijay B. Shenoy, and H. R. Krishnamurthy. Synchronous and asynchronous mott transitions in topological insulator ribbons. *Phys. Rev. B*, 85:235449, Jun 2012.

[63] A. Amaricci, L. Privitera, F. Petocchi, M. Capone, G. Sangiovanni, and B. Trauzettel. Edge state reconstruction from strong correlations in quantum spin hall insulators. *Phys. Rev. B*, 95:205120, May 2017.

[64] S Gariglio, N Reyren, A D Caviglia, and J-M Triscone. Superconductivity at the laalo3/srtio3 interface. *Journal of Physics: Condensed Matter*, 21(16):164213, mar 2009.

[65] Julie A. Bert, Beena Kalisky, Christopher Bell, Minu Kim, Yasuyuki Hikita, Harold Y. Hwang, and Kathryn A. Moler. Direct imaging of the coexistence of ferromagnetism and superconductivity at the laalo3/srtio3 interface. *Nature Physics*, 7(10):767–771, 2011.

[66] M. Ben Shalom, M. Sachs, D. Rakhmilevitch, A. Palevski, and Y. Dagan. Tuning spin-orbit coupling and superconductivity at the $srtio_3/laalo_3$ interface: A magnetotransport study. *Phys. Rev. Lett.*, 104:126802, Mar 2010.

[67] S. Okamoto and A. J. Millis. Electronic reconstruction at an interface between a mott insulator and a band insulator. *Nature*, 428:630–633, 2004.

[68] Satoshi Okamoto and Andrew J. Millis. Spatial inhomogeneity and strong correlation physics: A dynamical mean-field study of a model mott-insulator–band-insulator heterostructure. *Phys. Rev. B*, 70:241104, Dec 2004.

[69] Suguru Ueda, Norio Kawakami, and Manfred Sigrist. Electronic and magnetic properties in strongly correlated heterostructures. *Phys. Rev. B*, 85:235112, Jun 2012.

[70] Giovanni Borghi, Michele Fabrizio, and Erio Tosatti. Strongly correlated metal interfaces in the gutzwiller approximation. *Phys. Rev. B*, 81:115134, Mar 2010.

[71] R. W. Helmes, T. A. Costi, and A. Rosch. Kondo proximity effect: How does a metal penetrate into a mott insulator? *Phys. Rev. Lett.*, 101:066802, Aug 2008.

[72] A. Euverte, F. Hébert, S. Chiesa, R. T. Scalettar, and G. G. Batrouni. Kondo screening and magnetism at interfaces. *Phys. Rev. Lett.*, 108:246401, Jun 2012.

[73] Jimmy A. Hutasoit and Tudor D. Stanescu. Induced spin texture in semiconductor/topological insulator heterostructures. *Phys. Rev. B*, 84:085103, Aug 2011.

[74] Jak Chakhalian, John W. Freeland, Andrew J. Millis, Christos Panagopoulos, and James M. Rondinelli. Colloquium: Emergent properties in plane view: Strong correlations at oxide interfaces. *Rev. Mod. Phys.*, 86:1189–1202, Oct 2014.

[75] Xiao-Liang Qi and Shou-Cheng Zhang. Topological insulators and superconductors. *Rev. Mod. Phys.*, 83:1057–1110, Oct 2011.

[76] Tudor D. Stanescu, Jay D. Sau, Roman M. Lutchyn, and S. Das Sarma. Proximity effect at the superconductor–topological insulator interface. *Phys. Rev. B*, 81:241310, Jun 2010.

[77] Sabyasachi Tiwari, Maarten L. Van de Put, Kristiaan Temst, William G. Vandenberghe, and Bart Sorée. Atomistic modeling of spin and electron dynamics in two-dimensional magnets switched by two-dimensional topological insulators. *Phys. Rev. Appl.*, 19:014040, Jan 2023.

[78] Stephan Rachel and Motohiko Ezawa. Giant magnetoresistance and perfect spin filter in silicene, germanene, and stanene. *Phys. Rev. B*, 89:195303, May 2014.

[79] John S. Van Dyke and Dirk K. Morr. Effects of defects and dephasing on charge and spin currents in two-dimensional topological insulators. *Phys. Rev. B*, 95:045151, Jan 2017.

[80] Tomá š Rauch, Markus Flieger, Jürgen Henk, and Ingrid Mertig. Nontrivial interface states confined between two topological insulators. *Phys. Rev. B*, 88:245120, Dec 2013.

[81] Suguru Ueda, Norio Kawakami, and Manfred Sigrist. Proximity effects in a topological-insulator/mott-insulator heterostructure. *Phys. Rev. B*, 87:161108, Apr 2013.

[82] H. Ishida and A. Liebsch. Buried topological edge state associated with interface between topological band insulator and mott insulator. *Phys. Rev. B*, 90:205134, Nov 2014.

[83] J. Salafranca, M. J. Calderón, and L. Brey. Magnetoresistance of an all-manganite spin valve: A thin antiferromagnetic insulator sandwiched between two ferromagnetic metallic electrodes. *Phys. Rev. B*, 77:014441, Jan 2008.

[84] Kalpataru Pradhan and Arno P. Kampf. Interfacial magnetism in manganite superlattices. *Phys. Rev. B*, 88:115136, Sep 2013.

[85] Takahiro Fukui, Yasuhiro Hatsugai, and Hiroshi Suzuki. Chern numbers in discretized brillouin zone: Efficient method of computing (spin) hall conductances. *Journal of the Physical Society of Japan*, 74(6):1674–1677, 2005.

[86] Feng Liu and Katsunori Wakabayashi. Novel topological phase with a zero berry curvature. *Phys. Rev. Lett.*, 118:076803, Feb 2017.

[87] Chang-An Li, Sang-Jun Choi, Song-Bo Zhang, and Björn Trauzettel. Dirac states in an inclined two-dimensional su-schrieffer-heeger model. *Phys. Rev. Res.*, 4:023193, Jun 2022.

[88] Chang-An Li, Song-Bo Zhang, Jan Carl Budich, and Björn Trauzettel. Transition from metal to higher-order topological insulator driven by random flux. *Phys. Rev. B*, 106:L081410, Aug 2022.

[89] Hongyu Lu, Shouvik Sur, Shou-Shu Gong, and D. N. Sheng. Interaction-driven quantum anomalous hall insulator in a dirac semimetal. *Phys. Rev. B*, 106:205105, Nov 2022.

[90] Sergi Julià-Farré, Markus Müller, Maciej Lewenstein, and Alexandre Dauphin. Self-trapped polarons and topological defects in a topological mott insulator. *Phys. Rev. Lett.*, 125:240601, Dec 2020.

[91] Xuecong Ji, Jiacheng Gao, Changming Yue, Zhijun Wang, Hua Wu, Xi Dai, and Hongming Weng. Interaction-driven topological phase transition in monolayer $crcl_2(pyrazine)_2$. *Phys. Rev. B*, 106:235103, Dec 2022.

[92] Hongyu Lu, Kai Sun, Zi Yang Meng, and Bin-Bin Chen. Ubiquitous nematic dirac semimetal emerging from interacting quadratic band touching systems. *Phys. Rev. B*, 109:L081106, Feb 2024.

[93] Zi Hong Liu, Hongyu Lu, Zi Yang Meng, and Lukas Janssen. Interaction-induced nematic dirac semimetal from quadratic band touching: A constrained-path quantum monte carlo study. *arXiv preprint arXiv:2507.15668*, 2025.

[94] C. Weeks and M. Franz. Topological insulators on the lieb and perovskite lattices. *Phys. Rev. B*, 82:085310, Aug 2010.

[95] Natanael C. Costa, Tiago Mendes-Santos, Thereza Paiva, Raimundo R. dos Santos, and Richard T. Scalettar. Ferromagnetism beyond lieb's theorem. *Phys. Rev. B*, 94:155107, Oct 2016.

[96] L. Oliveira-Lima, N. C. Costa, J. Pimentel de Lima, R. T. Scalettar, and R. R. dos Santos. Dynamical resilience to disorder: The dilute hubbard model on the lieb lattice. *Phys. Rev. B*, 101:165109, Apr 2020.

[97] Elliott H. Lieb. Two theorems on the hubbard model. *Phys. Rev. Lett.*, 62:1927–1927, Apr 1989.

[98] Henrik Kajueter, Gabriel Kotliar, and Goetz Moeller. Doped mott insulator: Results from mean-field theory. *Phys. Rev. B*, 53:16214–16226, Jun 1996.

[99] A. Amaricci, L. Privitera, F. Petocchi, M. Capone, G. Sangiovanni, and B. Trauzettel. Edge state reconstruction from strong correlations in quantum spin hall insulators. *Phys. Rev. B*, 95:205120, May 2017.

[100] A. Amaricci, A. Valli, G. Sangiovanni, B. Trauzettel, and M. Capone. Coexistence of metallic edge states and antiferromagnetic ordering in correlated topological insulators. *Phys. Rev. B*, 98:045133, Jul 2018.

[101] H. Ishida and A. Liebsch. Buried topological edge state associated with interface between topological band insulator and mott insulator. *Phys. Rev. B*, 90:205134, Nov 2014.

[102] Bin Cui, Xingwen Zheng, Jianfeng Wang, Desheng Liu, Shijie Xie, and Bing Huang. Realization of lieb lattice in covalent-organic frameworks with tunable topology and magnetism. *Nature Communications*, 11(1):66, 2020.

[103] Wenjun Wu, Shuo Sun, Chi Sin Tang, Jing Wu, Yu Ma, Lingfeng Zhang, Chuanbing Cai, Jianxin Zhong, Milorad V. Milošević, Andrew T. S. Wee, and Xinmao Yin. Realization of a 2d lieb lattice in a metal–inorganic framework with partial flat bands and topological edge states. *Advanced Materials*, 36(40):2405615, 2024.

[104] I. Fina, X. Marti, D. Yi, J. Liu, J. H. Chu, C. Rayan-Serrao, S. Suresha, A. B. Shick, J. Železný, T. Jungwirth, J. Fontcuberta, and R. Ramesh. Anisotropic magnetoresistance in an antiferromagnetic semiconductor. *Nature Communications*, 5(1):4671, 2014.

[105] Suman Sardar, Megha Vagadia, Tejas M. Tank, Jayaprakash Sahoo, and D. S. Rana. Exploring anisotropic phases and spin transport in perovskite heterostructures: Insights into 3d/5d interfaces for antiferromagnetic spintronics. *Journal of Applied Physics*, 135(8):080701, 02 2024.

[106] Serge Florens and Antoine Georges. Slave-rotor mean-field theories of strongly correlated systems and the mott transition in finite dimensions. *Phys. Rev. B*, 70:035114, Jul 2004.

[107] E. Zhao and A. Paramekanti. Self-consistent slave rotor mean-field theory for strongly correlated systems. *Phys. Rev. B*, 76:195101, Nov 2007.

[108] Sayan Jana, Arijit Saha, and Anamitra Mukherjee. Impact of strong correlations on a band topological insulator on the lieb lattice. *Phys. Rev. B*, 100:045420, Jul 2019.

[109] Atanu Paul, Anamitra Mukherjee, Indra Dasgupta, Arun Paramekanti, and Tanusri Saha-Dasgupta. Hybridization-switching induced mott transition in $ab\mathrm{o}_3$ perovskites. *Phys. Rev. Lett.*, 122:016404, Jan 2019.

Appendix A

A.1 Chern number and QAH order parameter

In Sec. 3.4, we have reported that the QAH phase is characterized by a quantized Chern number. Here, we provide an explicit numerical evidence.

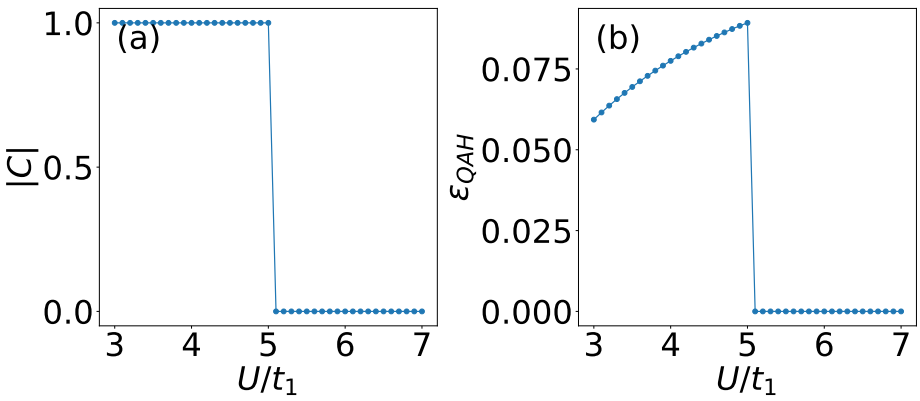

Figure A.1: (a) Chern number as a function of the nearest-neighbor interaction strength U. The system exhibits a quantized value $|C| = 1$ within the QAH phase. (b) Quantum anomalous Hall (QAH) order parameter as a function of U, which is finite in the QAH phase and vanishes upon entering the site-nematic phase. Results are shown for $V = 3.0t_1$, $t_1 = 1.0$, and $t_2 = 2.0$.

Figure A.1(a) shows the dependence of the Chern number on the nearest-neighbor interaction U. The Chern number of the occupied bands is evaluated using the Fukui–Hatsugai–Suzuki method [85]. For $U < U_c$, we obtain $C = \pm 1$, indicating a topologically nontrivial phase stabilized by spontaneous time-reversal-symmetry breaking. This quantized value persists over a finite interaction window, reflecting the robustness of the QAH state. Beyond the critical strength U_c, the Chern number abruptly drops to $C = 0$, signaling a transition into a topologically trivial SNI.

The corresponding QAH order parameter, displayed in Fig. A.1(b), remains finite in the QAH region ($U < U_c$) and vanishes in the SNI phase. The simultaneous disappearance of both the Chern number and the QAH order parameter at U_c highlights the direct competition between interaction-driven topological order and symmetry-breaking nematic order. These results clearly demonstrate a correlation-induced topological phase transition stabilized in an intermediate interaction regime.

A.2 Proof of particle-hole symmetry

1. Symmetry Criterion in k-Space

For a multi-band Hamiltonian $H(\vec{k})$, the condition for particle-hole symmetry (PHS) is

$$\mathcal{C}H(\vec{k})\mathcal{C}^{-1} = -H(-\vec{k}), \tag{A.1}$$

where $\mathcal{C} = UK$ is an antiunitary operator, U is unitary, and K denotes complex conjugation.

We consider the generalized two-dimensional SSH model in the noninteracting limit at half filling with

$$U = V = \delta = 0,$$

and impose the special parameter choice

$$t_1 = t_2 = t, \qquad t_1' = -t_2' = t'. \tag{A.2}$$

2. Momentum-Space Hamiltonian Before Parameter Substitution

The momentum-space Hamiltonian in the basis

$$\Psi_{\mathbf{k}}^{\dagger} = (c_{1,\mathbf{k}}^{\dagger}, c_{2,\mathbf{k}}^{\dagger}, c_{3,\mathbf{k}}^{\dagger}, c_{4,\mathbf{k}}^{\dagger})$$

is

$$H = \sum_{\mathbf{k}} \Psi_{\mathbf{k}}^{\dagger} H(\mathbf{k}) \Psi_{\mathbf{k}}, \tag{A.3}$$

with

$$H(\mathbf{k}) = \begin{pmatrix} 0 & H_{01} & H_{02} & H_{03} \\ H_{10} & 0 & H_{12} & H_{13} \\ H_{20} & H_{21} & 0 & H_{23} \\ H_{30} & H_{31} & H_{32} & 0 \end{pmatrix}. \tag{A.4}$$

The nearest-neighbor hopping matrix elements are

$$H_{01}(\mathbf{k}) = -\left(t_1 e^{-ik_x} + t_2 e^{ik_x}\right), \tag{A.5}$$

$$H_{02}(\mathbf{k}) = -\left(t_1 e^{-ik_y} + t_2 e^{ik_y}\right), \tag{A.6}$$

$$H_{13}(\mathbf{k}) = -\left(t_1 e^{-ik_y} + t_2 e^{ik_y}\right), \tag{A.7}$$

$$H_{23}(\mathbf{k}) = -\left(t_1 e^{-ik_x} + t_2 e^{ik_x}\right). \tag{A.8}$$

The next-nearest-neighbor hopping matrix elements are

$$H_{03}(\mathbf{k}) = t_1' e^{-i(k_x+k_y)} + t_1' e^{i(k_x+k_y)} + t_2' e^{-i(k_x-k_y)} + t_2' e^{i(k_x-k_y)}, \tag{A.9}$$

$$H_{12}(\mathbf{k}) = t_2' e^{-i(k_x-k_y)} + t_2' e^{i(k_x-k_y)} + t_1' e^{-i(k_x+k_y)} + t_1' e^{i(k_x+k_y)}. \tag{A.10}$$

Using

$$e^{i\theta} + e^{-i\theta} = 2\cos\theta,$$

we obtain

$$H_{03}(\mathbf{k}) = 2t_1' \cos(k_x + k_y) + 2t_2' \cos(k_x - k_y), \tag{A.11}$$

$$H_{12}(\mathbf{k}) = 2t_2' \cos(k_x - k_y) + 2t_1' \cos(k_x + k_y). \tag{A.12}$$

3. Hamiltonian at the Special Symmetric Point

Substituting

$$t_1 = t_2 = t, \qquad t_1' = -t_2' = t',$$

the nearest-neighbor terms become

$$H_{01} = H_{10} = -2t \cos k_x, \tag{A.13}$$

$$H_{02} = H_{20} = -2t \cos k_y, \tag{A.14}$$

$$H_{13} = H_{31} = -2t \cos k_y, \tag{A.15}$$

$$H_{23} = H_{32} = -2t \cos k_x. \tag{A.16}$$

For the next-nearest-neighbor terms,

$$H_{03} = 2t' \cos(k_x + k_y) - 2t' \cos(k_x - k_y), \tag{A.17}$$

$$H_{12} = -2t' \cos(k_x + k_y) + 2t' \cos(k_x - k_y). \tag{A.18}$$

Using the trigonometric identity

$$\cos(A + B) - \cos(A - B) = -2 \sin A \sin B,$$

we obtain

$$H_{03} = -4t' \sin k_x \sin k_y, \tag{A.19}$$

$$H_{12} = 4t' \sin k_x \sin k_y. \tag{A.20}$$

Therefore the Hamiltonian becomes

$$H(\mathbf{k}) = \begin{pmatrix} 0 & -2t\cos k_x & -2t\cos k_y & -4t'\sin k_x \sin k_y \\ -2t\cos k_x & 0 & 4t'\sin k_x \sin k_y & -2t\cos k_y \\ -2t\cos k_y & 4t'\sin k_x \sin k_y & 0 & -2t\cos k_x \\ -4t'\sin k_x \sin k_y & -2t\cos k_y & -2t\cos k_x & 0 \end{pmatrix}. \tag{A.21}$$

4. Complex Conjugation and Momentum Inversion

Since all matrix elements are real,

$$H^*(\mathbf{k}) = H(\mathbf{k}). \tag{A.22}$$

Now under momentum inversion

$$k_x \to -k_x, \qquad k_y \to -k_y,$$

we use

$$\cos(-x) = \cos x, \qquad \sin(-x) = -\sin x.$$

Hence

$$\sin(-k_x)\sin(-k_y) = \sin k_x \sin k_y. \tag{A.23}$$

Therefore,

$$H(-\mathbf{k}) = H(\mathbf{k}). \tag{A.24}$$

5. Construction of the Particle-Hole Operator

Define the permutation matrix

$$P = \begin{pmatrix} 0 & 1 & 0 & 0 \\ 1 & 0 & 0 & 0 \\ 0 & 0 & 0 & 1 \\ 0 & 0 & 1 & 0 \end{pmatrix}, \tag{A.25}$$

which exchanges the sublattice pairs

$$(a \leftrightarrow b), \qquad (c \leftrightarrow d).$$

Next define the gauge transformation matrix

$$\tilde{P} = \begin{pmatrix} 1 & 0 & 0 & 0 \\ 0 & -1 & 0 & 0 \\ 0 & 0 & -1 & 0 \\ 0 & 0 & 0 & 1 \end{pmatrix}. \tag{A.26}$$

Now define

$$U = P\tilde{P}. \tag{A.27}$$

Explicitly,

$$U = \begin{pmatrix} 0 & -1 & 0 & 0 \\ 1 & 0 & 0 & 0 \\ 0 & 0 & 0 & 1 \\ 0 & 0 & -1 & 0 \end{pmatrix}. \tag{A.28}$$

6. Action of the Symmetry Operator

We now compute

$$UH(\mathbf{k})U^{\dagger}.$$

Direct matrix multiplication gives

$$UH(\mathbf{k})U^\dagger = \begin{pmatrix} 0 & 2t\cos k_x & 2t\cos k_y & 4t'\sin k_x \sin k_y \\ 2t\cos k_x & 0 & -4t'\sin k_x \sin k_y & 2t\cos k_y \\ 2t\cos k_y & -4t'\sin k_x \sin k_y & 0 & 2t\cos k_x \\ 4t'\sin k_x \sin k_y & 2t\cos k_y & 2t\cos k_x & 0 \end{pmatrix}. \tag{A.29}$$

Comparing with the original Hamiltonian,

$$UH(\mathbf{k})U^\dagger = -H(\mathbf{k}). \tag{A.30}$$

Finally define the antiunitary operator

$$\mathcal{C} = UK, \tag{A.31}$$

where K is the complex conjugation operator.

Then

$$\mathcal{C}H(\mathbf{k})\mathcal{C}^{-1} = UH^*(\mathbf{k})U^\dagger \tag{A.32}$$

$$= UH(\mathbf{k})U^\dagger \tag{A.33}$$

$$= -H(\mathbf{k}) \tag{A.34}$$

$$= -H(-\mathbf{k}). \tag{A.35}$$

Therefore,

$$\boxed{\mathcal{C}H(\mathbf{k})\mathcal{C}^{-1} = -H(-\mathbf{k})} \tag{A.36}$$

which proves that the generalized two-dimensional SSH Hamiltonian possesses particle-hole symmetry at

$$t_1 = t_2 = t, \qquad t_1' = -t_2' = t', \qquad \delta = 0.$$

Consequently, the energy spectrum satisfies

$$E(\mathbf{k}) \leftrightarrow -E(\mathbf{k}),$$

and the bands occur in symmetric pairs about zero energy.

Appendix B

B.1 Mean field in k-space

This section outlines the HF mean-field formalism introduced in section 4.3.1. The interacting Hubbard Hamiltonian is given by

$$\mathcal{H}_{int} = U \sum_i \hat{n}_{i\uparrow}\hat{n}_{i\downarrow}. \tag{B.1}$$

We employ the mean-field approximation to simplify the two-body interaction term. This involves decoupling the product of number operators as

$$\hat{n}_{i\uparrow}\hat{n}_{i\downarrow} \approx \langle \hat{n}_{i\uparrow} \rangle \hat{n}_{i\downarrow} + \langle \hat{n}_{i\downarrow} \rangle \hat{n}_{i\uparrow} - \langle \hat{n}_{i\uparrow} \rangle \langle \hat{n}_{i\downarrow} \rangle . \tag{B.2}$$

Under this approximation, the interaction Hamiltonian takes the following form:

$$\mathcal{H}_{int} = \sum_i \frac{U}{2}[\langle n_i \rangle n_i - 4 \langle m_i \rangle m_i] - \frac{U}{4}[\langle n_i \rangle^2 - 4 \langle m_i \rangle^2], \tag{B.3}$$

where $n_i = (n_{i\uparrow} + n_{i\downarrow})$ is the total on-site occupation and $m_i = \frac{1}{2}(n_{i\uparrow} - n_{i\downarrow})$ is the on-site magnetization. The second term in Eq. B.3 introduces a global constant energy shift and can, therefore, be neglected as it does not affect the relative energy spectrum of the system. The resulting interacting Hamiltonian in momentum space is

$$\mathcal{H}_{int} = \sum_{I_\alpha, k_y} \frac{U}{2}[\langle n^{I_\alpha} \rangle n^{I_\alpha}_{k_y} - 4 \langle m^{I_\alpha} \rangle m^{I_\alpha}_{k_y}], \tag{B.4}$$

where k_y is conjugate momenta along the translation invariant direction y and α denotes sites within the unit cell I as shown in Fig.4.1. $\langle n^{I_\alpha} \rangle = \frac{1}{N} \sum_{k_y} \left\langle n^{I_\alpha}_{k_y} \right\rangle$ and $\langle m^{I_\alpha} \rangle = \frac{1}{N} \sum_{k_y} \left\langle m^{I_\alpha}_{k_y} \right\rangle$ respectively. Here $\langle n^{I_\alpha} \rangle$ and $\langle m^{I_\alpha} \rangle$ are calculated self consistently.

B.2 Long-range Coulomb interaction

The average electron density of the MI and TI in the heterostructure is determined by the chemical potential μ. The long-range Coulomb interaction between all charges is crucial in controlling the amount of charge transfer across the interfaces. To account for this effect, we solve the Coulomb potentials ϕ^{I_α} self-consistently at the mean-field level, following the methodology established in the literature [83, 84]. The Hamiltonian describes the long-range Coulomb interaction:

$$\mathcal{H}_{\mathrm{C}} = \sum_{I_\alpha, k_y} \phi^{I_\alpha} n^{I_\alpha}_{k_y}, \tag{B.5}$$

where,

$$\phi^{I_\alpha} = \sum_{\beta \neq \alpha} a_M t \frac{\langle \hat{n}_{I_\beta} \rangle - z_{I_\beta}}{|\vec{r}_{I_\alpha} - \vec{r}_{I_\beta}|} + \sum_{J \neq I, \beta} a_M t \frac{\langle \hat{n}_{J_\beta} \rangle - z_{J_\beta}}{|\vec{r}_{I_\alpha} - \vec{r}_{J_\beta}|}$$

In this equation, $\langle \hat{n}_{J_\beta} \rangle$ represents the electron charge density at the site (J_β) and a_M is the Madelung constant, as defined in the paper. Throughout the calculations, we assume a uniform background charge $z_{J_\beta} = 1$. Solving ϕ^{I_α} self-consistently allows us to incorporate the long-range Coulomb interaction effect on the charge transfer across the MI-TI interface, ensuring that the electrostatic effects are treated consistently within the mean-field framework.

B.3 Computational details of self-consistency in Hartree-Fock approach in heterostructure problem

We performed self-consistent calculations of the mean-field parameters $\langle \hat{n}_i \rangle$ and $\langle \hat{m}_i \rangle$. We set the convergence tolerance in energy to be $\sim 10^{-5}$. Additionally, we fixed the Madelung constant to $a_M = 1$ throughout all calculations to ensure a uniform electron density within the bulk on each side of the heterostructure. We averaged the Coulomb potential within the

$\lambda \neq 0$ side, excluding two unit cells from each end of the $\lambda \neq 0$ side.

Appendix C

C.1 Derivation of current

In section 4.3.1 of the main text, we briefly outlined the prescription to calculate the current operators. In this section, we provide derivation of current operators. The full Hamiltonian is written as:

$$\mathcal{H} = \mathcal{H}_t + \mathcal{H}_{SO} + \mathcal{H}_{int} + \mathcal{H}_C, \tag{C.1}$$

In the mean-field approximation $[n_I, \mathcal{H}_{int}] = [n_I, \mathcal{H}_C] = 0$, simplifying the analysis. The hopping and spin-orbit coupling terms are rewritten in terms of the unit cell index I. The hopping Hamiltonian becomes

$$\begin{aligned}\mathcal{H}_t = &- t \sum_{I\sigma} [d^\dagger_{I_a\sigma} d_{I_c\sigma} + d^\dagger_{I_a\sigma} d_{I_b\sigma} + d^\dagger_{(I+\delta_y)_a\sigma} d_{I_c\sigma} \\ &+ d^\dagger_{(I+\delta_x)_a\sigma} d_{I_b\sigma}] + h.c.\end{aligned} \tag{C.2}$$

The spin-orbit coupling Hamiltonian is expressed as

$$\begin{aligned}\mathcal{H}_{SO} =& i\lambda \sum_{I\sigma} s d^\dagger_{I_c\sigma} d_{I_b\sigma} - i\lambda \sum_{I\sigma} s d^\dagger_{I_b\sigma} d_{I_c\sigma} \\ &- i\lambda \sum_{I\sigma} s d^\dagger_{I_c\sigma} d_{(I+\delta_y)_b\sigma} + i\lambda \sum_{I\sigma} s d^\dagger_{(I+\delta_y)_b\sigma} d_{I_c\sigma} \\ &- i\lambda \sum_{I\sigma} s d^\dagger_{(I+\delta_y-\delta_x)_b\sigma} d_{I_c\sigma} + i\lambda \sum_{I\sigma} s d^\dagger_{I_c\sigma} d_{(I+\delta_y-\delta_x)_b\sigma} \\ &- i\lambda \sum_{I\sigma} s d^\dagger_{(I+\delta_x)_c\sigma} d_{I_b\sigma} + i\lambda \sum_{I\sigma} s d^\dagger_{I_b\sigma} d_{(I+\delta_x)_c\sigma},\end{aligned} \tag{C.3}$$

The local Hubbard interaction term is expressed as:

$$\mathcal{H}_{int} = U \sum_{I_\alpha} n_{I_\alpha\uparrow} n_{I_\alpha\downarrow}, \tag{C.4}$$

where U is the strength of the on-site Hubbard interaction , $s = 1(-1)$ for $\uparrow$ $(\downarrow)$. δ_x and δ_y are the next-nearest lattice translation vector relative to the unit cell I in the positive x and y direction respectively. Using these Hamiltonians, the current operators are derived by summing over contributions from all unit cells in a specific direction. The current operator in the y-direction is found to be

$$\begin{aligned} j^y_\sigma = &\sum_I it(d^\dagger_{(I+\delta_y)_a\sigma}d_{I_c\sigma} - d^\dagger_{I_c\sigma}d_{(I+\delta_y)_a\sigma}) \\ &+\lambda\sum_I s(d^\dagger_{I_c\sigma}d_{(I+\delta_y)_b\sigma} + d^\dagger_{(I+\delta_y)_b\sigma}d_{I_c\sigma}) \\ &-\lambda\sum_I s(d^\dagger_{I_c\sigma}d_{(I+\delta_y-\delta_x)_b\sigma} + d^\dagger_{(I+\delta_y-\delta_x)_b\sigma}d_{I_c\sigma}), \end{aligned} \tag{C.5}$$

Similarly, the current operator in the x-direction is

$$\begin{aligned} j^x_\sigma = &\sum_I it(d^\dagger_{(I+\delta_x)_a\sigma}d_{I_b\sigma} - d^\dagger_{I_b\sigma}d_{(I+\delta_x)_a\sigma}) \\ &-\lambda\sum_I s(d^\dagger_{I_b\sigma}d_{(I+\delta_x)_c\sigma} + d^\dagger_{(I+\delta_x)_c\sigma}d_{I_b\sigma}) \\ &+\lambda\sum_I s(d^\dagger_{I_b\sigma}d_{(I+\delta_x-\delta_y)_c\sigma} + d^\dagger_{(I+\delta_x-\delta_y)_c\sigma}d_{I_b\sigma}). \end{aligned} \tag{C.6}$$

These expressions are derived under the assumption that adjacent layers exist on both sides of the layer that is being considered for the current calculation, i.e for bulk layers.

Appendix D

D.1 Slave-rotor mean field theory

We study the correlation effects in the heterostructure using the slave-rotor mean-field theory, as outlined in previous works [106, 107, 108]. To make this study self-contained, we briefly summarize the method here. The electronic creation and annihilation operators are decomposed into a direct product of a bosonic rotor degree of freedom and an auxiliary fermion. The rotor accounts for charge occupations, while the spinons preserve the anti-symmetric nature of the electronic operators. To distinguish between the two sides of the heterostructure, we denote the electronic operator on the U-side as $c_{I_\alpha,\sigma}$ and on the λ-side as $d_{I_\alpha,\sigma}$. Specifically, the transformations are:

$$\begin{aligned} d_{i,\sigma} &\to c_{I_\alpha,\sigma} \text{ for U side }, \\ d_{i,\sigma} &\to d_{I_\alpha,\sigma} \text{ for } \lambda \text{ side }. \end{aligned} \tag{D.1}$$

We then apply the slave-rotor decomposition to the U-side as follows:

$$\begin{aligned} c^\dagger_{I_\alpha\sigma} &= f^\dagger_{I_\alpha\sigma} e^{-i\theta_{I_\alpha}}, \\ c_{I_\alpha\sigma} &= f_{I_\alpha\sigma} e^{i\theta_{I_\alpha}}, \end{aligned} \tag{D.2}$$

where $f^\dagger_{I_\alpha\sigma}$, $f_{I_\alpha\sigma}$ are spinon creation and annihilation operators and $e^{\pm i\theta_{I_\alpha}}$ represent the rotor creation and annihilation operators. The rotor operators act on charge states as

$$e^{\pm i\theta_{I_\alpha}} \left|n^\theta_{I_\alpha}\right\rangle = \left|n^\theta_{I_\alpha} \pm 1\right\rangle . \tag{D.3}$$

To ensure that the spin and the charge degrees of freedom add up to physical electron occupation in the unit cell, we need to restrict the rotor spectrum. At half-filling, the average

occupation of every unit cell is three. To remove the unphysical states from the direct product basis, we impose the following constraint equation

$$\sum_{\alpha} \left(n^{\theta}_{I_\alpha} + n^{f}_{I_{\alpha\uparrow}} + n^{f}_{I_{\alpha\downarrow}} - \mathcal{I} \right) = 0, \tag{D.4}$$

where the electron number is equal to the spinon number i.e. $n^{f}_{I_{\alpha\sigma}} = n^{e}_{I_{\alpha\sigma}}$ and $\mathcal{I}$ is the identity operator.

Then, the Hamiltonian Eq. 4.1 is reformulated in terms of spinon and rotor operators to derive an exact expression under the slave-rotor decomposition. Subsequently, we introduce a mean-field ansatz to approximate the ground state:

$$|\Psi\rangle = \left|\Psi^{fd}\right\rangle \left|\Psi^{\theta}\right\rangle, \tag{D.5}$$

where the superscript d denotes the collective index for the electronic operators on the λ-side, f refers to the spinon operator on the U-side, and θ denotes the rotor operator. The Hubbard interaction term is confined exclusively to the U-side, resulting in the spinon contribution emerging solely from the U-side. The next step is to compute two decoupled Hamiltonians, $H_{f,d} \equiv \left\langle \Psi^{\theta} | H | \Psi^{\theta} \right\rangle$ and $H_{\theta} \equiv \left\langle \Psi^{fd} | H | \Psi^{fd} \right\rangle$. The expressions are:

$$\begin{aligned} H_{f,d} = &- \sum_{I\alpha\beta\sigma} t_{I_\alpha I_\beta \sigma} \left\langle \Psi^{\theta} \left| e^{-i\theta_{I_\alpha}} e^{i\theta_{I_\beta}} \right| \Psi^{\theta} \right\rangle f^{\dagger}_{I_{\alpha}\sigma} f_{I_{\beta}\sigma} - \sum_{I\alpha J\beta\sigma} t_{I_\alpha J_\beta \sigma} d^{\dagger}_{I_{\alpha}\sigma} d_{J_{\beta}\sigma} + \sum_{I\alpha\sigma} \phi^{I_\alpha} \Big(f^{\dagger}_{I_{\alpha}\sigma} f_{I_{\alpha}\sigma} \\ &+ d^{\dagger}_{I_{\alpha}\sigma} d_{I_{\alpha}\sigma} \Big) - \sum_{I\alpha J\beta\sigma} t_{I_\alpha J_\beta \sigma} \left\langle \Psi^{\theta} \left| e^{-i\theta_{I_\alpha}} \right| \Psi^{\theta} \right\rangle f^{\dagger}_{I_{\alpha}\sigma} d_{J_{\beta}\sigma} - \sum_{I\alpha\sigma} \left(\lambda_{I_\alpha \sigma} + \mu \right) f^{\dagger}_{I_{\alpha}\sigma} f_{I_{\alpha}\sigma}, \end{aligned} \tag{D.6}$$

$$\begin{aligned} H_{\theta} = &- \sum_{I\alpha J\beta\sigma} t_{I_\alpha J_\beta \sigma} \left\langle \Psi^{fd} \left| f^{\dagger}_{I_{\alpha}\sigma} f_{J_{\beta}\sigma} \right| \Psi^{fd} \right\rangle e^{-i\theta_{I_\alpha}} e^{i\theta_{J_\beta}} - \sum_{I\alpha J\beta\sigma} t_{I_\alpha J_\beta \sigma} \left\langle \Psi^{fd} \left| f^{\dagger}_{I_{\alpha}\sigma} d_{J_{\beta}\sigma} \right| \Psi^{fd} \right\rangle e^{-i\theta_{I_\alpha}} \\ &+ U/2 \sum_{I\alpha} \left(n^{\theta}_{I_\alpha} \right)^2 - \sum_{I\alpha\sigma} \left(\lambda_{I_\alpha \sigma} + \frac{U}{2} \right) n^{\theta}_{I_\alpha}, \end{aligned} \tag{D.7}$$

where

$$\phi^{I_\alpha} = \sum_{J\neq I,\beta} a_M t \frac{\left\langle f^\dagger_{J_\beta\sigma} f_{J_\beta\sigma}\right\rangle - z_{J_\beta}}{\left|\vec{r}_{I_\alpha} - \vec{r}_{J_\beta}\right|} + \sum_{\beta\neq\alpha} a_M t \frac{\left\langle f^\dagger_{I_\beta\sigma} f_{I_\beta\sigma}\right\rangle - z_{I_\beta}}{\left|\vec{r}_{I_\alpha} - \vec{r}_{I_\beta}\right|} + \sum_{J\neq I,\beta} a_M t \frac{\left\langle d^\dagger_{J_\beta\sigma} d_{J_\beta\sigma}\right\rangle - z_{J_\beta}}{\left|\vec{r}_{I_\alpha} - \vec{r}_{J_\beta}\right|}$$
$$+ \sum_{\beta\neq\alpha} a_M t \frac{\left\langle d^\dagger_{I_\beta\sigma} d_{I_\beta\sigma}\right\rangle - z_{I_\beta}}{\left|\vec{r}_{I_\alpha} - \vec{r}_{I_\beta}\right|}$$

are onsite Coulomb potentials as discussed in Eq. (4.5). The two coupled Hamiltonians are solved self-consistently under the constraint equation. The spinon Hamiltonian refers to Eq. (D.6) a one-body physics, while the rotor Hamiltonian in Eq. (D.7) describes many-body physics which can be solved using cluster mean-field theory. Since the system is inhomogeneous, we solve using multiple unit cell clusters along the x-direction and repeat this in the y-direction.

D.2 Observable in Slave-rotor calculation

We express the single-particle electron Green's function as a convolution of the spinon and rotor Green's functions [109]. By taking the imaginary part of this reconstructed Green's function, we compute the spectral function. We define the local (on-site) retarded Matsubara Green's function as

$$\begin{aligned} G_{I_\alpha\sigma}(i\omega_n) &= -\int_0^\beta d\tau e^{i\omega_n\tau} \left\langle \Psi \left| c_{I_\alpha,\sigma}(\tau) c^\dagger_{I_\alpha,\sigma}(0) \right| \Psi \right\rangle \\ &= -\int_0^\beta d\tau e^{i\omega_n\tau} \left\langle \Psi^f \left| f_{I_\alpha\sigma}(\tau) f^\dagger_{I_\alpha\sigma}(0) \right| \Psi^f \right\rangle \\ &\quad \times \left\langle \Psi^\theta \left| e^{-i\theta_{I_\alpha}(\tau)} e^{i\theta_{I_\alpha}(0)} \right| \Psi^\theta \right\rangle . \end{aligned} \tag{D.8}$$

The spinon correlation function in Eq. (D.8) is

$$\begin{aligned} &\tfrac{1}{2}\textstyle\sum_\sigma \left\langle f_{I_\alpha\sigma}(\tau) f^\dagger_{I_\alpha\sigma}(0) \right\rangle \\ &\quad = \tfrac{1}{2}\textstyle\sum_{\alpha\sigma} \left|\left\langle \chi^f_\alpha \mid I_\alpha, \sigma \right\rangle\right|^2 \left[1 - n_f\left(\epsilon^f_\alpha - \mu_f\right)\right] e^{-\tau\left(\epsilon^f_\alpha - \mu_f\right)}, \end{aligned} \tag{D.9}$$

where $\left|\chi_\alpha^f\right\rangle$ and ϵ_α^f are the spinon eigenvectors and eigenvalues, respectively. The rotor correlation function in Eq. (D.8) is expressed as

$$\begin{aligned}&\left\langle e^{-i\theta_{I_\alpha}(\tau)} e^{i\theta_{I_\alpha}(0)}\right\rangle \\ &= \tfrac{1}{Z_\theta}\textstyle\sum_{m,n} e^{-\beta\epsilon_m}\left\langle m\left|e^{-i\theta_{I_\alpha}}\right|n\right\rangle\left\langle n\left|e^{i\theta_{I_\alpha}}\right|m\right\rangle e^{\tau(\epsilon_m-\epsilon_n)},\end{aligned} \tag{D.10}$$

where ϵ_m and $|m\rangle$ are the eigenvalues and corresponding eigenvectors of the rotor Hamiltonian, respectively. Here, Z_θ is the rotor partition function

$$Z_\theta = \sum_m e^{-\beta\epsilon_m}. \tag{D.11}$$

The integration in Eq. (D.8) performed over imaginary time τ. We then analytically continue back to the real frequency to obtain $G_{I\alpha\sigma}(\omega)$. The projected density of state (PDOS) is obtained from its imaginary part of the full Green's function.